

The evolutionary steps from nonlinear to turbulent waves on gravity-driven films over topography

Von der Fakultät für Ingenieurwissenschaften
der Universität Bayreuth
zur Erlangung der Würde eines
Doktor-Ingenieur (Dr.-Ing.)
genehmigte Dissertation

von
Dipl.-Phys. Markus Johannes Dauth
aus
Bayreuth

Erstgutachter: Prof. Dr. N. Aksel
Zweitgutachter: Prof. Dr. V. Bontozoglou
Tag der mündlichen Prüfung: 06. August 2019

Lehrstuhl für Technische Mechanik und Strömungsmechanik
Universität Bayreuth
2019

Journal publications

- Markus Dauth, Mario Schörner and Nuri Aksel:
What makes the free surface waves over topographies convex or concave? A study with Fourier analysis and particle tracking.
Physics of Fluids, **29**, 092108 (2017).
- Markus Dauth and Nuri Aksel:
Breaking of waves on thin films over topographies.
Physics of Fluids, **30**, 082113 (2018).
- Markus Dauth and Nuri Aksel:
Transition of regular wave fronts to irregular wave fronts in gravity-driven thin films over topography.
Acta Mechanica, **230**(7), 2475–2490 (2019).

Abstract

A gravity-driven viscous film flow over an inclination is a fundamental problem in the field of fluid mechanics. It serves as a model to understand the physics behind a wide range of environmental and technical processes, which silently influence everyday life. For an idealized setup, which presumes that the viscous fluid flows over an inclined or vertical substrate of infinite extent which is perfectly flat, hydrodynamic effects have been studied extensively and are well-understood. In particular, the Navier-Stokes equations can be solved analytically. The well-known Nusselt solution with its quadratic velocity profile is at hand under these idealized constraints.

Going beyond the idealized world reveals many fascinating effects, which are also essential for practical applications. The price to be paid, however, is a sharp increase in complexity. A prominent role plays, for example, the roughness of the underlying substrate. This roughness is either induced by accuracy limitations in preparation or intentionally. The influence of the substrate's undulations on the flow characteristics is tremendous and the interplay between the undulations and the flow gives rise to new phenomena, e.g., resonant standing waves and eddies. In general the flow over such inclined topographies cannot be calculated analytically in closed form from the Navier-Stokes equations. Since already small impurities on the substrate have a serious effect on the film flow and a predictable flow is required for various technical applications, e.g., curtain coating, falling film reactors, and heat exchangers, the understanding of the physical phenomena is vital. Also, most systems in the environment and technical applications have a finite extent and are bounded by, e.g., side walls which prohibit the assumption of a two-dimensional flow.

In the respected film flows the interface between the fluid and the surrounding gas is considered as a shear free, deformable boundary. Hence, waves can emerge spontaneously at the free surface if a critical volume flux is exceeded. The waves appear as the flow reacts to disturbances, like ambient noise or external forcing. On their way downstream these waves can decrease or increase their amplitude depending on the flow parameters, the underlying substrate, and the wave parameters. Similar to the substrate's undulation, the waves at the free surface drastically impact the application of film flow systems in technical facilities. Therefore, extensive experimental and computational research is inevitable to understand the flow mechanisms.

This dissertation deals with the influence of inertia and various substrate shapes on the evolution of linear, nonlinear, and turbulent free surface waves on a gravity-driven viscous film flow. The aim of this study is to follow all evolutionary steps of waves from the linear over the nonlinear to a turbulent regime and to assign accompanying phenomena to interactions of the waves and the flow. Combining the results of a wide range of experiments made it possible to reveal novel flow phenomena. In particular, the shape of the traveling free surface wave, the mechanism of wave breaking, the transition of regular wave fronts to irregular wave fronts, and the transition to a comprehensive turbulent flow will be discussed in detail and assigned to the interaction of the traveling free surface waves with the underlying steady flow.

In the first step, linear and nonlinear waves were analyzed in detail. To do so, different geometrical shapes and excitation frequencies and amplitudes were considered in the experiments.

Although sinusoidal waves were impressed in the experiments, two distinct wave shapes were found, namely convex and concave. By analyzing these wave shapes, an energy transfer from the excitation frequency to higher harmonics was inspected. The importance of the influence of the interaction between the waves and the substrate can be shown by the emergence of beat frequencies in the Fourier spectrum for undulated substrates. Additionally, particle tracking measurements of the steady state and the perturbed state unveiled major differences in the magnitude of the interaction between the traveling wave and the steady flow depending on the substrate's shape. The exact shape of the substrate is not determining the wave's shape but the shape of the steady state free surface is decisive for the evolution of the traveling free surface wave. The shape of the steady state free surface is a reaction of the flow to the underlying boundaries. Thereby, e.g., eddies have a strong impact on the flow and cause an effective substrate shape leading to the shape of the free surface.

Convectively unstable nonlinear waves are in the focus of the next study, which uncovered a completely new phenomena on gravity-driven thin film flows, namely, the wave breaking. Wave breaking in different flow configurations, e.g., at a beach, is well-known textbook knowledge. However, the physical effects provoking the wave breaking at the beach are not present in the system considered in this work. Up to now, neither experimental nor theoretical work has shown this novel phenomena for film flows and hence, there is no explanation of the physical mechanism behind it. The evolutionary behavior of nonlinear waves can be categorized in three different domains: saturation, single wave breaking, and multiple wave breaking. In the experiments, a wave frequency selection for the wave breaking was found to differ for the substrates. Along the event of wave breaking, air is encapsulated underneath the flow over the whole channel width via plunging of the wave into a trough of the steady state free surface. Due to an energetically favorable state the air encapsulation contracts to an orderly bubble. As the decisive parameter for the wave breaking mechanism the global or mean curvature of the steady state free surface was identified, due to the fact that wave breaking needs obstacles with protruding, prominent, and sufficiently high peaks. These obstacles provoke corresponding peaks on the steady state free surface which act as stumbling stones for the waves.

The subsequent study on nonlinear waves went one step further to unveil the phenomenon of the transition of regular wave fronts to irregular wave fronts. Thereby, a subdivision of the wave into a chaotic wave front and regular wave tail was found. This means that a coexistence of a regular and turbulent regime can be achieved on film flows by varying the inertia in the system. Based on the finding of the irregular wave front, an extensive study on the transition was performed. That way, the necessity of wave breaking as a precursor is revealed and a transition to turbulence in line with the Landau theory for the transition to turbulence is at hand. In this theory the state of turbulence is reached via multiple bifurcations which repeat themselves "indefinitely". The wave breaking acts as the bifurcation and new stable and unstable waves emerge from the collapse. Since wave breaking needs protruding, prominent, sufficiently high peaks as obstacles, this transition of regular to irregular wave fronts was found on strongly undulated, anharmonic, rectangular substrates.

The necessity of strongly undulated anharmonic substrates for the transition of regular to irregular wave fronts leads to the question: Can harmonic undulated substrates also show this kind of turbulence? This question was challenged with new measurements concerning a flow over a sinusoidal substrate. Within the framework of this dissertation the transition of regular to irregular wave fronts on a sinusoidal topography was not observed. Nevertheless, a transition to turbulence of the whole flow was recorded. In the experiments the transition to turbulence was observed for a sufficiently high inertia and irrespective of an external excitation.

Zusammenfassung

Eine schwerkraftgetriebene Strömung eines viskosen Flüssigkeitsfilmes über eine Schräge ist ein grundlegendes Problem im Bereich der Strömungsmechanik. Es dient als Modell, um die Physik hinter einer Vielzahl von Prozessen in der Umwelt und Technik zu verstehen, die den Alltag im Verborgenen beeinflussen. Für ein idealisiertes System, das davon ausgeht, dass die viskose Flüssigkeit über ein geneigtes oder vertikales, perfekt flaches Substrat von unendlichem Ausmaß fließt, wurden hydrodynamische Effekte umfassend untersucht und gut verstanden. Insbesondere können die Navier-Stokes-Gleichungen analytisch gelöst werden. Unter diesen idealisierten Randbedingungen findet man die bekannte Nusselt-Lösung mit ihrem quadratischen Geschwindigkeitsprofil.

Der Blick über die idealisierte Welt hinaus offenbart viele faszinierende Effekte, die auch für die praktische Anwendung unerlässlich sind. Der zu zahlende Preis ist jedoch eine stark gestiegene Komplexität. Dabei spielt beispielsweise die Rauigkeit des darunter liegenden Substrates eine markante Rolle, welche entweder durch Genauigkeitseinschränkungen in der Herstellung oder absichtlich verursacht wird. Der Einfluss der Welligkeit des Substrats auf die Strömungseigenschaften ist enorm und das Zusammenspiel zwischen der Undulation und der Strömung führt zu neuen Phänomenen, z.B. resonanten stehenden Oberflächenwellen und Wirbelbildung in den Mulden. Im Allgemeinen kann die Strömung über solche geneigten Topographien nicht in geschlossener Form analytisch aus den Navier-Stokes-Gleichungen berechnet werden. Da bereits kleine Verunreinigungen auf dem Substrat den Filmfluss erheblich beeinflussen und für verschiedene technische Anwendungen, wie z.B. Vorhangbeschichtung, Fallfilmreaktoren und Wärmetauscher, ein vorhersehbarer Fluss erforderlich ist, ist das Verständnis der physikalischen Phänomene von entscheidender Bedeutung. Darüber hinaus haben die meisten Systeme in der Umwelt und in technischen Anwendungen eine begrenzte Ausdehnung und sind z.B. durch Seitenwände begrenzt, die die Annahme einer zweidimensionalen Strömung ausschließen.

In den betreffenden Filmströmungen wird die Grenzfläche zwischen dem Fluid und dem umgebenden Gas als scherfreie, verformbare Grenze betrachtet. Somit können bei Überschreitung eines kritischen Volumenstroms an der freien Oberfläche spontan Wellen entstehen. Die Wellen erscheinen, wenn die Strömung auf Störungen, wie das allgegenwärtige Umgebungsgerauschen oder äußeren Zwang, reagiert. Auf dem Weg stromabwärts können diese Wellen in Abhängigkeit von den Strömungsparametern, dem darunter liegenden Substrat und den Wellenparametern schrumpfen oder wachsen. Ähnlich wie die Undulation des Substrats beeinflussen die Wellen an der freien Oberfläche den Einsatz von Filmflusssystemen in technischen Anlagen drastisch. Daher ist eine umfangreiche experimentelle und rechnergestützte Forschung unumgänglich, um die Strömungsmechanismen zu verstehen.

Diese Dissertation beschäftigt sich mit dem Einfluss von Trägheit und verschiedenen Substratformen auf die Entwicklung von linearen, nichtlinearen und turbulenten freien Oberflächenwellen auf einer gravitationsgetriebenen, viskosen Filmströmung. Ziel dieser Studie war es, alle evolutionären Schritte von Wellen, vom linearen über das nichtlineare bis hin zu einem turbulenten Regime zu verfolgen und begleitende Phänomene den Wechselwirkungen der

Wellen und der Strömung zuzuordnen. Die Kombination der Ergebnisse verschiedenster Experimente ermöglichte es, neuartige Strömungsphänomene zu entdecken. Insbesondere die Form der laufenden freien Oberflächenwelle, der Mechanismus des Wellenbrechens, der Übergang von regelmäßigen Wellenfronten zu turbulenten Wellenfronten und der Übergang zu einer flächendeckenden turbulenten Strömung werden im Detail diskutiert und der Wechselwirkung der laufenden freien Oberflächenwellen mit der zugrunde liegenden stationären Strömung zugeordnet.

Im ersten Schritt wurden lineare und nichtlineare Wellen im Detail analysiert. Dazu wurden in den verschiedenen Experimenten unterschiedliche geometrische Formen und Anregungsfrequenzen und -amplituden berücksichtigt. Obwohl in den Experimenten sinusförmige Wellen aufgeprägt wurden, wurden zwei unterschiedlich ausgeprägte Wellenformen gefunden, nämlich konvex und konkav. Bei der Analyse dieser Wellenformen wurde ein Energietransfer von der Anregungsfrequenz zu höheren Oberwellen untersucht. Die Bedeutung des Einflusses der Wechselwirkung zwischen den Wellen und dem Substrat kann durch die Entstehung von Schwebungsfrequenzen im Fourier-Spektrum für undulierte Substrate gezeigt werden. Darüber hinaus zeigten particle-tracing-Messungen des stationären und des gestörten Zustands große Unterschiede in der Größe der Wechselwirkung zwischen den laufenden Wellen und der stationären Strömung in Abhängigkeit von der Form des Substrats. Die genaue Form des Substrats bestimmt nicht direkt die Wellenform. Entscheidend für die Entwicklung der laufenden freien Oberflächenwelle ist die Form der stationären freien Oberfläche. Die Form der stationären freien Oberfläche ist eine Reaktion der Strömung auf die darunter liegenden Begrenzungen. Dadurch haben z.B. Wirbel einen starken Einfluss auf die Strömung und bewirken eine effektive Substratform, die zur Form der freien Oberfläche führt.

Konvektiv instabile nichtlineare Wellen stehen im Fokus der nächsten Studie, die ein völlig neues Phänomen bei schwerkraftgetriebenen Dünnschicht Filmströmungen aufdeckte: Das Wellenbrechen. Das Brechen von Wellen in sich unterscheidenden Strömungskonfigurationen, z.B. an einem Strand, ist bekanntes Lehrbuchwissen. Allerdings sind die physikalischen Effekte, die das Wellenbrechen am Strand verursachen, in dem in dieser Arbeit betrachteten System nicht vorhanden. Bisher haben weder experimentelle noch theoretische Arbeiten dieses neuartige Phänomen für Filmströmungen gezeigt, so dass es keine Erklärung für den physikalischen Mechanismus dahinter gibt. Das evolutionäre Verhalten nichtlinearer Wellen kann in drei verschiedene Kategorien unterteilt werden: Sättigung, einfache und mehrfache Wellenbrechung. In den Experimenten wurde festgestellt, dass sich eine Frequenzauswahl bei dem Wellenbrechen für die Substrate unterscheidet. Durch das Eintauchen der Welle in eine Mulde der stationären freien Oberfläche, wird während des Wellenbrechens Luft unter der Strömung über die gesamte Kanalbreite eingefangen. Um in einen energetisch günstigeren Zustand zu kommen, zieht sich der Lufteinschluss zu einer geordneten Blase zusammen. Als entscheidender Parameter für den Wellenbrechmechanismus wurde die globale oder mittlere Krümmung der stationären freien Oberfläche identifiziert. Für die Wellenbrechung werden Hindernisse mit vorstehenden, markanten und ausreichend hohen Spitzen benötigt. Diese Hindernisse provozieren entsprechende Spitzen auf der stationären freien Oberfläche, die als Stolpersteine für die Wellen dienen.

Die anschließende Studie zu nichtlinearen Wellen ging noch einen Schritt weiter, um das Phänomen des Übergangs von regelmäßigen Wellenfronten zu unregelmäßigen Wellenfronten zu enthüllen. Dabei wurde eine Unterteilung der Welle in eine chaotische Wellenfront und in einen regelmäßigen Wellenschwanz gefunden. Das bedeutet, dass eine Koexistenz von einem regelmäßigen und turbulenten Regime auf einem Filmfluss erzeugt werden kann. Basierend auf dem Befund der unregelmäßigen Wellenfront wurde eine umfangreiche Studie zu dem Übergang

durchgeführt. Auf diese Weise wurde die Notwendigkeit des Wellenbrechens als Wegbereiter aufgezeigt und ein Übergang zur Turbulenz im Sinne der Landau Theorie für den Übergang zur Turbulenz liegt vor. In dieser Theorie wird der Zustand der Turbulenz durch mehrere Bifurkationen erreicht, die sich “unbegrenzt” wiederholen. Das Wellenbrechen wirkt wie die Verzweigung und neue sowohl stabile als auch instabile Wellen entstehen aus dem Zusammenbruch. Da das Wellenbrechen markante und ausreichend hohe Spitzen als Hindernisse benötigt, wurde dieser Übergang von regelmäßigen zu unregelmäßigen Wellenfronten auf stark gewellten, anharmonischen rechteckigen Substraten gefunden.

Die Notwendigkeit von stark gewellten anharmonischen Substraten für den Übergang von regelmäßigen zu unregelmäßigen Wellenfronten wirft folgende Frage auf: Können harmonisch gewellte Substrate auch diese Art von Turbulenzen aufweisen? Dies wurde mit neuen Messungen an einer Strömung über ein sinusförmiges Substrat hinterfragt. Im Rahmen dieser Dissertation wurde der Übergang von regelmäßigen zu unregelmäßigen Wellenfronten auf einer sinusförmigen Topographie nicht beobachtet. Dennoch wurde ein Übergang zur Turbulenz der gesamten Strömung festgestellt. In den Experimenten wurde der Übergang zur Turbulenz für eine ausreichend hohe Trägheit und unabhängig von einer äußeren Anregung beobachtet.

Contents

Journal publications	3
Abstract	5
Zusammenfassung	7
1. Introduction: From the steady state to flows with chaotic free surface waves	13
1.1. The steady state	13
1.2. The linear stability	15
1.3. The wave dynamics	16
1.4. The presence of turbulence	16
1.5. Scope of this dissertation	17
2. Experimental systems and setups	19
2.1. Experimental systems	19
2.1.1. Flow facilities	19
2.1.2. Topographies	20
2.1.3. Liquid	21
2.1.4. Tracer particles and dye	22
2.2. Measurement setups	22
2.2.1. Flow rate	22
2.2.2. Steady flow	23
2.2.3. Linear stability	25
2.2.4. Wave dynamics	28
2.2.5. Single particle Tracking	30
2.2.6. Wave screening	31
3. Results and discussion	33
3.1. Wave shapes in the nonlinear regime on film flows	33
3.1.1. Motivation	33
3.1.2. Measured parameter space	34
3.1.3. Variation of the topography wavelength	34
3.1.4. Variation of the properties of the surface wave	38
3.1.5. Variation of the topography shape	39
3.1.6. Study of dimensionless parameters	41
3.1.7. Particle tracking	42
3.1.8. Conclusions	44
3.2. Wave breaking of nonlinear waves on film flows	48
3.2.1. Motivation	48
3.2.2. Measured parameter space	49
3.2.3. Steady flow	49
3.2.4. Screening different evolutionary behavior of the traveling wave	50

3.2.5. Screening different substrates and excitation frequencies	51
3.2.6. Screening the excitation amplitude	54
3.2.7. Screening the wave breaking	54
3.2.8. Screening the Fourier wave number space	56
3.2.9. Screening the wave impact	57
3.2.10. The steady state free surface as a major influencing parameter	59
3.2.11. Conclusion	59
3.3. Turbulent wave fronts on film flows	61
3.3.1. Motivation	61
3.3.2. Measured parameter space	62
3.3.3. Irregular wave shape	62
3.3.4. Evolution of traveling waves	64
3.3.5. Screening different phenomena	67
3.3.6. The magnitude of chaotic behavior	67
3.3.7. The pathway to chaos and conclusion	69
3.4. Thoughts on surface turbulence on film flows	73
4. Conclusions and outlook	75
A. Appendix	79
List of Symbols	83
List of Figures	87
List of Tables	90
References	91

1. Introduction: From the steady state to flows with chaotic free surface waves

A layer of viscous fluid flowing on a vertical or inclined substrate solely driven by gravity is denominated as a gravity-driven viscous film flow. Gravity-driven film flows can be seen in nature on inclined roads during strong rain, avalanches [1], debris flow [2], moving glaciers [3], biofilms [4], bubbles [5], lachrymal fluid, and tear films [6]. Emerging surface waves on the viscous film flow can play a crucial role in nature and in technical applications. The dynamics of surface waves can drastically influence the functionality of technical devices and may either enhance or impair their performance. Examples are heat exchangers [7,8], distillation processes [9,10], and coating technologies [11–13]. In heat exchangers with a falling film, free surface waves amplify the efficiency of the thermal transmission. Conversely, most coating applications require a smooth surface which makes it indispensable to suppress surface waves. The interest in nature and technical application led the scientific community to work in the field of gravity-driven free surface waves and their dynamics.

In Chapter 1, the basics behind gravity-driven films flowing over flat and undulated substrates will be shown and discussed.

1.1. The steady state

One of the groundbreaking works on film flows was done by Wilhelm Nusselt. In 1916, he solved the Navier-Stokes equations analytically for a flow with infinite extent over a perfectly flat substrate [14]. Thereby, he revealed the quadratic dependency of the velocity on the distance to the substrate. The solution has some constraints, as Nusselt assumed the system to be steady, the shear stress at the free surface of the flow to be zero, the velocity field to be unidirectional, and the velocity to depend only on the distance to the flat substrate. The requirement of a flat substrate and a flow of infinite extent is never met in physics and real life applications. In the example of heat exchangers, rough surfaces increase the area of the heat exchange and enhance the efficiency.

Nusselt's condition of an infinite extent cannot be fulfilled in technical applications. Instead, side walls confine the two-dimensional film flow, which leads to new physically important phenomena in the system. Prominent three-dimensional features of the velocity field and the free surface shape are caused by the no-slip condition and the capillary rise at the side walls. The no-slip condition induces a zero velocity at the side walls and the capillary rise leads to a significantly higher film thickness near the side walls leading to a velocity overshoot in the vicinity of the side walls. These results were experimentally, numerically, and analytically shown by the group of Aksel [15,16]. By thinning the film, a transition from a film flow to a corner flow was observed by finding a film rupture in the middle of the channel [17].

The interest on gravity-driven channel flows over undulated topographies has risen in the last years, since technical applications often depend on the undulations. Nevertheless, the number of experimental publications on this topic is relatively low due to various technical difficulties,

which mostly result from curved liquid boundaries and the resulting poor optical accessibility. For very small undulations compared to the film thickness the shape of the steady state free surface is already drastically altered. Pozrikidis and Thoroddsen [18] studied the shape of the free surface of a liquid film flowing down an inclined plane over a particle captured on the wall, whereas the particle size is much smaller than the film thickness. The influence of two-dimensional rectangular step-up-step-down and trench geometries on the free surface shape of a thin water film was analyzed by Decré and Baret with phase-stepped interferometry [19]. These kinds of geometries have also been studied by using an integral boundary method on a Stokes flow [20], analytically via a Green function of the linearized problem [21], and by using a lubrication approximation [22, 23]. Aksel [24] analytically, numerically, and experimentally examined the effect of capillarity on the free surface shape and velocity of a flow over an inclined plane with an edge. The publications [18–22, 24] show a ridge of the free surface in the vicinity of step-downs of the substrate and a depletion of the free surface near step-ups. The magnitude of these features is dictated by four pertinent parameters, the depth, width and steepness of the trenches, and the capillary pressure at the free surface of the flow. For the case of creeping flows, the volume of the depletion and ridge are equal, which Scholle and Aksel [25] proved analytically. The influence of a sinusoidal substrate at a vertical wall on the heat and mass transfer characteristics was studied by Negny *et al.* [26].

Gravity-driven viscous flows over periodical undulations, such as the sinusoidal substrate mentioned before, were investigated extensively [15, 27–54]. For different kinds of flows the influence of the underlying undulations on the free surface shape varies. In the case of creeping flows the amplitude of the free surface waviness decreases with an increasing film thickness [15, 27, 28]. Increasing the Reynolds number for laminar flows with sufficiently high inertia shows two types of changes. First, the amplitude of the free surface shape increases for Reynolds number below a certain threshold. Second, the amplitude of the free surface shape decreases with further increase of the Reynolds number beyond this threshold [28–30]. The critical Reynolds number, which provokes the highest amplitude of the free surface shape, depends on the film thickness, the geometry, and the hydrostatic and capillary pressure. These dependencies are only valid for small amplitudes of the underlying waviness since the nonlinear terms in the governing equations are neglected. In the case of higher undulations the resonance Reynolds number is shifted to higher values since higher harmonics in the free surface shape appear [31–33, 41]. Wierschem *et al.* [34, 35] compared different theoretical perturbation approaches with experiments on thin films over weak and strong sinusoidal undulations and thick films over weak sinusoidal undulation. Despite seeing resonant waves of the free surface also humps, shocks, and surface rollers were observed [36]. The improvement in computational power facilitated computations for three-dimensional systems as these are interesting for real world problems [37–40].

The underlying undulation of the flow dictates the shape of the free surface, which is in line with the normal cause-to-effect paradigm. In recent years, the interest in the inverse problem increased. The inverse problem states that an observable, like the shape of the free surface or the velocity field, is given and has to be related to unknown flow quantities, i.e., flow conditions, material properties or unknown boundaries [55]. Multiple publications are dealing with the inverse problem [41, 56–62]. Nevertheless, an uncertainty in the inverse problem remains since different substrates with the same wavelength and amplitude can exhibit barely distinguishable free surface shapes when recirculation areas appear as shown by Schörner *et al.* [63].

The recirculation areas or eddies were found by inspecting the velocity field for a Stokes flow over undulations with boundary integral formulation by observing a reversal flow in the troughs of the geometry [27]. Scholle *et al.* [64] showed that eddies in creeping flows act as a “fluid

roller bearing”. Furthermore, it was analytically shown that the film thickness is the crucial parameter for the emergence of eddies in a creeping flow [65]. These results are in line with the experiments by Wierschem *et al.* [66]. By solving the Navier-Stokes equations numerically, Trifonov also found eddies in a flow when inertia is considered [29]. In a film flow where inertia is considered, the size of the eddies increases and the eddy is tilted [67–69]. Eddies are found in flows over various geometrical shapes, i.e., sinusoidal, rectangular, saw-tooth [31, 63, 70, 71]. Wierschem *et al.* [70] showed that eddies can be suppressed at moderate Reynolds numbers, when the amplitude of the free surface is amplified by resonance. Scholle *et al.* [72] showed that eddies can increase the heat transfer between the substrate and the free surface of the film flow.

1.2. The linear stability

The film flows considered in this work exhibit a free surface since they are not bound by a rigid wall and are hence susceptible against free surface perturbations. This was found by Sergei and Pjotr Kapitza in groundbreaking experiments [73, 74]. In their pioneering experiments they observed spontaneously traveling free surface waves on a flow over a flat substrate when the volume flux exceeds a certain threshold. The results of the Kapitza family led to numerous publications on the topic of linear stability on film flows. Benjamin [75] and Yih [76] found that Nusselt’s solution of the Navier-Stokes equations is unstable against long-wave perturbations above a critical Reynolds number. They adapted the Orr-Sommerfeld equation [77–79] on thin film flows and found the critical Reynolds number to be $Re_c = 5/4 \times \cot \alpha$ for a flow over a flat substrate, whereas α represents the inclination angle. These results are valid for infinitely long, linear free surface perturbations with a wave number and amplitude tending against zero. In experiments this critical Reynolds number and the long-wave type instability was confirmed by Liu *et al.* [80] and Liu and Gollub [81]. The flow was denoted as “convectively unstable” above the critical Reynolds number against these disturbances.

The results from the computations were gained for a two-dimensional film flow. However, in technical applications and real world problems the flow is bounded by sidewalls. The no-slip condition and the capillary rise at the sidewalls is found to be stabilizing on the film flow [82, 83]. Furthermore, a transition from the classical long-wave instability to a short-wave instability was observed by Pollak *et al.* [84].

Vlachogiannis and Bontozoglou [32] and Argyriadi *et al.* [33] tested the stability of free surface disturbances over weak rectangular, periodic bottom undulations with a fluorescence imaging method. They found a remarkable stabilization of the flow at high Reynolds numbers and an increase of the stability threshold with the corrugation steepness. A stabilization of the flow against disturbances was also found for sinusoidal bottom undulations analytically by Wierschem and Aksel [85]. Their results were proven experimentally by Wierschem *et al.* [35] and they also showed that the shape of the neutral curve qualitatively remains unaffected. Trifonov also tested the stability of the flow against disturbances by numerically solving the Navier-Stokes equations [86–88] and found that the flow is significantly stabilized if the mean film thickness drastically increases by the undulations compared to the film thickness of the corresponding Nusselt flow.

For the case of steep bottom undulations stabilizing and destabilizing results were found depending on the amplitude and wavelength of the substrate and the surface tension [41, 89–91]. More publications show the stabilizing and destabilizing effect of steep undulations [92–99]. Heining and Aksel [89] were the first to numerically show a completely new phenomenon by

publishing a segmented stability chart with an unstable isle. They discarded their new finding as an artifact from the linearization. They used an integral boundary layer model to analytically and numerically reveal this phenomenon. However, their finding was experimentally [92] and numerically [93] proven. Schörner *et al.* [95] were able to link the unstable isle to resonance phenomena of the steady state film flow. Different types of stability charts were discovered over the time and a universal pathway for the stability of films over topography was unveiled [98]. The topic of film flows over topography concerning the linear stability is nicely reviewed by Aksel and Schörner [100].

1.3. The wave dynamics

The evolution and dynamics of waves over flat substrates have been studied elaborately. These waves emerged due to instability of the flow or external forcing. The studies mostly treat linear waves with a vanishing amplitude – for nonlinear waves with a non-zero amplitude new models had to be derived [101–110]. Chang and Demekhin reviewed the topic in their book [111].

Nonlinear waves were also analyzed experimentally and numerically [80,81,112–122]. The works concentrate on the evolution and the saturation (steady state) of waves flowing down an inclined channel. A rich diversity of waves was observed and reviewed by Craster and Matar [123] and Chang [124]. The variety of waves was reduced to two main categories: Solitary waves which are disjoint by large areas of a quasi steady state flow and nearly sinusoidally shaped waves of small wavelength and wide peaks. The solitary waves are mostly accompanied in front by depletion regions called capillary waves. The aforementioned saturation of the waves was observed for both wave categories. Reck and Aksel [125] found surface rollers in solitary waves over a flat substrate in an inclined open channel, which might explain the stability of the steady state of the waves.

The above-mentioned saturation was also seen experimentally by Reck and Aksel [126] and numerically by Trifonov [97] for waves on a flow over an undulated substrate. Yet, the influence of substrate undulations on free surface waves is barely analyzed and little is known. Some experimental and numerical research deals with the influence of the undulated substrate on the free surface waves [33, 86, 91, 126, 127]. To describe the waves, they are viewed as two individual parts in superposition. First, the wavy steady state free surface which is a result of the undulated substrate. Second, the proceeding unsteady wave which travels on top of the steady state wave. The unsteady wave's amplitude and shape depends on the position of the wave in a substrate's undulation pattern.

1.4. The presence of turbulence

In the field of fluid mechanics two distinct transition schemes to turbulent states are known, yet not fully understood. Prominent examples are the transitions of the Hagen-Poiseuille flow and the Bénard problem. These two examples show different transition behavior. First, the transition to turbulence of the Hagen-Poiseuille flow was classically said to be spontaneous [128], yet new research suggests that the transition elapses with intermediate steps [129]. The classical type of spontaneous transition can be seen in film flows as the steady state can become unstable and breaks into a three-dimensional flow [130–136]. This transition can occur for the steady flow with or without external forcing. Second, the transition to turbulence in the Bénard problem

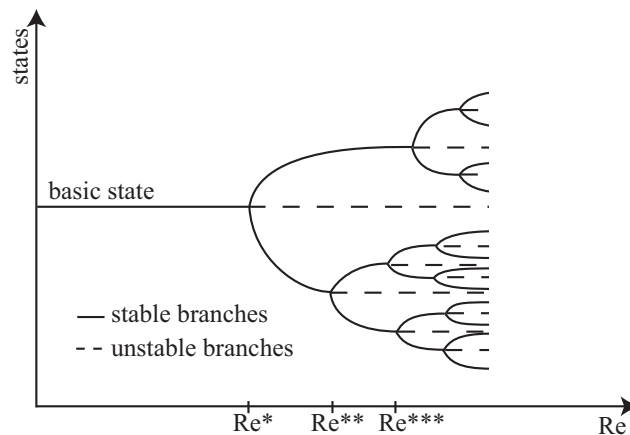


Figure 1.1.: Schematic response diagram of Landau theory for the transition to turbulence. Multiple bifurcations are shown at different values of the control parameter $Re^{*/**/**}$. This scheme is modified and reprinted from [138].

proceeds via bifurcation of the states which is in line with the Landau theory for transition to turbulence [128, 137].

In Figure 1.1, a schematic response diagram for the Landau theory for the transition to turbulence is displayed. For a small driving (control) parameter (in this case the Reynolds number) a unique stable steady state (basic state) is present. At a critical value of the driving parameter Re^* the steady state bifurcates and traveling waves are supported by one or more wavelengths. Beyond this critical value traveling waves can grow and the steady flow is considered as unstable. Nevertheless, new stable, possibly unsteady solutions can branch for $Re \geq Re^*$ and the flow remains stable until the next bifurcation ($Re = Re^{**}$). This branching can repeat itself indefinitely as the driving parameter increases and more unstable solutions appear. After many such bifurcations the state of turbulence is reached [138].

1.5. Scope of this dissertation

The present dissertation deals with the evolution and dynamics of linear, nonlinear, and turbulent traveling free surface waves over different types of topographies. Various measurement techniques were combined for a comprehensive study on nonlinear and turbulent waves. Thereby, new flow phenomena were revealed and attributed to different flow characteristics. The aim of this work is to study the evolution of forced perturbations along all evolutionary steps. The evolution from nonlinear to turbulent waves is the main subject of this study.

The dissertation is structured as follows: In Chapter 2, all experimental setups and techniques, which were used to characterize the flow and the perturbations are presented. The new findings on the evolution of mainly nonlinear waves are shown in Chapter 3. This Chapter is subdivided in four parts. In Section 3.1, the regular evolution of nonlinear waves concerning the wave's shape is examined. A new phenomenon on film flows, namely wave breaking, and the accompanied bubble formation is presented in Section 3.2. In the subsequent Section 3.3, the transition of regular wave fronts to irregular wave fronts is investigated in detail. Section 3.4 deals with different turbulent regimes on gravity-driven thin film flows. A summary is presented in Chapter 4 and completes the dissertation.

2. Experimental systems and setups

2.1. Experimental systems

Gravity-driven viscous thin film flows down an inclined open channel with periodic topographies were tested. As a reference measurement the flow over the flat substrate was also studied. The flow facilities, the topographies, and the liquid with the solved dye and tracer particles characterize the experimental systems.

This Chapter is based on the publications [63, 84, 92, 95, 98, 126, 139–144].

2.1.1. Flow facilities

In Figure 2.1, a sketch of the flow facilities is shown. The tempered oil from the liquid reservoir was pumped into the inflow tank at the inlet of the inclined open channel. All experiments were performed in one channel with a width $b_c = (170 \pm 1)$ mm and length $l_c = (2100 \pm 1)$ mm. The flat substrate of the channel was bordered by transparent, planar Plexiglas[®] sidewalls. Exchangeable substrates were placed on top of the flat bottom plate. The channel was inclined against the horizontal axis by the inclination angle α , which could be adjusted continuously between 0° and 90° and checked with a *Mitutoyo Pro 360 Digital Protractor 950-315* with a reading precision of 0.1° . A leveling of the direction perpendicular to the flow direction was conducted with a spirit level type *Pro 360*, also from *Mitutoyo*. Any twisting of the channel was eliminated with adjustment screws which were attached to the mount of the channel on the vibration isolating table.

The temperature of the oil was kept constant with a heat exchanging coil in the liquid reservoir by a heating bath *Thermo Haake TC300* which was linked to a temperature sensor *Almemo 4290-7* attached to the outflow inside the channel. The temperature was kept constant at $\theta = (23.0 \pm 0.1)^\circ\text{C}$ during all measurements and was regulated by a custom *LabView* program. In Figure 2.2, the measured liquid temperature θ is plotted for a five hour measurement. The temperature in the lab was controlled by two air conditioners.

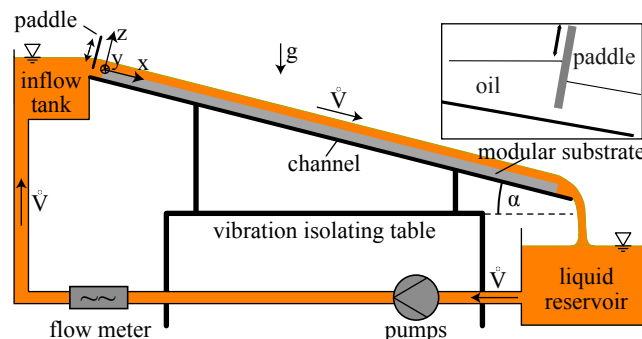


Figure 2.1.: Sketch of the flow facilities and the flow circuit used in the experiments. The inlay shows the impounded oil behind the paddle. Modified and reprinted with permission from Dauth and Aksel [144]. © Springer Nature.

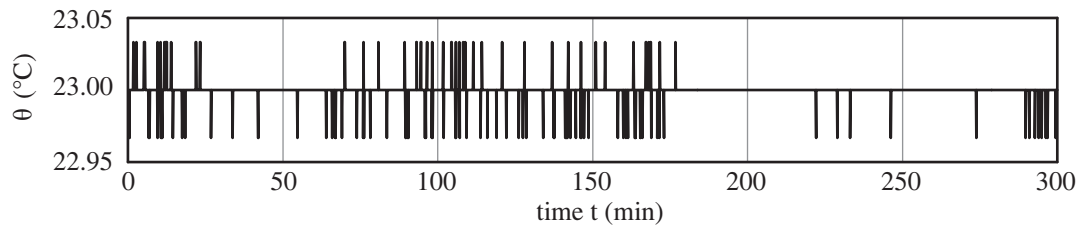


Figure 2.2.: The measured temperature θ for a five hour measurement.

A constant volume flux \dot{V} was provided by two eccentric screw pumps type *AFJ 15.1B/2B* from *PF Jöhstadt*. The volume flux \dot{V} could be regulated up to $580 \text{ cm}^3/\text{s}$ by varying the angular frequency of the pumps. Furthermore, a bypass yielded the opportunity to continuously change the volume flux.

Periodic perturbations on the steady film flow were induced by a linear motor from *LinMot* type *E1250-IP-UC/V1RE* which was attached to the inflow of the channel. The excitations on the flow could be continuously adjusted in form of the excitation frequency between $0.5 \text{ Hz} \leq f_e \leq 15.0 \text{ Hz}$ and the peak-to-peak paddle amplitude A_e . In case of measurements on nonlinear traveling free surface waves the paddle amplitude was set to $A_e = 8.0 \text{ mm}$ except otherwise stated. For linear waves the paddle amplitude was minimized in order to achieve almost vanishing small wave amplitudes. The inlay in the sketch of the flow facilities (Figure 2.1) shows the mechanism of wave generation. The oil is impounded behind the paddle and released by the sinusoidal up- and downward motion of the paddle.

2.1.2. Topographies

In Section 2.1.1, it was described that differently shaped inlays were tightly bound in the channel. In Figure 2.3 (a), a sketch of an inclined substrate and its specific parameters is shown. The substrate's wavelength λ_b , the length of the topography's top and bottom of the trench W and L , the amplitude A , the inclination angle α , and its specific *shape* are characterizing the substrate.

The different substrate shapes are shown in Figure 2.3 (b). The undulation amplitude was fixed for all topographies to $A = 8.0 \text{ mm}$. For the sinusoidal and sawtooth-like substrate the topography's wavelength was fixed at $\lambda_b = 20 \text{ mm}$. In the case of the rectangular substrate a modular building block system was used, see Figure 2.3 (c). The length of the topography's

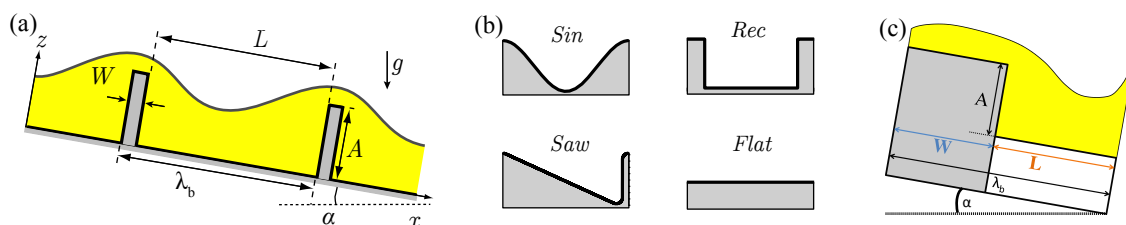


Figure 2.3.: (a) Geometry and notations of the viscous film flow over the inclined topography. (b) Sketch of the specific shapes of the topography, i.e., sinusoidal (*shape = Sin*), sawtooth-like (*Saw*), rectangular (*Rec*) and flat (*Flat*). (c) Sketch of the modular rectangular substrate (*Rec*). The main flow direction is from left to right. Modified and reprinted with permission from Schörner and Aksel [98] and Dauth and Aksel [144]. © AIP Publishing & Springer Nature.

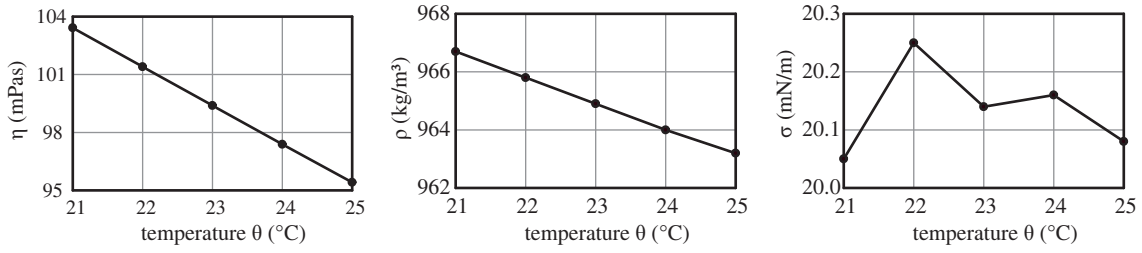


Figure 2.4.: The dynamic viscosity η , density ρ and surface tension σ for the *Elbesil* silicon oil blend.

top of the trench W was varied from 1 to 30 mm. The length of the topography's bottom of the trench L was varied from 9 to 99 mm. The flat substrate was considered as the borderline cases for all substrates with either W , L or $\lambda_b = \infty$. In the experiments the inclination angle α was varied between 5° and 30° .

2.1.3. Liquid

In the experiments a blend of *Elbesil* silicon oils was used as the fluid. The oil showed Newtonian behavior within the shear rates and temperature range considered in the measurements and was denoted as *Elbesil 100*. The main fluid properties namely the dynamic viscosity η , density ρ and surface tension σ were measured in the temperature range between 21°C and 25°C in 1°C steps. The results are shown in Figure 2.4. From the dynamic viscosity and the density the kinematic viscosity $\nu = \eta/\rho$ was calculated.

The dynamic viscosity η was measured with different Ubbelohde viscosimeter capillaries type 501 from *Schott* which were plunged into a water bath, whose temperature was controlled by a thermostat from *Schott*. The accuracy of the temperature of the heating bath was 0.05°C and the precisions of the viscosimeter capillaries were specified to be between 0.65% and 0.80%.

A Mohr Westphal balance from *Kern* was used to determine the density ρ of the silicon oil. A thermostat type *ecoline RE204* from *Lauda* controlled the temperature of the oil in the balance during the measurement.

The surface tension σ was obtained by a ring-tensiometer type *TE1CA-M* from *Lauda* whose fluid temperature was controlled by a thermostat type *RC 6 CP* from *Lauda* during these measurements.

The fluid properties are listed in Table 2.1 for the measurement temperature $\theta = (23.0 \pm 0.1)^\circ\text{C}$.

The Kapitza number describes the ratio of surface tension forces to inertial forces [111], is listed in Table 2.1, and calculated as:

$$Ka = \frac{\sigma}{\rho g^{1/3} \nu^{4/3}}. \quad (2.1)$$

Notation	η (mPas)	ρ (kg/m ³)	σ (mN/m)	ν (mm ² /s)	Ka
<i>Elbesil 100</i>	99.4 ± 0.3	964.9 ± 0.2	20.1 ± 0.1	103.0 ± 0.3	2.02 ± 0.02

Table 2.1.: Liquid properties and Kapitza number of the *Elbesil* silicon oil blend used in the experiments at the measurement temperature $\theta = (23.0 \pm 0.1)^\circ\text{C}$.

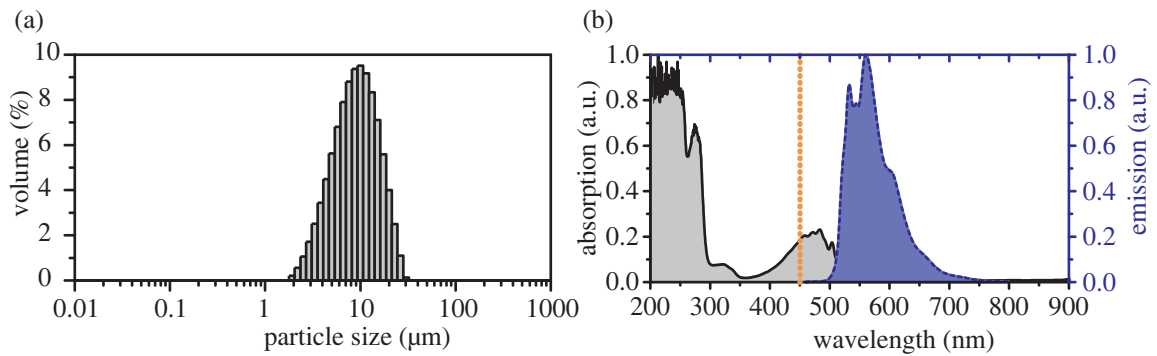


Figure 2.5.: (a) Weighted particle size distribution of the tracer particles type *80A601* from *Dantec*. (b) Absorption and emission spectra of *Quinizarin*, which was dissolved in *Elbesil* oil. Black solid line: absorption spectrum. Blue dashed line: emission spectrum for excitation at 450 nm (orange dotted line).

2.1.4. Tracer particles and dye

For the measurements, which are described in Section 2.2, the silicon oil had to be seeded with glass spheres and mixed with a fluorescent dye. The hollow glass spheres type *80A601* from *Dantec* were used as tracer particles and faithfully followed the wave and flow dynamics. The volume weighted particle size distribution was measured with a *Mastersizer 2000* laser diffraction particle size analyzer from *Malvern Instruments*. In Figure 2.5 (a), the size distribution is plotted. The median particle size was $d_{V,50} = 9.64 \mu\text{m}$ and the grade of dispersity [145] was $\xi_d = (d_{V,84} - d_{V,16}) / (2d_{V,50}) \approx 0.45$. The quantities $d_{V,j}$ denote the particle sizes, which were greater than or equal to $j\%$ of all particles. The manufacturer’s data sheet indicated a mean particle diameter $d_p = 10 \mu\text{m}$ and density $\rho_p = 2230 \text{ kg/m}^3$. The sedimentation speed can be calculated in line with Happel and Brenner [146] to $w_{sed} = d_p^2 g (\rho_p - \rho) / (18\eta)$ which yields $w_{sed} = 6.94 \times 10^{-4} \text{ mm/s}$ for the silicon blend used in the experiments. This velocity is several orders of magnitude smaller than the velocities of the different flows considered.

An organic compound *Quinizarin* from *Sigma-Aldrich* was dissolved in the silicon oil and was used as a fluorescent dye. The spectral properties namely the absorption and emission spectra for an excitation at 450 nm are displayed in Figure 2.5 (b). The absorption spectrum was recorded with a *Lambda 750 UV/Vis/NIR* spectrophotometer from *PerkinElmer*. The emission spectrum for the 450 nm excitation was measured with a *Cary Eclipse* fluorescence spectrophotometer from *Agilent*. The data was recorded in 0.5 nm steps.

2.2. Measurement setups

The description of the measurements setups in this Section is based on the publications [63, 84, 92, 95, 98, 126, 139–144].

2.2.1. Flow rate

The overall volume flux \dot{V} which was produced by the two eccentric pumps, explained in Section 2.1.1 and exemplarily shown in Figure 2.6 for a five hour measurement, was measured with an ultrasonic flow meter type *Deltawave C* from *Systec controls*. The flow meter was mounted on the pipe between the pumps and the inflow tank. Occasionally, the measurement of the flow meter was counterchecked with an analog flow meter type *RW-RD 40* from *Aqua Metro*, which was mounted on the outflow of the channel.

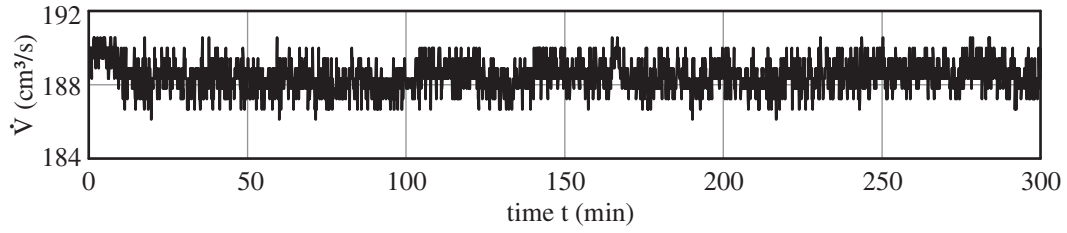


Figure 2.6.: The measured volume flux \dot{V} for a five hour measurement.

The overall volume flux was used to calculate the two-dimensional flow rate $\dot{q}_{2D} = \dot{V}/b_c$, which is assumed to be constant over the whole width of the channel. The no-slip condition and the capillary rise effect caused by the sidewalls provoke a dependency of the flow rate on the spanwise y -coordinate $\dot{q}_{3D} = \dot{q}(y)$. Scholle and Aksel [15] analytically calculated the flow rate for flat substrates $\dot{q}_{3D}(y)$ and showed that the deviation from the flow rate at the channel center $\dot{q}_{3D}(b_c/2)$ and the present calculated flow rate $\dot{V}/(b_c)$ is less than 1%. In case of undulated substrates no similar study exists hence it was assumed that a similar behavior is at hand.

With the assumption of the quasi two-dimensional flow the Reynolds number [147] can be defined as

$$Re = \frac{h_n u_{s,n}}{\nu} = \frac{3\dot{V}}{2\nu b_c} \quad (2.2)$$

for the corresponding Nusselt flow [14] with the film thickness h_n , the free surface velocity $u_{s,n}$ and the parabolic velocity profile $\vec{u}(z)$. The required characteristic length and velocity can be directly calculated by analytically solving the Navier-Stokes equations and are given in equations 2.3:

$$h_n = \sqrt[3]{\frac{3\nu\dot{V}}{g b_c \sin \alpha}}, \quad u_{s,n} = \sqrt[3]{\frac{9\dot{V}^2 g \sin \alpha}{8\nu b_c^2}}, \quad \vec{u}(z) = \frac{g \sin \alpha}{2\nu} (2h_n - z) z \vec{e}_x. \quad (2.3)$$

2.2.2. Steady flow

The measurement technique for the detection of the steady state free surface $h_0(x)$ of the film flow is shown in Figure 2.7. In order to uncover $h_0(x)$ the fluorescent dye *Quinizarin* was dissolved in the silicon oil, as described in Section 2.1.4. This organic compound was excited in the center of the channel in the x - z -plane by narrow laser lines from at least two 70 mW lasers type *FP-MVmicro-450-70-10-F* by *Laser Components*. The laser lines were overlaid and the lasers were mounted in their working distance from the oil surface, see Figure 2.8. The continuous laser emission had a central wavelength of 450 nm.

The fluorescence of the liquid was recorded with a high-speed camera *CR600x2* from *Optronis* (camera 1 in Figure 2.7 and 3 in Figure 2.8) with a spatial resolution of $20 \mu\text{m}/\text{pixel}$ and a size of the image in x -direction of $x_c \approx 28 \text{ mm}$. Scattered incident laser light was blocked from the camera with an appropriate optical longpass filter with a 50% cut-off wavelength of 550 nm. In order to avoid distortion from the capillary rise and side wall effects, the camera was inclined with respect to the y -axis by 20° . An exemplary image of the steady state flow over a rectangular substrate is shown in Figure 2.9 (a). The perspective view was corrected

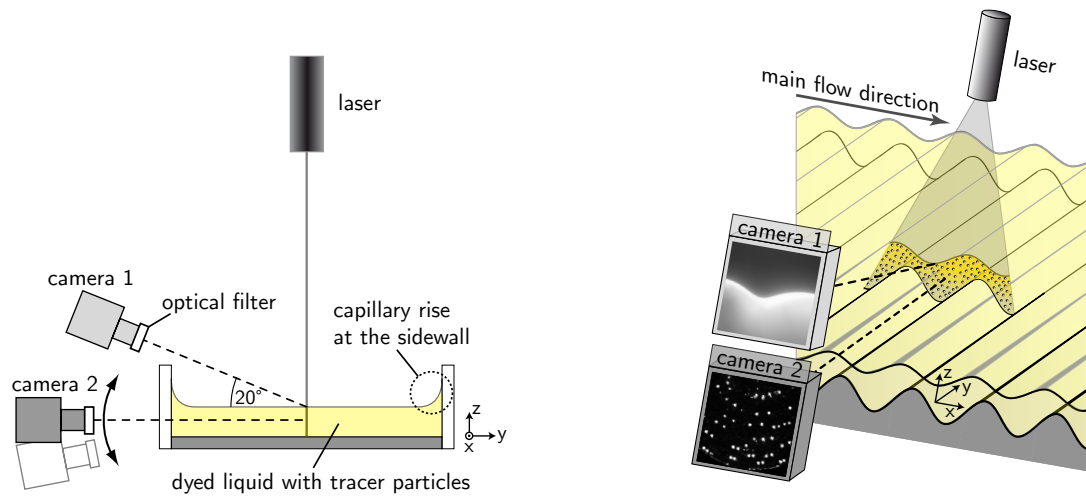


Figure 2.7.: Experimental setups for the measurements of the free surface shape of the steady film flow (Section 2.2.2), the free surface shape of the perturbed film flow (Section 2.2.4) and the flow field structure of both steady and perturbed film flow (Section 2.2.5). The steady and perturbed free surfaced were illuminated by multiple blue diode lasers and recorded by camera 1. The flow field structures were revealed by single particle tracking measurements. Tracer particles mixed in the silicon oil were illuminated with a red line laser and recorded by camera 2 which position was adaptable for the measurements. Modified and reprinted with permission from Schörner *et al.* [95]. © AIP Publishing.

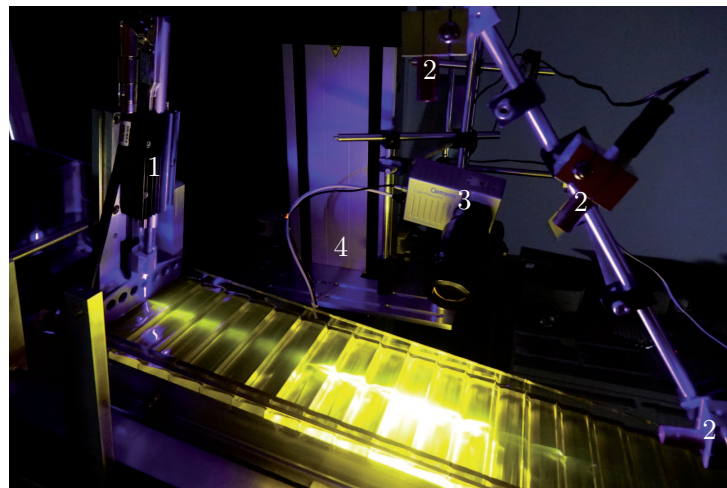


Figure 2.8.: Experimental setup for the steady flow and wave evolution/dynamics: [1] linear motor with paddle to generate waves, [2] three 70 mW line lasers to illuminate the oil, [3] high-speed camera, and [4] traversing unit. Modified and reprinted with permission from Dauth and Aksel [144]. © Springer Nature.

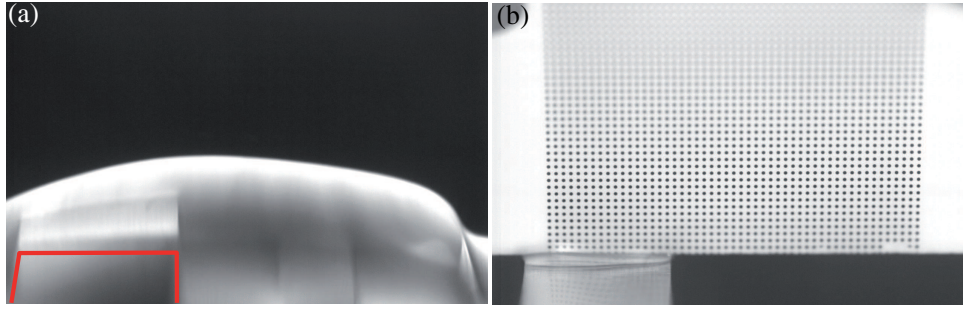


Figure 2.9.: (a) Exemplary image of the steady state flow over a rectangular substrate with $W/L = 10/30$ and $Re = 16$. The substrate's contour is marked with a red line. (b) Image of the calibration plate that was used to correct the perspective view from above. The dots on the ceramic plate have a diameter of 0.25 mm and a distance of 0.5 mm.

with a calibration, see Figure 2.9 (b). With the help of the calibration picture each pixel was assigned to a position in the x - z -plane.

In order to process the recorded images, an edge-detection algorithm was developed in *MatLab*. The steps described in the following can be partially seen in Figure 2.10. First, a Gaussian filter was applied to get rid of the high frequency noise. Second, for every column the brightness function was read out, exemplarily shown for one column in Figure 2.10 (b) [the column is indicated by the dotted orange line in Figure 2.10 (a)]. Third, the first and second derivative of the brightness function are calculated for each column. In order to find the maximum of the first derivative the second derivative was used. The first derivative for the exemplary column is plotted in Figure 2.10 (c). The z -coordinate of the maximum of the first derivative of the brightness function represents the steady state free surface $h_0(x)$, i.e., the upper boundary of the flowing silicon oil. Now, all columns have to be recombined to the steady state free surface, which is plotted as a red line in Figure 2.10 (a).

2.2.3. Linear stability

In order to gain information on the flow's linear convective instability, a measurement setup and technique related to preceding approaches was used [35, 63, 80, 84, 92]. The experimental setup used is shown in Figure 2.11. As displayed there, a paddle is mounted at the inlet of

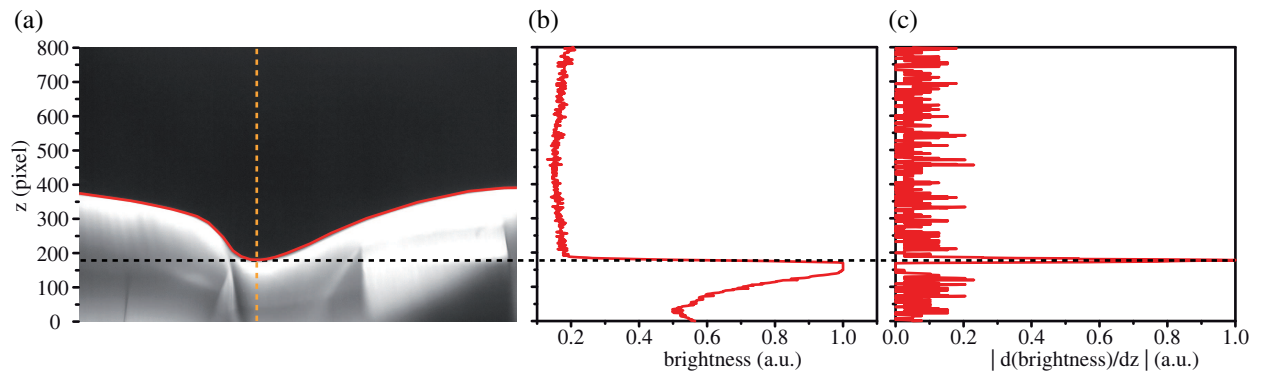


Figure 2.10.: Determination of the steady state free surface of the flow over a rectangular substrate with $W/L = 10/30$. (a) One exemplary image. (b) The brightness function plotted for the pixel coordinate indicated with the dotted orange line in (a). (c) The first derivative of the brightness function.

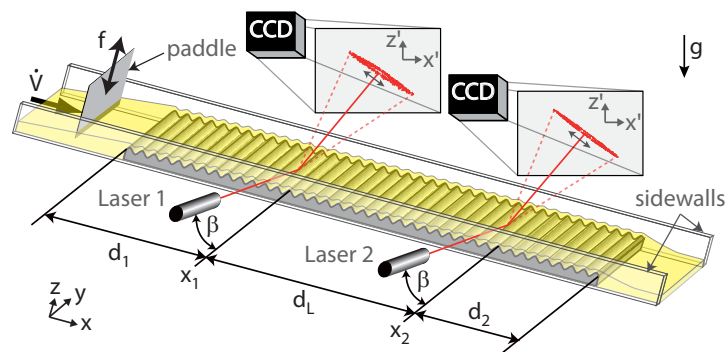


Figure 2.11.: Experimental setup for the measurements of the convective free surface instability. Modified and reprinted with permission from Schörner *et al.* [63]. © AIP Publishing.

the channel in front of the topography and was tightly fitted in the channel. The paddle was permanently dipped into the silicon oil and continuously oscillated in a sinusoidal motion in the z -direction with a small peak-to-peak paddle amplitude $A_e \leq 0.5$ mm. The paddle was driven by a linear motor type *E1250-IP-UC/V1RE* from *LinMot*, as described in Section 2.1.1. With the up- and downward motion of the paddle the impounded silicon oil is periodically released and the volume flux \dot{V} of the steady state flow was varied leading to time-periodic, small traveling free surface waves with a frequency between $0.5 \text{ Hz} \leq f_e \leq 15.0 \text{ Hz}$ and an amplitude $a_w < 0.1$ mm [126, 139]. Due to the small wave amplitude the waves can be considered as linear waves [98, 126, 139].

For probing the stability of the flow against these free surface perturbations two diode lasers type *FP-D-635-5-C-F* from *Laser Components* were mounted at the streamwise coordinates x_1 and x_2 . The positions x_1 and x_2 were appropriately chosen to exclude inflow and outflow effects [92] and to avoid a corruption of the measurements due to an insufficient distance $x_2 - x_1$. Both lasers were parallel fixed in the y - z -plane with an inclination of $\beta = (20 \pm 2)^\circ$ against the y -axis. The stability of the flow against free surface perturbations was probed in the middle of the channel $y = b_c/2$, hence the laser spots hit the free surface on a crest of the topography in the channel center. After an optical path of at least 3 m the reflections of the laser spots hit a screen. Whenever a traveling free surface wave passes the reflection spots in the channel the reflections on the screen starts oscillating. The amplitude of the oscillation of the reflections is proportional to the amplitude of the traveling free surface wave at its respective position in streamwise direction. To be more precise, the maximum slope $2\pi a_w / \lambda_w$ of the free surface contour of the traveling wave at the respective position x_i is proportional to the oscillation amplitude of the laser spots on the screen.

The screen was captured with a CCD camera type *DMK 31BU03* from *IC Imaging* with a frame rate of 30.0 Hz. Each laser spot was recorded 512 times and processed with a Gaussian filter to reduce image noise, whereas the threshold was set to 80% of the brightest pixel. The center of the sharp-edged spot was calibrated in space with a reference calibration image in order to avoid distortions from a perspective view. The inlays in Figure 2.11 show the position of the laser spot in the x' - z' -plane and were denoted as

$$\mathbf{p}_i(t) = (p_{x',i}(t), p_{z',i}(t)), \quad i = \{1, 2\}. \quad (2.4)$$

In Figure 2.12 (a), a typical example for the recorded pathlines $\mathbf{p}_i(t)$ is given. Figure 2.12 (b) shows an excerpt of the x' - and z' -components of the time-dependent positions of the laser

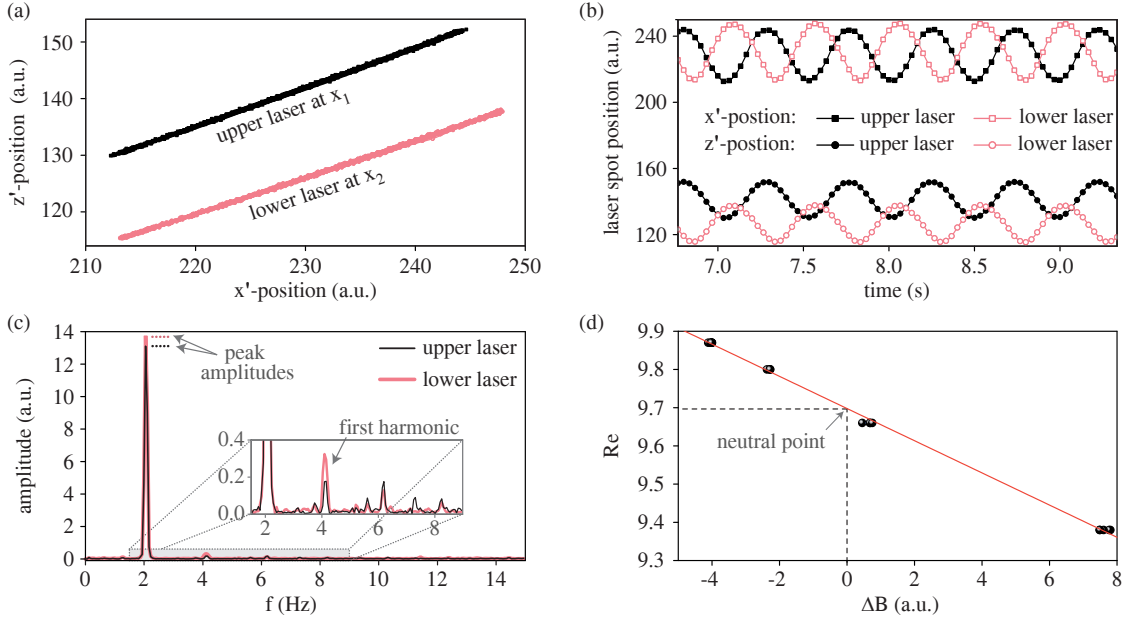


Figure 2.12.: (a) Positions of the spots of the upper laser (black) and the lower laser (rose) on the screen. (b) Excerpt of the x' - and z' -components of the time-dependent positions (a) of the laser spots. (c) Absolute values of the Fourier transformed signals of the laser spots of the measurement shown in (a) and (b). (d) Dependence of the amplitude difference ΔB on the Reynolds number. The example shown in (a) - (d) corresponds to Re_c , $A = 8$ mm, $L = 19$ mm, $W = 1$ mm and $\alpha = 21^\circ$. In (a) - (c), $Re = 9.66$ and $f_e = 2.05$ Hz. In (d), the Reynolds number was varied while $f_e = 2.05$ Hz and all other system parameters were kept constant. Modified and reprinted with permission from Schörner [141].

spots. This leads to the Fourier transformed signals

$$\hat{\mathbf{p}}_i(f') = (\hat{p}_{x',i}(f'), \hat{p}_{z',i}(f')) = (\mathcal{F}(p_{x',i}(t)), \mathcal{F}(p_{z',i}(t))) \quad (2.5)$$

and their absolute values

$$\hat{p}_i(f') = \sqrt{\hat{p}_{x',i}^2(f') + \hat{p}_{z',i}^2(f')} \quad (2.6)$$

which were calculated according to Pollak *et al.* [84]. In Figure 2.12 (c), the absolute values $\hat{p}_i(f')$ of the two-dimensional Fourier transformed signals $\hat{\mathbf{p}}_i(f')$ are displayed. The main peak represents the paddle excitation frequency f_e . The higher harmonic frequencies or frequencies of external noise [shown in the inlay in Figure 2.12 (c)] are two orders of magnitude smaller and hence do not influence the waves shape drastically and the wave remains sinusoidal.

The main frequencies in the Fourier space $\hat{p}_i(f')$ were fitted with a Gaussian fit and the amplitudes of the Gaussian fit B_i were read out. Since the amplitudes B_i are directly proportional to the amplitude of the traveling waves a_w it is possible to state whether a wave is convectively unstable or stable against the disturbance by looking at the difference of the two amplitudes of the Gaussian fit $\Delta B = B_2 - B_1$. The flow is convectively unstable against the disturbance if the wave was amplified in streamwise direction ($\Delta B > 0$). If the wave is damped in streamwise direction, the flow was denoted as stable against the free surface disturbance ($\Delta B < 0$). The whole Reynolds number and frequency range considered was scanned with small steps in both directions Re and f_e to find the stable and convectively unstable regimes. Both regimes are separated by the neutral curve where the difference between the amplitudes for the two probing

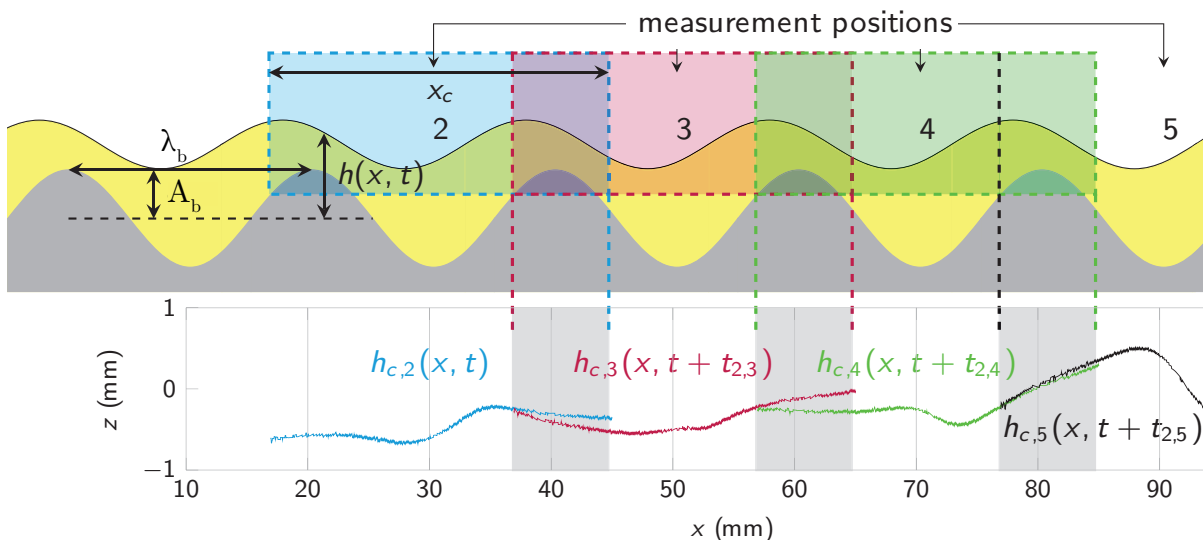


Figure 2.13.: The sketch shows a series of measurements over a sinusoidal substrate. Due to technical limitations, the whole channel could not be measured at one shot. Exemplary measurement positions two through five are shown. The recorded areas show overlaps to the adjacent ones. These were used to erase the mismatches between the fragments of the unsteady waves which are shown in the lower part, and join them together. Modified and reprinted with permission from Reck and Aksel [126]. © AIP Publishing.

positions is equal zero $\Delta B = 0$. This decisive point is only hit by chance in the experiment, hence the neutral point was found by a linear interpolation between neighboring points in either frequency or Reynolds number direction, please see Figure 2.12 (d). The neutral points were determined with a precision of $\Delta f = \pm 0.2 \text{ Hz}$ and $\Delta Re = \pm 0.5$.

2.2.4. Wave dynamics

In order to gain information on the wave dynamics, a measurement setup and technique related to preceding approaches was used [126,140]. The dynamics deal with traveling free surface waves on the steady flow in the linear and nonlinear regime. The measurement setup was already used for the detection of the free surface of the steady flow $h_0(x)$, please see Figure 2.7 with camera 1 and Figure 2.8. The system consists of a linear motor type *E1250-IP-UC/V1RE* from *LinMot*, as described in Sections 2.1.1 and 2.2.3, at least three 70 mW line lasers type *FP-MVmicro-450-70-10-F* by *Laser Components*, as described in Section 2.2.2, a high-speed camera *CR600x2* from *Optronis* (camera 1 in Figure 2.7), as described in Section 2.2.2 and a traversing unit type *iMC-S8* by *isel Germany AG*, as visible in Figure 2.8. The high-speed camera recorded 1200 images of the fluorescence of the silicon oil dye mixture with a frame rate of 200 fps. For the analysis of the free surface shape $h(x, t)$ the same edge-detection algorithm was used as in Section 2.2.2.

Since the free surface waves travel on the surface of the steady flow the detected free surface shape $h(x, t)$ is a superposition of the free surface of the steady flow $h_0(x)$ and the unsteady traveling free surface wave $h_c(x, t)$:

$$h(x, t) = h_0(x) + h_c(x, t). \quad (2.7)$$

The recorded images have the length $x_c \approx 28 \text{ mm}$, as described in Section 2.2.2 in order to have a good spatial resolution. To follow the wave dynamics, it is necessary to capture the wave

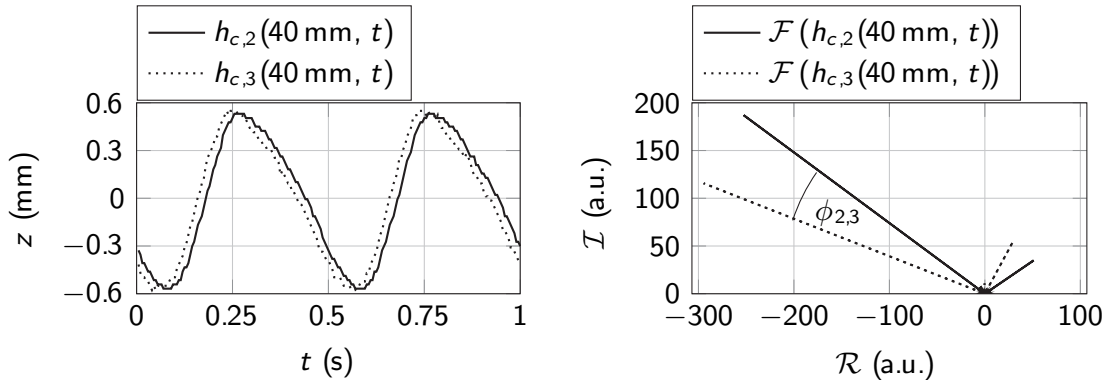


Figure 2.14.: The graph on the left side shows the amplitude-time-curves at the same downstream position $x = 40$ mm for the measurements at positions two and three which have a slight phase difference. The phase difference $\phi_{2,3}$ in radian measure can be read from the graph on the right hand side which displays the imaginary parts of the Fourier Transformations of the two amplitude-time-curves against their real parts. Modified and reprinted with permission from Reck [140].

along the whole channel length. Therefore, the measurement equipment, i.e., the lasers and the high-speed camera, was mounted on a traversing unit which moved alongside the channel and recorded the channel in fragments, which extend over $x = 20$ mm. The difference in the length of the fragments $x = 20$ mm and the length of the recorded images $x_c \approx 28$ mm leads to an overlap between two adjacent fragments, as visible in Figure 2.13.

Having captured all fragments along the channel, the *MatLab* algorithm calculated the free surfaces of the perturbed flow $h_i(x, t)$, which have to be corrected by $h_0(x)$ to yield the continuous wave's shape $h_{c,i}(x, t)$, please see Equation 2.7. These corrected fragments $h_{c,i}(x, t)$, $i = \{1, \dots, N_{frag}\}$ have to be recombined, whereas N_{frag} is the substrate length divided by the length of the fragments ($x = 20$ mm). Please, see exemplarily some fragmented continuous wave's shapes $h_{c,i}(x, t)$ in Figure 2.13. The aforementioned overlap between two adjacent units is also visible in Figure 2.13. In the overlap region the unsteady traveling free surface wave $h_c(x, t)$ clearly shows a discrepancy between two adjacent units. This discrepancy is caused by the random starting times of the measurements, however due to the periodic nature of the waves produced by the paddle, the unsteady waves repeat themselves after each period $1/f_e$. Which means

$$h_{c,2}(x, t) = h_{c,2}\left(x, t + \frac{n}{f_e}\right) \quad (2.8)$$

with n being an integer. The time delay of the measurements between two units is denoted as $t_{i,i+m}$, whereas m is a neutral number symbolizing the distance between two fragments. In the case of two adjacent units, $t_{i,i+1}$ is only by chance equal to $1/f_e$. The mismatch shown in Figure 2.13 can be erased by looking at the amplitude-time-curves as displayed on the left side in Figure 2.14. The visible phase difference $\tau_{i,i+1}$ can be calculated by computing the Fast Fourier Transformation $\mathcal{F}(h_{c,i}(x, t))$ of adjacent units in the overlap region. The phase mismatch in radian measure $\phi_{i,i+1}$ can be found by plotting the imaginary parts \mathcal{I} against the real parts \mathcal{R} . This is exemplarily plotted for the fragments $i = 2$ and $i = 3$ on the right side in Figure 2.14. The phase mismatch in time measure can be calculated by:

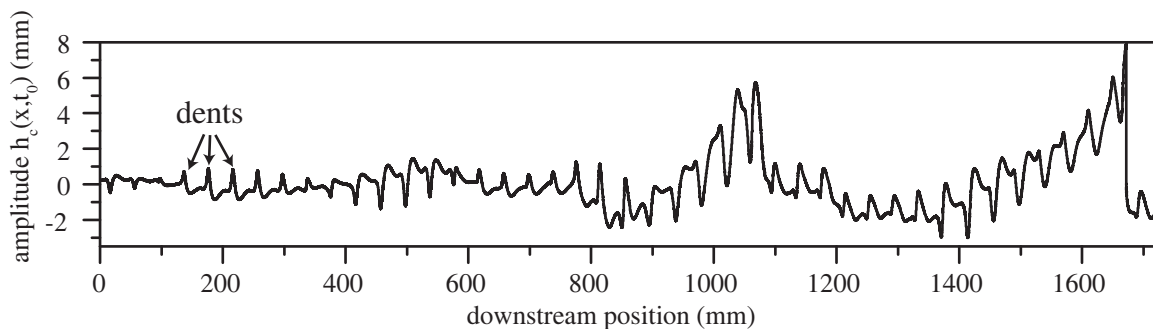


Figure 2.15.: An example of a free surface wave over a rectangular substrate with $W/L = 20/20$ and $f_e = 1.0$ Hz.

$$\tau_{i,i+1} = \frac{\phi_{i,i+1}}{2\pi} \cdot \frac{1}{f_e}. \quad (2.9)$$

The phase mismatch τ was calculated for all points in the overlap area yielding a higher accuracy after averaging over all these points. For recombining the wave along the whole channel all measurement positions have to be in the same phase, therefore all phase mismatches referring to the starting fragment have been calculated $\tau_{1,i}$ ($i = 2, \dots, N_{frag}$). Then all fragments were recombined by superposition:

$$h_c(x, t) = \sum_{i=1}^{N_{frag}} h_{c,i}(x, t + \tau_{1,i}). \quad (2.10)$$

An exemplary wave is displayed in Figure 2.15. The dents visible in Figure 2.15 for the rectangular shaped substrate result from the data processing: the curved steady state free surface h_0 of the stationary flow, which is induced by the substrate is subtracted from the time-dependent resulting free surface $h(x, t)$. For undulated substrates the top of the trench shows a slightly higher amplitude than the bottom of the trench, yielding these pronounced dents in the wave plots. The distance between these dents represents the wavelength of the substrate's topography. The origin of the dents is exemplarily shown in Figure 2.16, where the continuous wave shape h_c is plotted over an undulation.

2.2.5. Single particle Tracking

The flow pattern at the center of the channel was visualized by single particle tracking experiments (SPT). With this measurement technique the steady state flow and the flow which was perturbed by nonlinear traveling free surface waves were considered. The respective setup is shown schematically in Figure 2.7. An *Optronis CR600x2* high-speed camera (camera 2 in Figure 2.7), a 110 mW laser light sheet created by *FP-L-635* line lasers from *Laser Components* with a central emission wavelength of 635 nm, and nearly neutrally buoyant tracer particles type *80A601* from *Dantec* with a mean diameter of 10 μm , described in Section 2.1.4, were used. The light sheet had a width of about 0.5 mm in y -direction, lay in the x - z -plane, and illuminated the entrained particles there. The camera was aligned parallel to the y -axis and collected the light scattered at the above-mentioned tracers through the transparent side-walls. At each experimental run 5000 images with a resolution of at least 40 $\mu\text{m}/\text{pixel}$ were recorded. The frame rate was set to 900 frames per second.

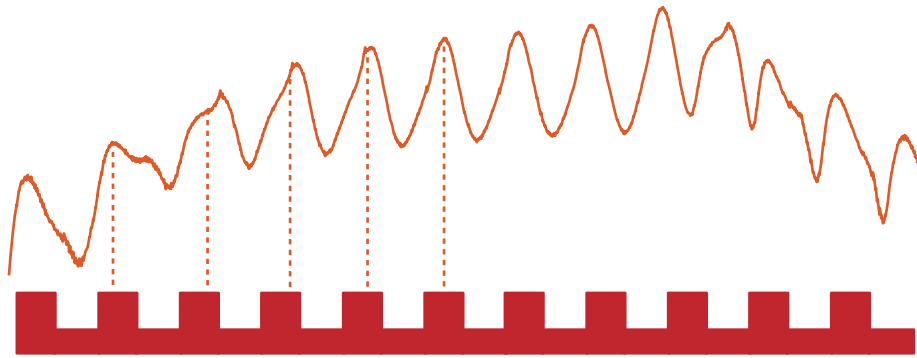


Figure 2.16.: Part of a traveling free surface wave which is already corrected by the steady state free surface with a sketch of the underlying substrate. Modified and reprinted with permission from Dauth and Aksel [143]. © AIP Publishing.

The acquired data was post-processed with an SPT technique based on the widely used Crocker-Grier algorithm [148], implemented and extended according to *Python Trackpy* [149]. In a nutshell, the individual particles were first localized with sub-pixel accuracy in each image and then the particle coordinates of subsequent images were linked to a trajectory. Finally, the spatial calibration in real-world coordinates was achieved with the help of the ceramic calibration plate, shown in Figure 2.9 (b). An example image with tracer particles and their trajectories is shown in Figure 2.17 for the steady state flow over a rectangular topography.

2.2.6. Wave screening

For the observation of the wave front, two different camera positions were used, namely a frontal view and a view from above (bird's eye view). A picture of the measurement setup is displayed in Figure 2.18. Both observation methods were used at two different measurement positions in the channel $x = 94.0$ cm and $x = 170.0$ cm.

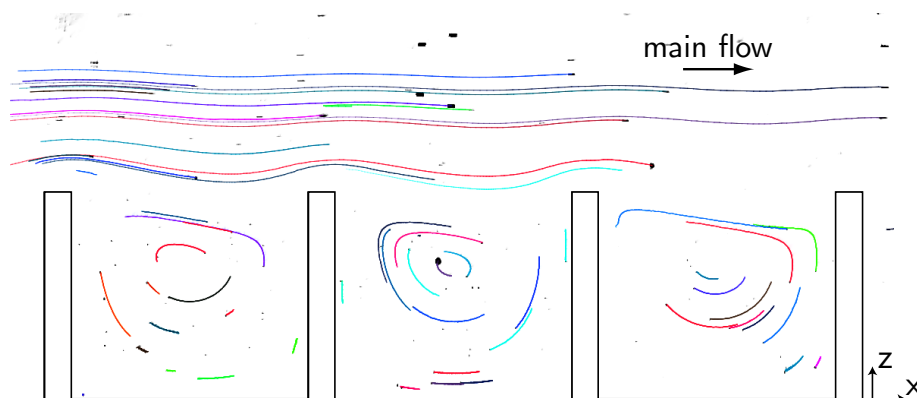


Figure 2.17.: Example image with tracer particles (black dots), overlaid with particle trajectories (colored lines). The contour of the rectangular topography with $A = 8$ mm, $W/L = 1/9$ mm, $\alpha = 10^\circ$ is shown as a black line. Modified and reprinted with permission from Dauth *et al.* [139]. © AIP Publishing.

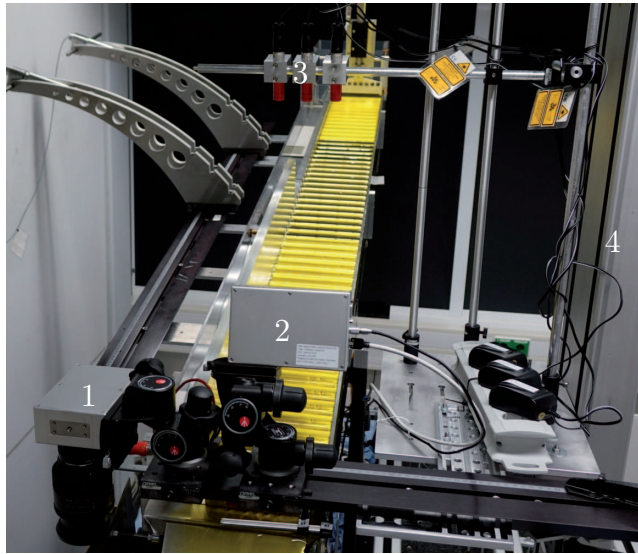


Figure 2.18.: Experimental setup for the wave screening: [1] high-speed camera for the bird's eye view recording, [2] high-speed camera for the frontal view, [3] three 70 mW line lasers to illuminate the oil and [4] traversing unit. This picture shows the configuration for the frontal view. For the bird's eye view, the traversing unit has to be moved above the channel and then recorded with camera [1]. Modified and reprinted with permission from Dauth and Aksel [144]. © AIP Publishing.

Frontal view

In the frontal perspective of the wave front, the oil in a direction perpendicular to the flow direction was illuminated with three 70 mW line lasers ([3] in Figure 2.18). The high-speed camera ([2] in Figure 2.18) captured the profile of the wave front over almost the whole channel width (160 mm) with a time resolution of 500 fps by recording the fluorescence of the oil of the illuminated laser intersection. The incident laser light was blocked by an appropriate filter. This way, a time resolution of the wave at one specific downstream position was achieved.

Bird's eye view

The camera ([1] in Figure 2.18) recorded from a position above the channel. For this sake, the whole measurement equipment on the traversing unit ([4] in Figure 2.18) was moved to a different position (as depicted in Figure 2.18) and recorded the wave from above. White light was used to illuminate the flow.

3. Results and discussion

3.1. Wave shapes in the nonlinear regime on film flows

3.1.1. Motivation

The linear stability of gravity-driven waves was studied extensively over flat and undulated substrates. Leaving the linear regime into the nonlinear regime for flat substrates, the number of publications decreases. For nonlinear waves over undulated substrates the number of publications decreases even further. In the available literature the external forced perturbation on the flows was mainly sinusoidal but changed its shape on the way downstream into a concave shape. There is no work considering the change of the wave's curvature. The wave's shape is decisive for example for heat exchangers, since the amount of transported liquid in the wave strongly depends on the wave's curvature, which influences the efficiency of the heat transport. Therefore, this Section focuses on the influence of the undulated topography on the curvature of the traveling nonlinear free surface waves.

Figure 3.1 shows two examples of the traveling waves over the *Flat* and the *Rec* substrate with $W/L = 1/19$. The two waves show a completely different behavior. In the case of the *Flat* channel the traveling wave exhibits the well-known classical concave shape [124], whereas a convex curvature of the wave for the *Rec* bottom profile is obtained. To ease the determination of the type of curvature, the wave's amplitude, shown in Figure 3.1, is overlaid with a spline function to average over amplitude undulation caused by the dents (as described in Section 2.2.4). Calculating the second derivative of the fit directly yields the curvature type. The difference in the curvature of both traveling waves provokes the question: What makes waves over topographies either concave or convex?

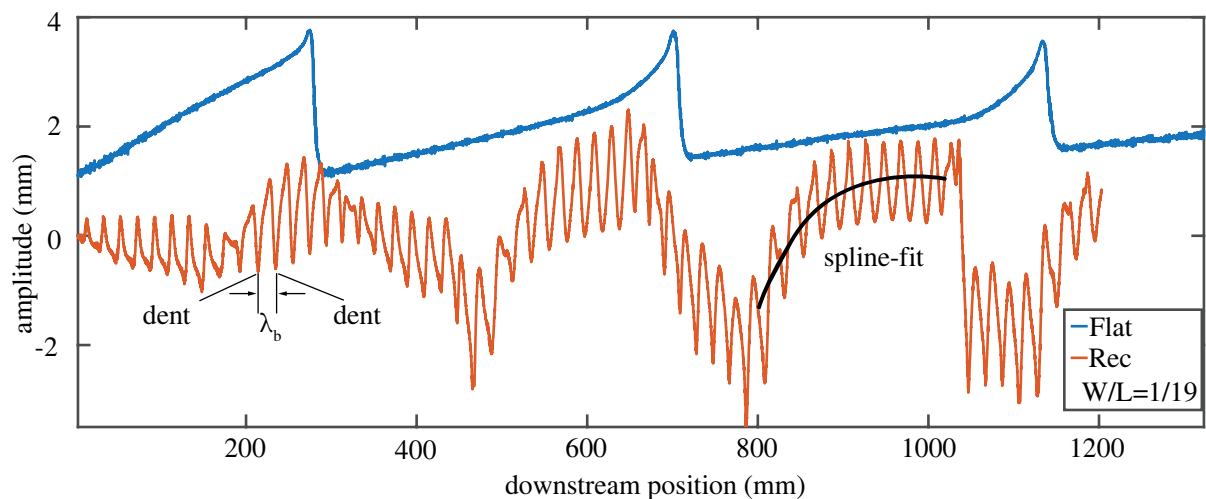


Figure 3.1.: Different curvatures for traveling free surface waves at $f_e = 1.0$ Hz over a *Flat* (blue) and a *Rec* (red) topography with $W/L = 1/19$ (red). For the wave over the flat substrate an offset is added due to lucidity. Modified and reprinted with permission from Dauth *et al.* [139]. © AIP Publishing.

To understand the reasons behind the formation of different wave forms, a series of measurements was carried out. The parameter space of the influencing parameters was classified into two subspaces. On the one hand, there are the wave excitation properties, e.g., the excitation frequency f_e and the amplitude A_e . Both wave characteristics have been varied in the experiments. On the other hand, the properties of the topography were varied. Firstly, the wavelength λ_b of the *Rec* substrate was varied within $\lambda_b = \{0; 10; 20; 100; \infty\}$ mm with a constant length of the top of the trench $W = 1$ mm. The *Flat* substrate can be either treated as a rectangular substrate with infinite or zero wavelength. Secondly, the substrate's amplitude A can be changed. In the experiments $A = 8$ mm was kept constant because already the amplitude to wavelength ratio was changed by varying the wavelength λ_b . Thirdly, the shape of the topography was modified, as shown in Figure 2.3.

This Section 3.1 is based on the publication "What makes the free surface waves over topographies convex or concave? A study with Fourier analysis and particle tracking" by Dauth *et al.* [139].

3.1.2. Measured parameter space

The experiments in this Section have been carried out on all substrate shapes shown in Figure 2.3 (b), namely *Sin*, *Rec*, *Saw* and *Flat*. The substrate's wavelength for the *Sin* and *Saw* topography was kept constant at $\lambda_b = 20$ mm. In the case of the *Rec* substrate the wavelength was varied within $\lambda_b = \{0; 10; 20; 100; \infty\}$ mm with a constant length of the top of the trench $W = 1$ mm.

The linear and nonlinear waves considered in this Section were analyzed by the measurement techniques: linear stability (Section 2.2.3), wave dynamics (Section 2.2.4), and single particle tracking (Section 2.2.5). All measurements were taken at an inclination angle of

$$\alpha = (10.0 \pm 0.1)^\circ, \quad (3.1)$$

a temperature of

$$\theta = (23.0 \pm 0.1)^\circ\text{C}, \quad (3.2)$$

and a volume flux of

$$\dot{V} = (140 \pm 3) \frac{\text{cm}^3}{\text{s}}. \quad (3.3)$$

The corresponding Reynolds number Re , Nusselt film thickness h_n and the free surface velocity for the Nusselt flow $u_{s,n}$ can be calculated by Equations 2.2 and 2.3:

$$Re = 12.0 \pm 0.5, \quad (3.4)$$

$$h_n = (5.3 \pm 0.1) \text{ mm}, \quad (3.5)$$

$$u_{s,n} = (233 \pm 6) \frac{\text{mm}}{\text{s}}. \quad (3.6)$$

3.1.3. Variation of the topography wavelength

In this Section, the substrate wavelength λ_b is varied for the rectangular shaped topography. The waves flowing over the five different substrates with $\lambda_b = \{0; 10; 20; 100; \infty\}$ mm were compared and stated the differences.

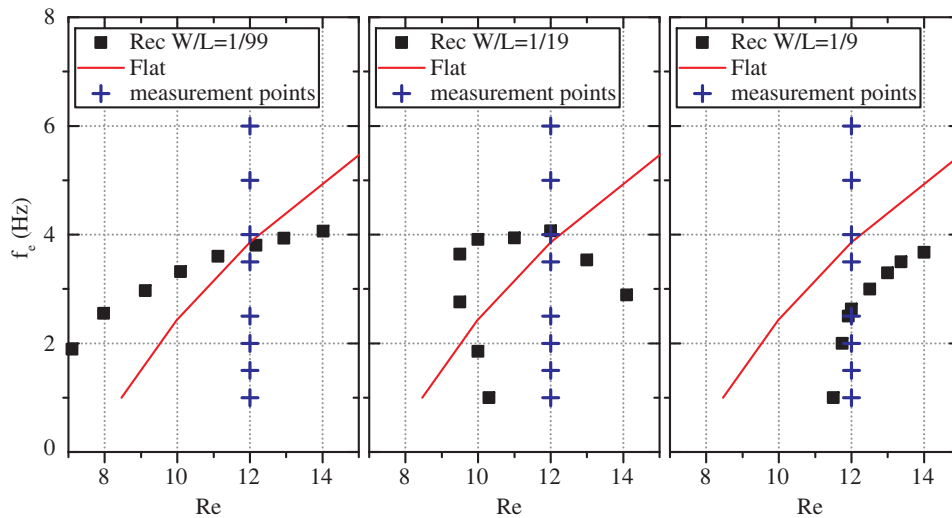


Figure 3.2.: Linear stability maps for the rectangular substrates with $\lambda_b = \{0; 10; 20; 100; \infty\}$ mm with $W = 1$ mm. Red line: measured neutral curve for the flat substrate; black squares: measured neutral points for each substrate; blue crosses: measured frequencies for traveling waves. Modified and reprinted with permission from Dauth *et al.* [139]. © AIP Publishing.

The stability charts obtained for the flows over the rectangular topographies are shown in Figure 3.2. The black dots indicate neutral points for small disturbances of the flows over the undulations. The red line is the measured neutral curve for the flat substrate, which corresponds to $\lambda_b = \{0; \infty\}$ mm. The blue crosses indicate the points $(Re = 12, f_e)$ where the wave evolution was measured.

For the wave evolution measurements the excitation frequency was set to $f_e = 1.0$ Hz for all rectangular substrates, see Figure 3.3 (a). Two different types of wave curvatures can be observed. Firstly, a concave shape for $\lambda_b = \{0; 10; 100; \infty\}$ mm is visible, whereas the flat substrate and $\lambda_b = 10$ mm exhibit the clearest concave shape. Secondly, a convex shape for $\lambda_b = 20$ mm is visible.

For each substrate wavelength the wave shape differs. Hence an interaction between the traveling wave and the topography has a major impact on the propagation of the surface wave. The waves were excited sinusoidal at the inlet. These waves change their shape on the way downstream to non-sinusoidal, see Figure 3.3 (a). Hence, all developed waves are a superposition of waves of various wave numbers, which is investigated in the Fourier space, please see Figure 3.3 (c). For details on the Fourier decomposition see Reck and Aksel [126].

As the time evolution of the traveling wave over the various substrates is of interest those are displayed in Figure 3.3 (b), in line with Trifonov [97] and Reck and Aksel [126]. The traveling waves with the excitation frequency $f_e = 1.0$ Hz are shown for five time steps $t = \{0, T/4, T/2, 3T/4, T\}$. With the time evolution it is possible to calculate the wavelength of the traveling waves with the help of the phase velocity. It is also possible to derive the wavelength from the Fourier-Transformation. Both results are almost identical with a deviation below 0.5%. In line with the FFT plots in Figure 3.3 (c), the values of the wavelength computed by the FFT are shown.

For the flat incline, the excitation wave number k_e and its higher harmonics combine to the concave wave. In contrast to the flat substrate, for $\lambda_b = 20$ mm a completely new feature occurs next to the basic wave number and its higher harmonics. Something similar to beat

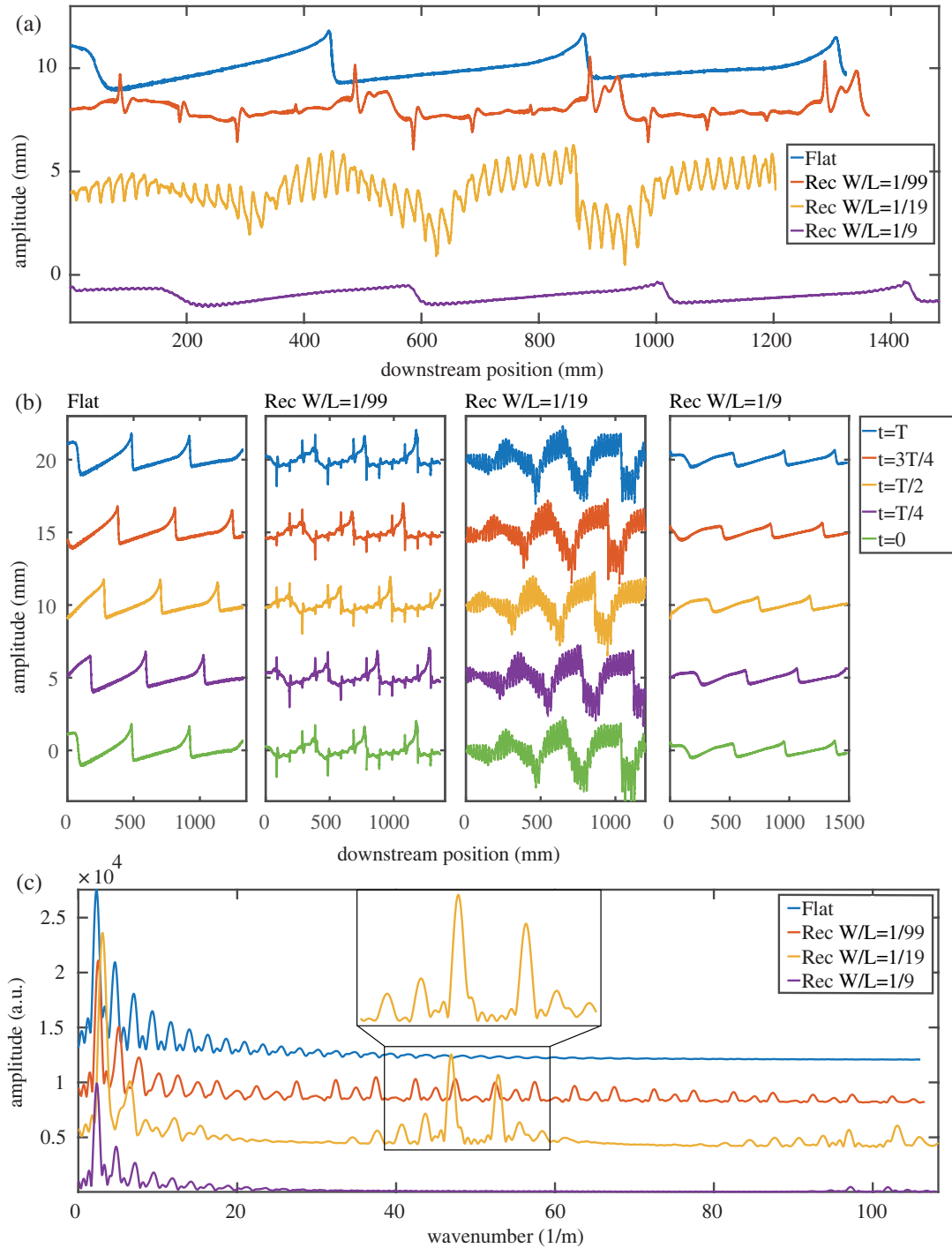


Figure 3.3.: (a) Evolution of waves over different rectangular substrates with $\lambda_b = \{0; 10; 20; 100; \infty\}$ mm with $f_e = 1.0$ Hz. (b) Time evolution of the traveling wave with $f_e = 1$ Hz over one period for the four different substrates in $T/4$ steps. (c) Wave number spectra for $\lambda_b = \{0; 10; 20; 100; \infty\}$ mm with $f_e = 1$ Hz. The inlay shows the beat peaks magnified for the rectangular substrate with $\lambda_b = 20$ mm. An offset is added to some curves in (a), (b) and (c) due to lucidity. Modified and reprinted with permission from Dauth *et al.* [139]. © AIP Publishing.

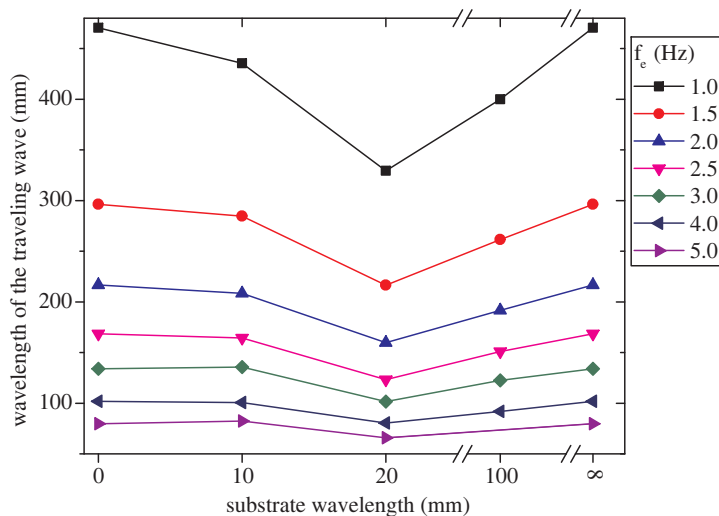


Figure 3.4.: Comparison of the wavelength of the traveling wave with the wavelength of the substrate for various excitation frequencies f_c . Modified and reprinted with permission from Dauth *et al.* [139]. © AIP Publishing.

wave numbers is visible for $\lambda_b = 20$ mm at $k_c = 40 - 60$ m^{-1} . This shows that the interaction between the traveling wave and the substrate's wave has a major impact on the evolving shape of the traveling wave. The two major peaks in Figure 3.3 (c) for the yellow curve around $k_c = 50$ m^{-1} are calculable with $k_{1/2} = k_0 \pm k_s$, where k_0 is the wave number corresponding to the substrate undulation and k_s is the wave number for the basic excitation and its higher harmonics [126]. The substrate wavelength $\lambda_b = 20$ mm leads to $k_0 = 50$ m^{-1} . This criteria is fulfilled for the major peaks around $k = 50$ m^{-1} . It can also be observed for the substrate wavelengths $\lambda_b = \{10; 100\}$ mm. For $\lambda_b = 10$ mm the beat wave number is around $k = 100$ m^{-1} . Yet the amplitude of the beat wave numbers is small which indicates only a weak interaction. With $\lambda_b = 100$ mm the wave numbers k_0 and k_s are in the same region and it is hard to distinguish between a beat wave number and a higher harmonic of the basic wave number of the traveling wave. However, there is an interaction between the traveling wave and the standing surface wave caused by the periodicity of the substrate. The major difference between the substrates is the strength of this interaction. For $\lambda_b = 20$ mm the strongest interaction is visible and for the other topographies only a weak interaction is at hand.

Figure 3.4 shows the wavelength of the traveling free surface wave versus the substrate's wavelength for various excitation frequencies. Starting from the flat substrate, represented by $\lambda_b = \infty$ mm, the wavelength of the traveling wave decreases until it reaches a minimum at $\lambda_b = 20$ mm. Then it increases again for $\lambda_b = 10$ mm to a similar wavelength as the wavelength of the flat topography, which can also be represented by $\lambda_b = 0$ mm. Concerning the wavelength of the traveling wave it can be stated that very long and very short substrate wavelengths show similarities with the flat substrate because the flat topography is the limiting case for the short and the long wavelength of the substrate ($\lambda_b = \{0; \infty\}$). All measured topographies have a shorter substrate wavelength compared to the wavelength of the traveling wave for small excitation frequencies. For all excitation frequencies the same trend is observable. In the next Section the frequency dependence of the traveling wave will be analyzed in more detail.

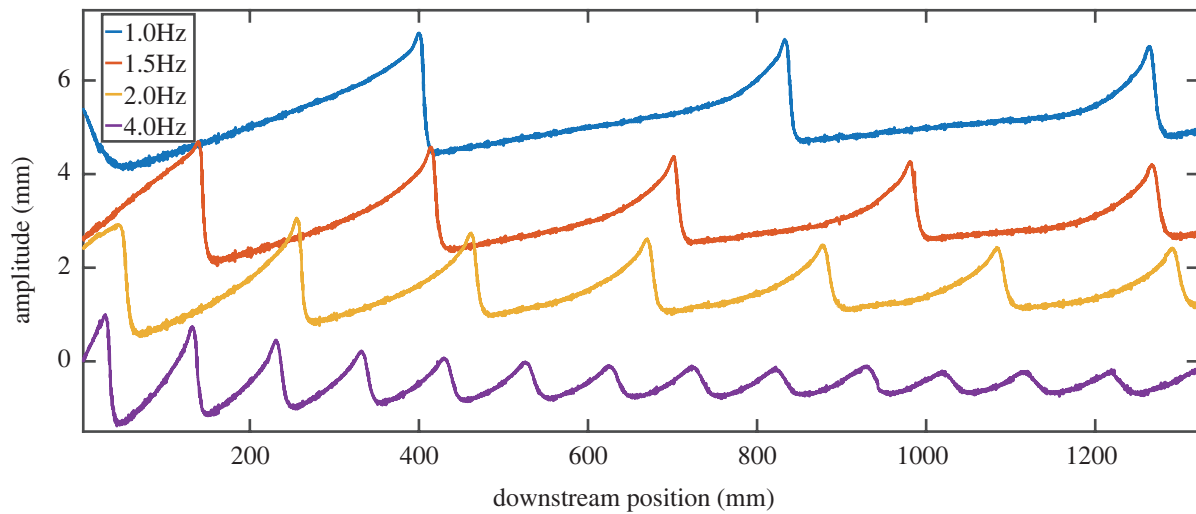


Figure 3.5.: Evolution of traveling waves over the flat substrate for different excitation frequencies f_e . An offset is added to some curves due to lucidity. Modified and reprinted with permission from Dauth *et al.* [139]. © AIP Publishing.

3.1.4. Variation of the properties of the surface wave

Evolution of traveling waves with different excitation frequencies

Figure 3.5 shows traveling waves over the flat substrate for various frequencies. All curves show a decrease in the wave's amplitude even though the excitation frequencies $f_e = \{1.0; 1.5; 2.0\}$ Hz are in the unstable region for $Re = 12$. The amplitude lessens because the saturation amplitude is smaller than the excitation amplitude. All curves in the unstable region exhibit a concave wave shape for the flat substrate.

For the rectangular shaped topography with $\lambda_b = 20$ mm the curves are displayed in Figure 3.6. The waves with the excitation frequencies $f_e = \{1.0; 1.5; 2.0\}$ Hz show a convex shape. This leads to the conclusion that the excitation frequency does not influence the wave's shape. For the other substrates these measurements were also performed and indicate the same conclusion.

Evolution of traveling waves with different excitation amplitudes

The other possibility to probe the influence of the excitation properties is to change the paddle amplitude A_e . It was set to three different magnitudes, $A_e = \{0.5; 2.0; 8.0\}$ mm, these excitation amplitudes provide waves in the linear ($A_e = 0.5$ mm), nonlinear ($A_e = 8.0$ mm) and intermediate ($A_e = 2.0$ mm) region. For $A_e = 0.5$ mm the ratio of the perturbation's amplitude a_w to its wavelength λ_w is smaller than 0.01, hence the waves are linear (see Section 2.2.3). For $A_e = 8.0$ mm the ratio at the beginning of the channel is already larger than 0.01 hence nonlinear waves are present. For all A_e the waves over undulated substrates grow downstream if the disturbances are convectively unstable. The major difference between the measurements is the measurement distance until the waves reach their saturation amplitude and shape. Hence, the excitation amplitude does not influence the wave's saturation shape and the results of these measurements are not shown in this Section.

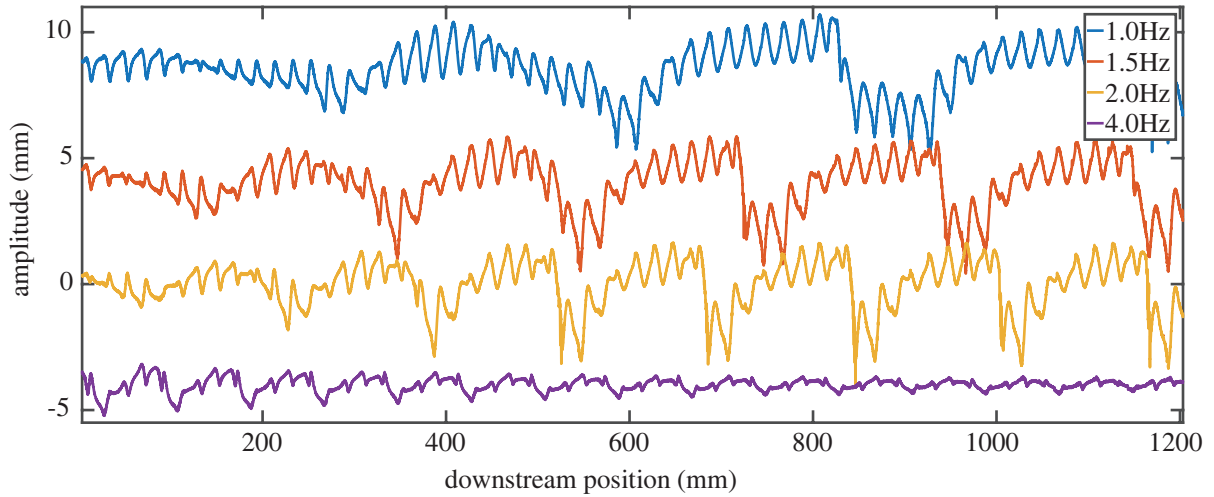


Figure 3.6.: Evolution of traveling waves over the rectangular substrate with $\lambda_b = 20$ mm for various excitation frequencies f_e . An offset is added to some curves due to lucidity. Modified and reprinted with permission from Dauth *et al.* [139]. © AIP Publishing.

3.1.5. Variation of the topography shape

In contrast to Section 3.1.3, the topography's shape is varied and its waviness was kept constant at $A/\lambda_b = 4/20$. The waves over the different undulated geometries and the flat substrate are compared.

The linear stability charts for the three undulated substrates of different shape are shown in Figure 3.7. The graphs have the same appearance as the stability charts in Figure 3.2, explained in Section 3.1.3. For all geometries an unstable isle was found around $Re = 12$.

In Figure 3.8 (a), the wave plots are displayed. The three undulated substrates show a convex

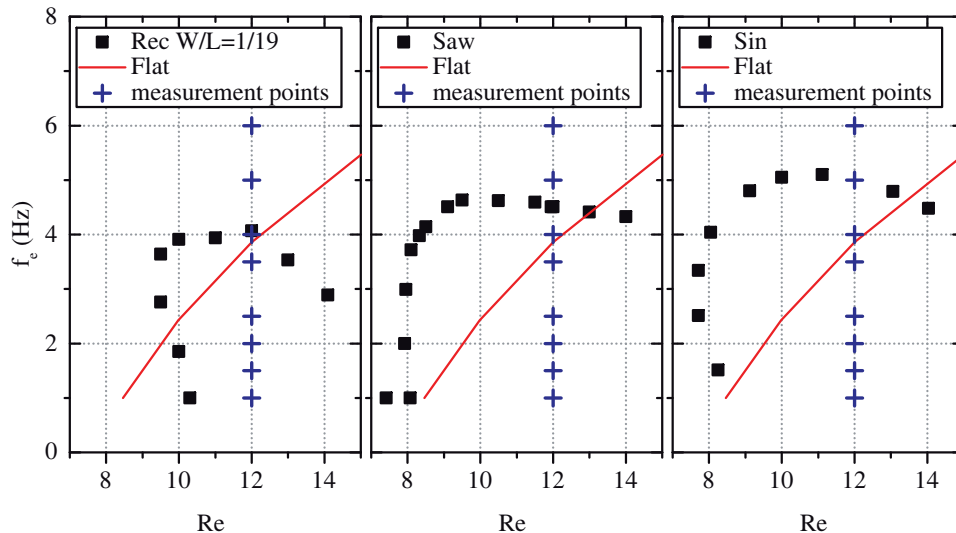


Figure 3.7.: Linear stability maps for the sinusoidal, sawtooth and rectangular substrates with $\lambda_b = 20$ mm. Red line: measured neutral curve for flat substrate; black squares: measured neutral points for each corrugated substrate; blue crosses: measured frequencies for traveling waves. Modified and reprinted with permission from Dauth *et al.* [139]. © AIP Publishing.

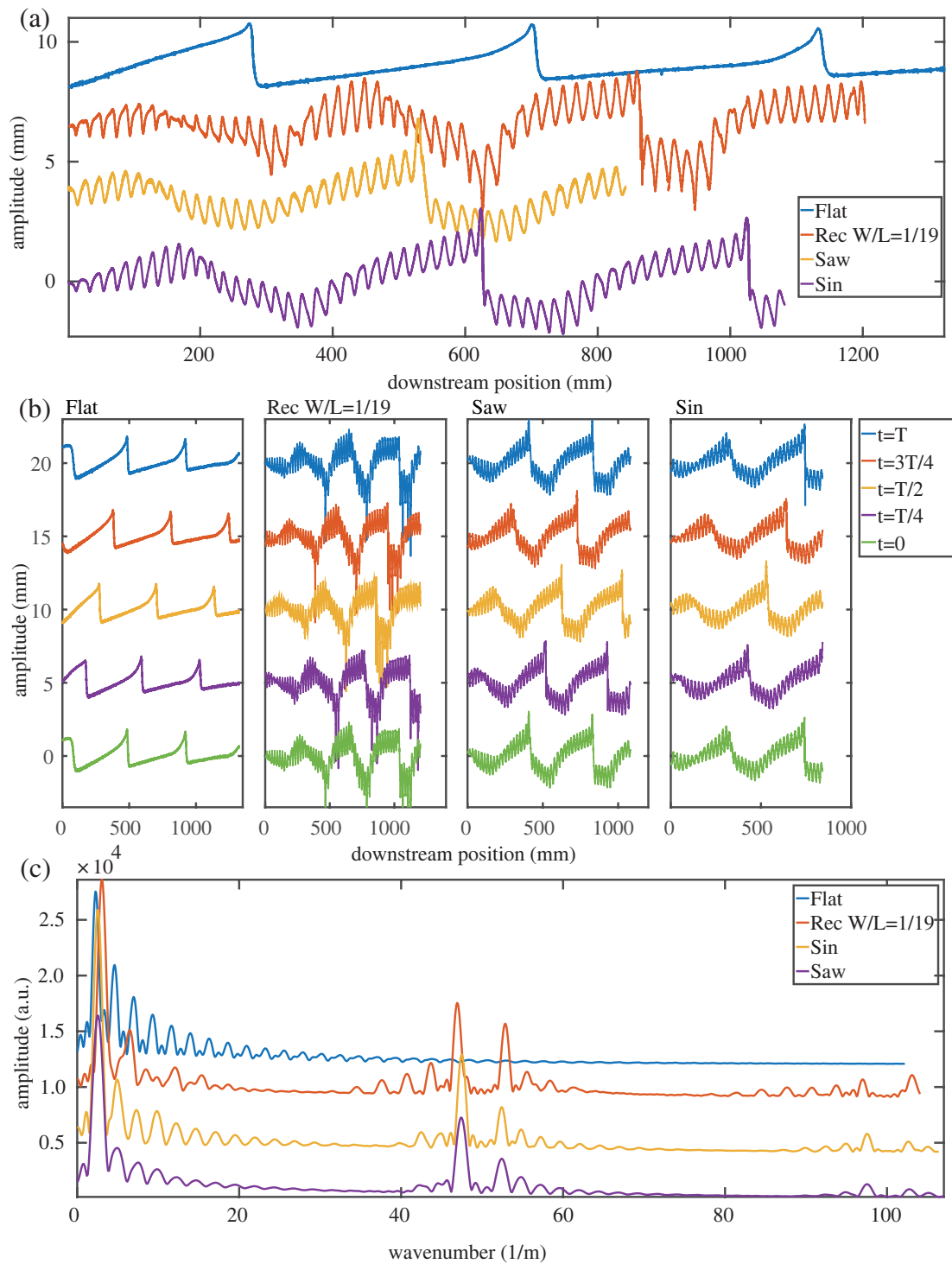


Figure 3.8.: (a) Evolution of traveling waves over various substrate shapes with the excitation frequencies $f_e = 1$ Hz. (b) Time evolution of the traveling wave with $f_e = 1$ Hz over one period for the four different substrates in $T/4$ steps. (c) Wave number spectra for four different substrate shapes with $f_e = 1.0$ Hz. An offset is added to some curves in (a), (b) and (c) due to lucidity. Modified and reprinted with permission from Dauth *et al.* [139]. © AIP Publishing.

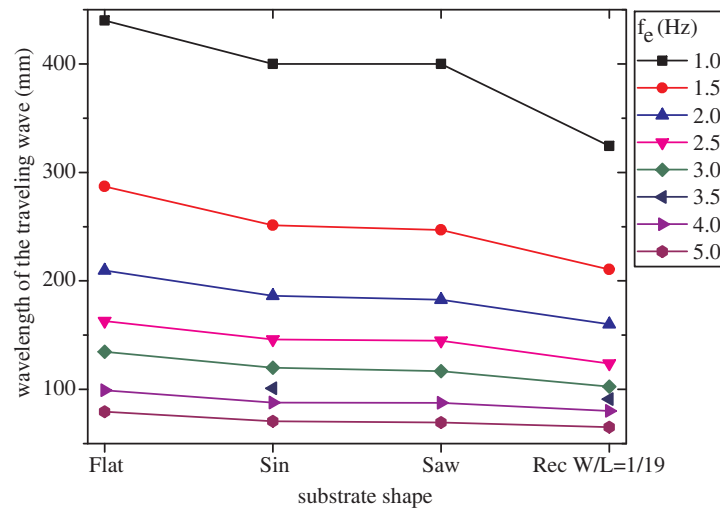


Figure 3.9.: Comparison of how the wavelength of the traveling wave changes with the shape of the substrate for different excitation frequencies f_e . Modified and reprinted with permission from Dauth *et al.* [139]. © AIP Publishing.

wave shape. Yet, there is a difference in the order of convexity. The rectangular substrate (*Rec*) exhibits a more convex wave shape than sine (*Sin*) and sawtooth (*Saw*), which both show a similar characteristic behavior. Since the amplitude to wavelength ratio $A/\lambda_b = 8/20$ was kept constant, the undulation's specific shape also plays a role for the evolution of a large traveling wave.

In Figure 3.9, the wavelength of the traveling wave for various substrates and different excitation frequencies is examined. The waves over the sinusoidally and sawtooth-like shaped topographies exhibit a similar wavelength for all excitations, yet shorter than the wavelength of the wave over the flat substrate. The wavelength λ_w is in between the wavelengths of the flat and rectangular substrates. A similar behavior was seen for the curvature of the wave, see Figure 3.8 (a). This indicates that the interaction between the traveling wave and the underlying flow field plays a major role in the evolution of the large traveling waves.

In order to test this hypothesis, the Fourier space was investigated in Figure 3.8 (c). The results for the flat (*Flat*) and the rectangular (*Rec*) substrate are already known from Section 3.1.3. For the sinusoidal (*Sin*) and sawtooth-like (*Saw*) profile beat wave numbers are also found. The beat amplitudes of the excitation and its harmonics are slightly weaker than the ones for the rectangular topography. In this context the greatest interaction between the substrate and the traveling wave for the rectangular substrate is visible and no interaction for the flat substrate. The interaction strengths for the sinusoidal and sawtooth-like substrate are settled in between. For all corrugations the interaction between the substrate and the traveling wave effects the curvature of the traveling wave and its wavelength.

3.1.6. Study of dimensionless parameters

In this Section, the relations between the amplitudes and wavelengths of the traveling waves and the substrates are compared. In Figure 3.10 (a), the wavelength of the traveling wave compared to the substrate's wavelength is plotted over the excitation frequency for the sinusoidal, the sawtooth-like and the rectangular substrates. The rectangular substrate with $\lambda_b = 20$ mm, the sinusoidal, and the sawtooth-like substrates have the same substrate wavelength and show a narrow band in the Figure 3.10 (a). The wavelength of the traveling waves can also be seen in

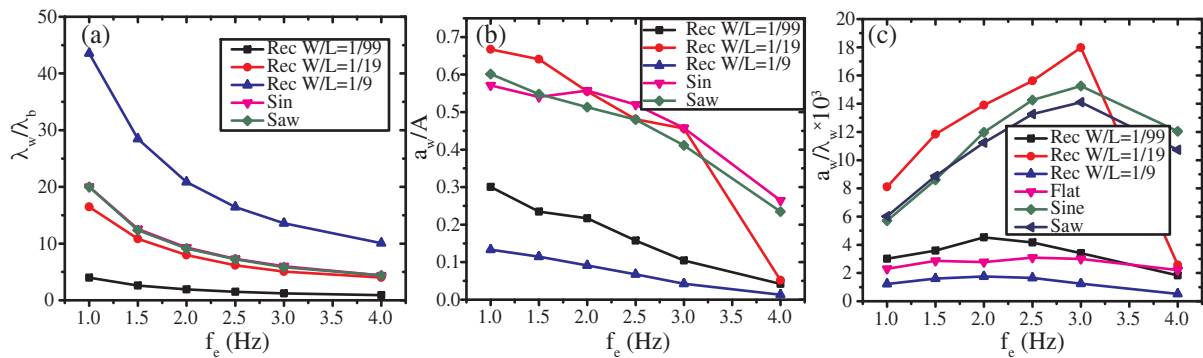


Figure 3.10.: (a) Ratio of the wavelength λ_w of the traveling wave and the wavelength λ_b of the substrate for different excitation frequencies and substrates. (b) Amplitude ratio of the traveling wave and the substrate for various frequencies and different substrates. (c) Amplitude to wavelength ratio of the traveling wave for various frequencies and different substrates. Modified and reprinted with permission from Dauth *et al.* [139]. © AIP Publishing.

Figure 3.4 and 3.9 in a different context. Substrates with the same wavelength lead to a similar wavelength of the evolving wave.

Figure 3.10 (b) shows the amplitude ratio of the traveling wave and the substrate. All substrate amplitudes are $A = 8$ mm hence the amplitudes of the traveling waves can easily be compared. The sinusoidal, sawtooth, and rectangular ($\lambda_b = 20$ mm) substrates show a narrow band for the frequencies $f_e = [1.0; 3.0]$ Hz. For $f_e = 4.0$ Hz the amplitude of the wave over the rectangular substrate leaves this band because of the different stability behavior, see Figure 3.7. The maximum amplitudes of the surface waves a_w for the other two rectangular substrates differ strongly from the band.

Figure 3.10 (c) shows the amplitude to wavelength ratio of the traveling wave for different excitation frequencies and substrate shapes. In the unstable region the ratio is bigger the more the substrate deviates from the flat substrate with respect to waviness and wavelength, see Figures 3.4 and 3.9. The rectangular substrate with $\lambda_b = 20$ mm shows the biggest deviation from the flat substrate for the curvature and wavelength of the traveling wave, see Figures 3.3 (a), 3.4, and 3.9.

3.1.7. Particle tracking

This Section is devoted to the question why variations on the topography's wavelength (Section 3.1.3) and shape (Section 3.1.5) affect the large and strongly nonlinear traveling free surface waves considered in this work. In contrast to these waves, which can show a concave or a convex shape dependent on the topography, the shape of small linear waves was found to remain unaffected [63,99]. In Section 3.1.3 and 3.1.5, it was assumed that a strong interaction between the traveling wave and the underlying fluid plays a major factor for the developing wave shape. In this Section, this assumption will be fortified by single particle tracking measurements. A significant interaction between the traveling wave and the underlying fluid will be shown, furthermore a different penetration depth dependent on the substrate will be shown.

Figure 3.11 shows how the free surface varied over time at a fixed position in streamwise direction when a saturated wave ($A_e = 8$ mm, $f_e = 1.0$ Hz) passed. Figures 3.11 (a) - (c) correspond to the rectangular substrate with $\lambda_b = 10$ mm, Figures 3.11 (d) - (f) to the rectangular substrate with $\lambda_b = 20$ mm and Figures 3.11 (g) - (i) to the sinusoidal substrate. One period of the traveling wave corresponds to 200 time steps. The time is color coded. The respective

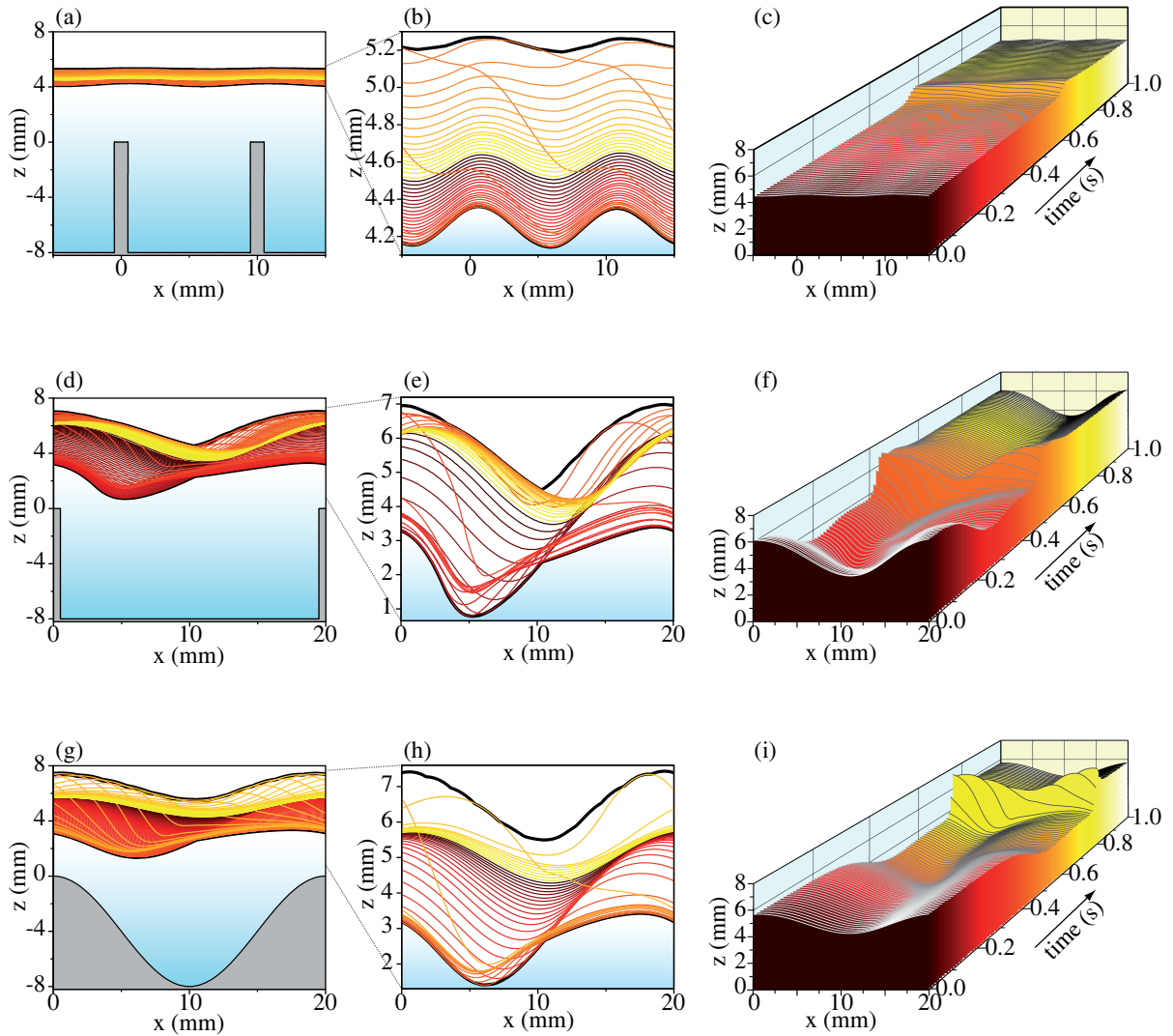


Figure 3.11.: Variation of the free surface during one period of the traveling wave ($A_e = 8$ mm, $f_e = 1.0$ Hz). (a) - (c): rectangular substrate with $\lambda_b = 10$ mm. (d) - (f): rectangular substrate with $\lambda_b = 20$ mm. (g) - (i): sinusoidal substrate. (a), (d) and (g): The free surfaces are plotted for one recorded second with 200 fps. This leads to a band which represents the maximum and minimum local height of the free surface. (b), (e) and (h): show the free surface enlarged for every fifth time step. (c), (f) and (i) show the evolution of the free surface for the same excerpt over time for each second time step. (f) and (i) show the depletion region in front of the wave crest. The contour of the free surface for $t = 0, T/4, T/2, 3T/4$ can be seen in Figure 3.12. Modified and reprinted with permission from Dauth *et al.* [139]. © AIP Publishing.

waves were shown, e.g., in Figure 3.3 (a) and Figure 3.8 (a). The bold black contour lines in the Figures 3.11 (a), (b), (d), (e), (g) and (h) highlight the local maximal and the local minimal height of the free surface during one period of the traveling wave. The width and the shape of the resulting band indicates how large the traveling wave was compared to the whole film and how uniform the local film thickness changed within one period of the corrugation while the wave passed. The raw data for the analysis is given in the supplementary material in publication [139] in form of videos.

The rectangular substrate with $\lambda_b = 10$ mm shows a narrow and flat band, hence the penetration depth of the disturbance, which is the traveling wave, is small. For the rectangular substrate

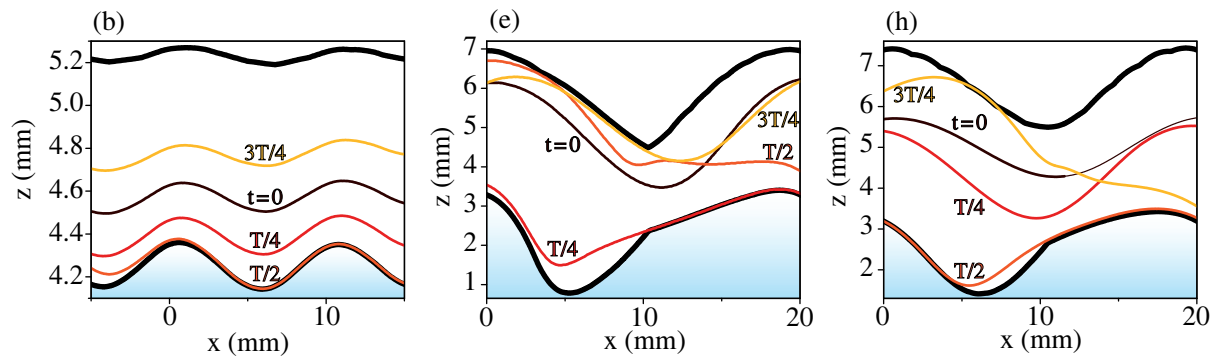


Figure 3.12.: Replotted figures of Figures 3.11 (b), (e), (h). For more optical clarity only time steps $t = 0, T/4, T/2, 3T/4$ are shown. Modified and reprinted with permission from Dauth *et al.* [139]. © AIP Publishing.

with $\lambda_b = 20$ mm the free surface is heavily disturbed by the traveling wave. A similarly strong disturbance is visible for the sinusoidal substrate. For more optical clarity Figures 3.11 (b), (e), and (h) are shown with only four time steps in Figure 3.12.

Moreover, for the two substrates with $\lambda_b = 20$ mm, a depletion region in front of the wave is visible [126]. The rectangular substrate with $\lambda_b = 10$ mm doesn't show a depletion region.

Now, the aforementioned interaction between the traveling surface wave and the underlying flow field has to be proven. For this sake, single particle tracking was used and compared the path lines of tracer particles for the steady state flow and the strongly perturbed flow ($A_e = 8$ mm, $f_e = 1$ Hz). The experiments were performed for the three different substrates shown in Figure 3.11, the sinusoidal one with $\lambda_b = 20$ mm and the two rectangular ones with $\lambda_b = \{10; 20\}$ mm.

Figure 3.13 shows the path lines for the rectangular topography with $\lambda_b = 10$ mm. Both the steady state flow [Figure 3.13 (a)] and the perturbed flow [Figure 3.13 (b)] are shown. Hardly any interaction of the traveling wave with the stationary flow is visible. The rectangular substrate with $\lambda_b = 20$ mm showed strong interaction, which can be seen in Figure 3.14. The steady state eddy, shown in Figure 3.14 (a) breaks up when the traveling wave passed and mixed with the fluid of the wave. Hence, the disturbance is not restricted to the free surface, as it is the case for small linear waves. The penetration depth is large and the whole film flow is heavily disturbed by the wave traveling over the substrate. For the sinusoidal substrate the interaction strength between the large traveling surface wave and the underlying flow field lies qualitatively between the one of the two rectangular topographies (see Figure 3.15).

3.1.8. Conclusions

In this Section (3.1), gravity-driven traveling free surface waves over undulated substrates were considered. Therefore, the flow was perturbed with different excitation frequencies and amplitudes. Furthermore, the substrate was changed in two ways. Firstly, the amplitude to wavelength ratio for a rectangular substrate was varied by elongating or shortening the substrate's wavelength. Secondly, different substrate shapes were used, namely, rectangular, sinusoidal, flat and sawtooth-like.

Two different kinds of wave shapes are reported, i.e., a convex and a concave wave curvature. For a fixed substrate the variation of the excitation frequency does not affect the curvature shape of the traveling wave. The same is valid for the excitation amplitudes.

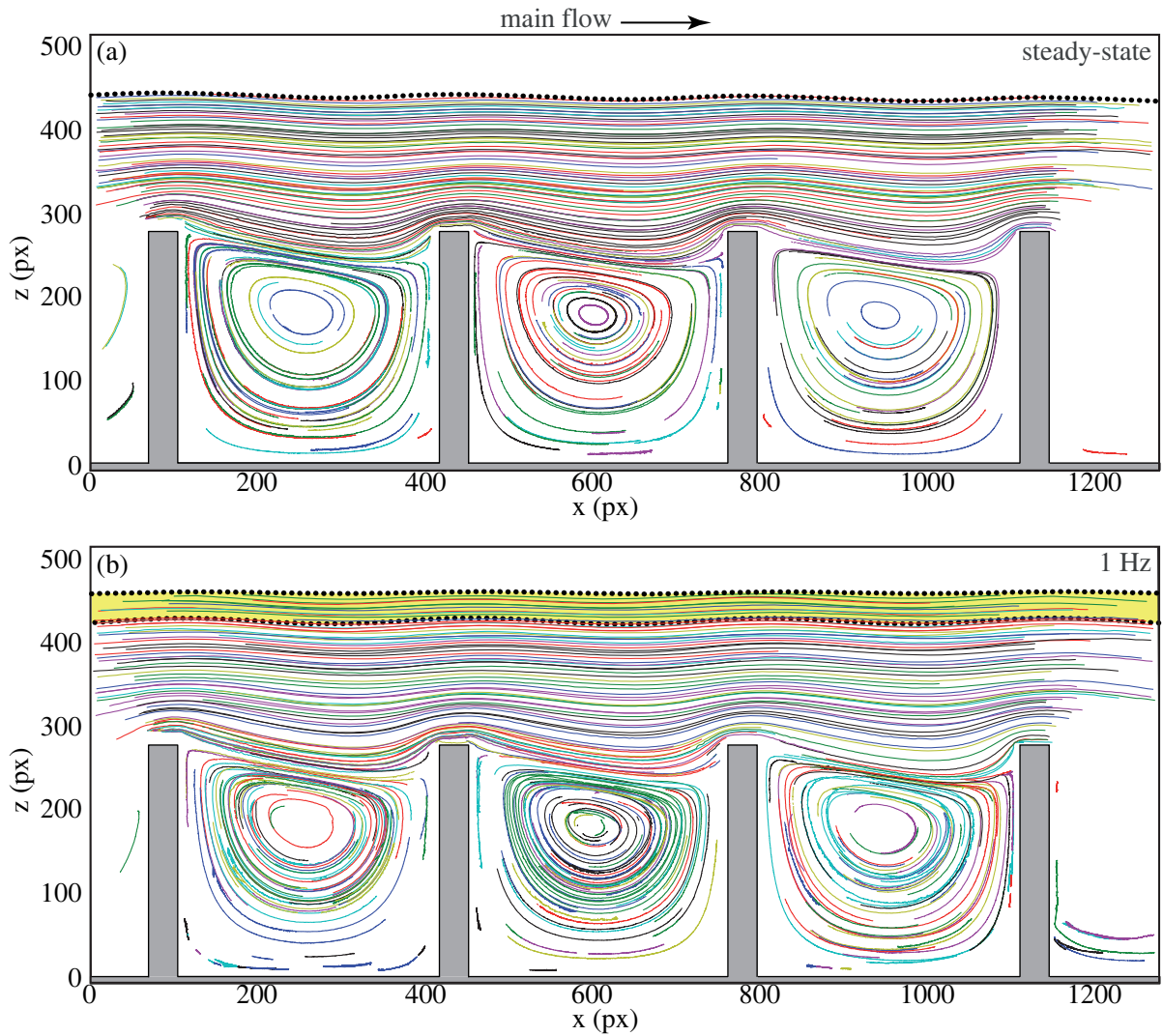


Figure 3.13.: Particle tracking images for the flow over the rectangular substrate with $\lambda_b = 10$ mm. (a) Steady state flow, (b) perturbed flow ($A_e = 8$ mm, $f_e = 1$ Hz). Modified and reprinted with permission from Dauth *et al.* [139]. © AIP Publishing.

For all undulated substrates an interaction of the traveling free surface wave with the substrate's wave is found, which is clearly visible in the Fourier space [Figures 3.3 (c) and 3.8 (c)]. The interaction strength differs strongly for different substrates. Substrates with the same topography wavelength show a similar interaction strength [Figure 3.8 (c)], a similar curvature of the traveling wave (convex) [Figure 3.8 (a)], and a similar wavelength of the traveling wave (Figure 3.9) even though the substrate shapes differ. The substrates with very long or very short wavelengths exhibit a steady state flow near the free surface similar to the flow over a flat substrate [Figure 3.13 (a)]. In these two cases the waves exhibit a weak interaction strength [Figure 3.3 (c)] and the curvature resembles to that of the flat substrate [Figure 3.3 (a)]. Concluding, the phenomena occurring over the flat substrate can be reached by these two limiting cases ($\lambda_b \rightarrow \{0; \infty\}$). Beyond the shape, also the wavelength and amplitude of the traveling wave prove this educated guess [Figures 3.4 and 3.10 (c)].

The particle tracking measurements unveiled the interaction mechanism more clearly. The

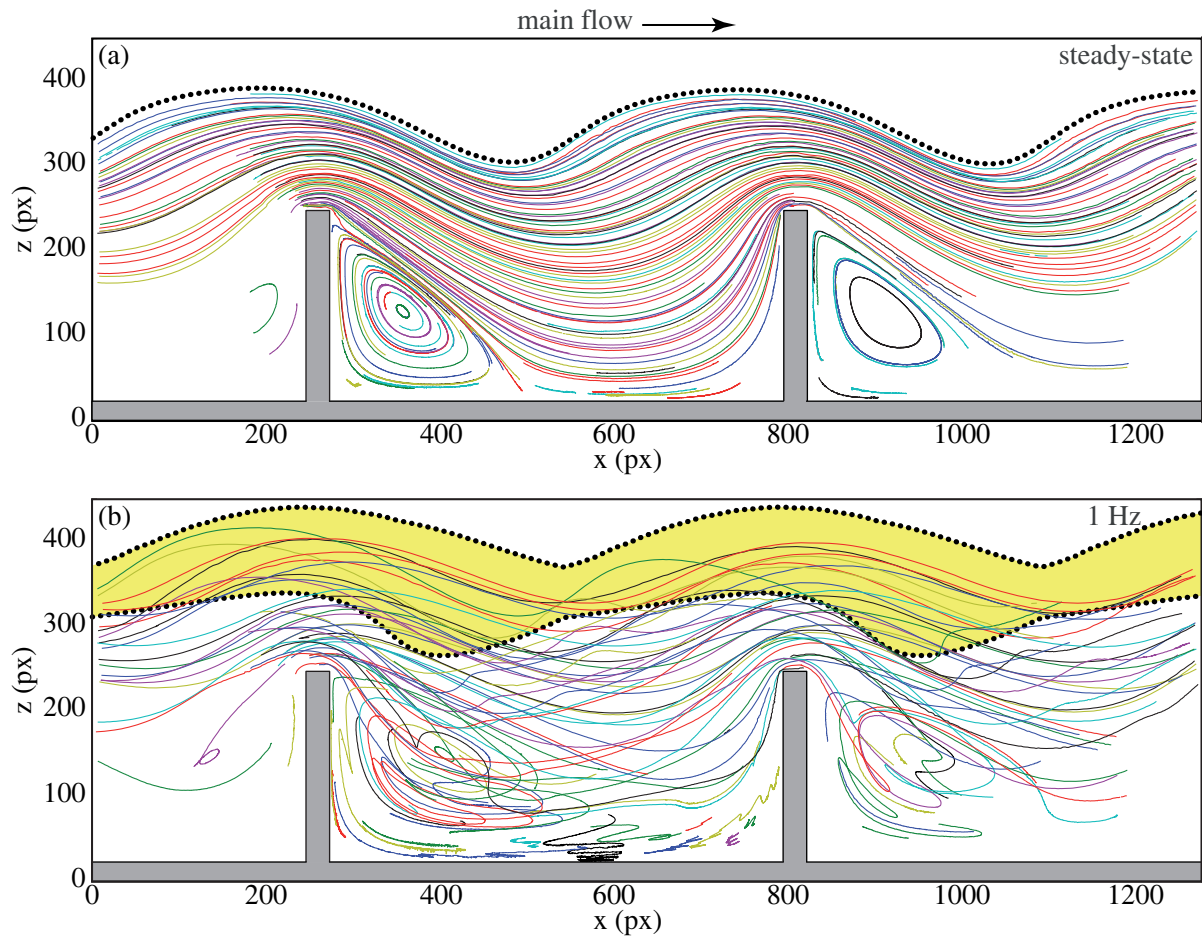


Figure 3.14.: Particle tracking images for the flow over the rectangular substrate with $\lambda_b = 20$ mm. (a) Steady state flow, (b) perturbed flow ($A_e = 8$ mm, $f_e = 1$ Hz). Modified and reprinted with permission from Dauth *et al.* [139]. © AIP Publishing.

rectangular limiting case shows almost no interaction of the traveling wave with the underlying flow [Figure 3.13 (b)]. This weak interaction leads to a concave traveling wave shape similar to the flat substrate when this type of interaction is not present. On the other hand, a strong interaction for some substrates [Figures 3.14 (b) and 3.15 (b)] is clearly visible. Even an eddy break up may be visible [Figure 3.14 (b)]. For strong interactions a convex curvature of the traveling waves is always at hand.

It can be conjectured that the free surface shape of the corresponding steady state flow dictates the interaction strength. Particle mixing provokes a drag force by flinging particles from the underlying steady state flow in the traveling wave [Figures 3.14 (b) and 3.15 (b)]. These particles fill the formerly concave wave and result in a convex shape.

Schörner *et al.* [63] performed a gedankenexperiment which concludes that the steady state free surface is decisive to the linear stability behavior. In this Section 3.1, it is stated that the evolution of linear and nonlinear traveling waves is dictated by the steady state free surface. This explains the similarity of the traveling waves over the sinusoidal, sawtooth-like and rectangular substrates because they exhibit a similar steady state free surface due to eddy formation in the troughs. With this assumption an inverse optimization problem may be triggered: Which substrate exhibits the most wavy steady state free surface and hence results in the most convex

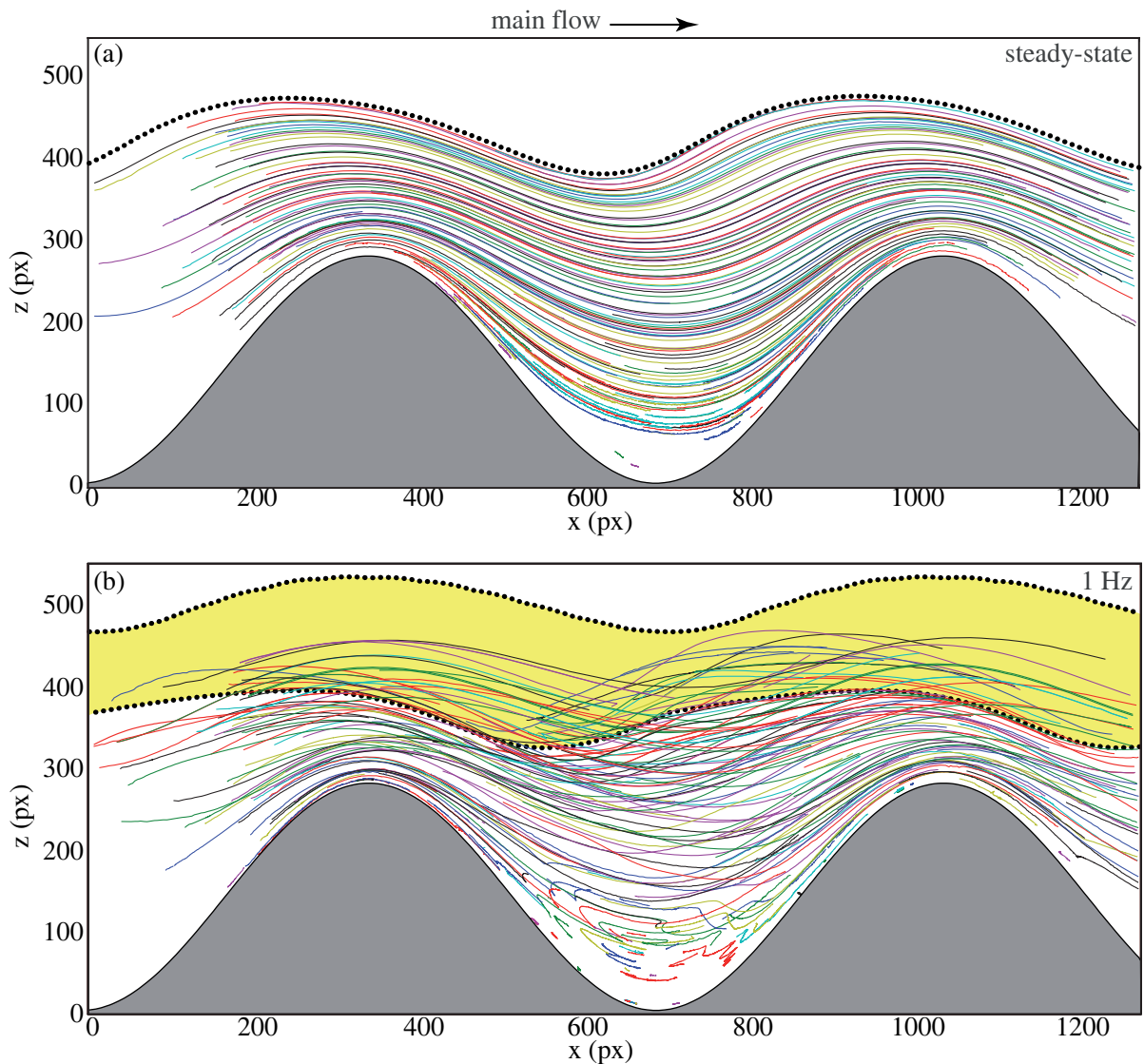


Figure 3.15.: Particle tracking images for the flow over the sinusoidal substrate with $\lambda_b = 20$ mm. (a) Steady state flow, (b) perturbed flow ($A_e = 8$ mm, $f_e = 1$ Hz). Modified and reprinted with permission from Dauth *et al.* [139]. © AIP Publishing.

shape of the traveling wave?

Another gedankenexperiment can be performed which sees the inertia (Reynolds number or volume flux) as a major influence. Based on the increase of the film thickness by increasing the volume flux the steady state free surface smoothens. For very high Reynolds numbers the steady state free surface of a flow over undulated substrates converges against the steady state free surface of a flow over a flat substrate and hence the waves should change their curvature to a concave shape. In the following Section 3.2, the influence of the increase of inertia is observed. Yet, the focus is changed to a new topic since novel phenomena were observed.

3.2. Wave breaking of nonlinear waves on film flows

3.2.1. Motivation

This Section is dedicated to the novel finding of wave breaking in gravity-driven viscous film flows over topographies. Although, wave breaking is well-known in the field of hydrodynamics and visible, e.g., at the beach, the conditions leading to the wave breaking of oceanic waves are not present in our system [150, 151]. While breaking of oceanic waves is well-known textbook knowledge, this is not the case for the wave breaking of gravity-driven free surface waves in a highly viscous channel flow.

Here, we consider the closest analogon to the channel flow, which are *shallow water waves*. Shallow water means that the height of the water is small compared to the wavelength of the wave. This is also the case for the channel flow discussed here. For this kind of flow a theory for wave evolution and breaking exists, see Stoker [151]. This theory is mathematically analogous to the shock in a compressible flow of a gas, where the *viscosity* is neglected ($u_{tt} - c_0^2 u_{xx} = 0$) [151]. In the present oil flow the viscosity is about two magnitudes larger than the viscosity of water and hence not negligible. Furthermore, the bottom at the beach is inclined with a positive slope with respect to the wave vector/wave's direction of motion. Hence, the water waves break into an inclination. In contrast to the water wave inclination, in the considered measurement system the slope declines. Also, the driving forces of the waves are completely different. Gravity is the driving force for the system investigated here. Water waves are shear driven. Beyond this, the basic state for the channel is the undulated steady state free surface. In case of water waves the basic state is just a flat surface of rest even though there might be undulations on the ground, see Figure 3.16.

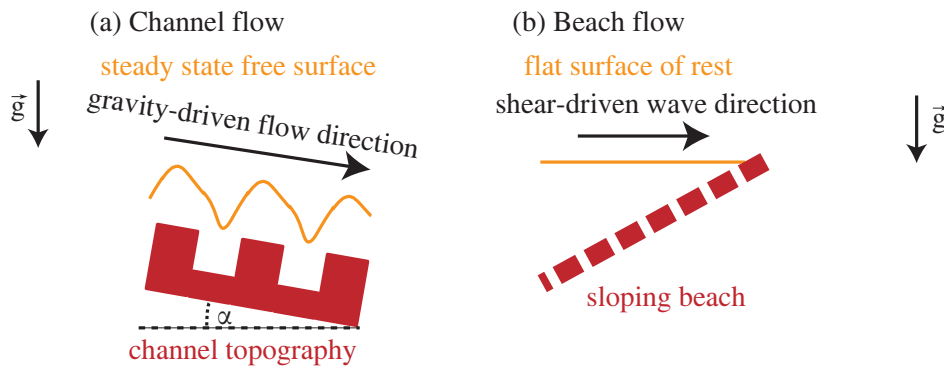


Figure 3.16.: Sketch of the basic states with an indication of the driving forces: (a) steady state free surface (yellow curve) for the film flow. (b) flat surface of rest (yellow line) for water waves.

Concluding, the theory of shallow water waves is not applicable to our system since the viscosity, the bottom slope, the driving force and the undulation of the steady state free surface differ strongly between both cases.

There is no theoretical nor experimental work available on the physical mechanisms, which are responsible for the wave breaking and surface wave collapsing in film flows. Therefore, this Section focuses on the influences of the substrate's shape and wavelength, the excitation frequency and amplitude on the traveling wave.

The present Section 3.2 is based on the publication "*Breaking of waves on thin films over topographies*" by Dauth and Aksel [143].

#	W (mm)	L (mm)	λ_b (mm)	shape
0	0 or ∞	0 or ∞	0 or ∞	<i>Flat</i>
1	10	10	20	<i>Rec</i>
2	10	20	30	<i>Rec</i>
3	10	30	40	<i>Rec</i>
4	10	50	60	<i>Rec</i>
5	10	100	110	<i>Rec</i>
6	20	10	30	<i>Rec</i>
7	20	20	40	<i>Rec</i>

Table 3.1.: The list of all substrate combinations used for measurements. Different length combinations of top of the trench (W) and bottom of the trench (L) are used.

3.2.2. Measured parameter space

The experiments in this Section have been carried out on the rectangular *Rec* and *Flat* substrate, shown in Figure 2.3 (b). The list of all combinations of W and L is shown in Table 3.1.

All measurements were taken at an inclination angle of

$$\alpha = (10.0 \pm 0.1)^\circ, \quad (3.7)$$

a temperature of

$$\theta = (23.0 \pm 0.1)^\circ\text{C}, \quad (3.8)$$

and a volume flux of

$$\dot{V} = (187 \pm 3) \frac{\text{cm}^3}{\text{s}}. \quad (3.9)$$

The corresponding Reynolds number Re , Nusselt film thickness h_n and the free surface velocity for the Nusselt flow $u_{s,n}$ can be calculated by Equations 2.2 and 2.3:

$$Re = 16.0 \pm 0.5, \quad (3.10)$$

$$h_n = (5.8 \pm 0.1) \text{ mm}, \quad (3.11)$$

$$u_{s,n} = (282 \pm 6) \frac{\text{mm}}{\text{s}}. \quad (3.12)$$

3.2.3. Steady flow

For all measured substrates, except the flat substrate, an undulated steady state free surface is observable. In Section 3.1, it was stated that the steady state free surface is decisive for the evolution of the traveling wave concerning the wave's shape and wavelength. The steady state free surfaces are plotted in Figure 3.17 for the flat and all undulated substrates. For the substrates with $W/L = \{10/10; 20/10\}$ the steady state free surface is almost flat and similar to the steady state free surface of a flat substrate. For all other substrates a more pronounced curvy steady state free surface is observable. Nevertheless, the magnitude of the curvature shows major differences between the different substrates. This will be discussed in more detail in the following Sections.

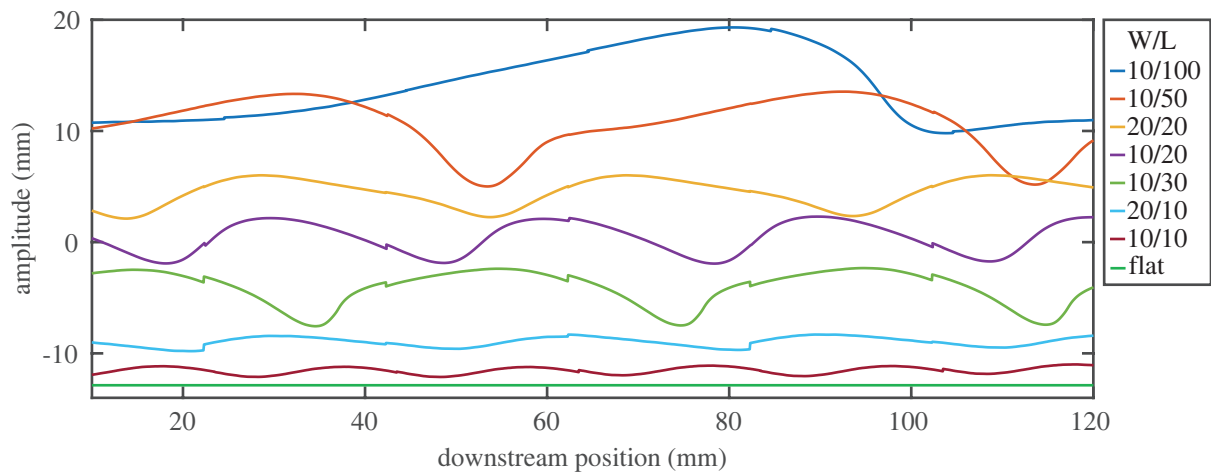


Figure 3.17.: The steady state free surfaces for all substrates measured in this Section 3.2. An offset was added to some curves for the sake of lucidity. Modified and reprinted with permission from Dauth and Aksel [143]. © AIP Publishing.

3.2.4. Screening different evolutionary behavior of the traveling wave

In Figure 3.18, the evolution of the maximal amplitudes of two waves is plotted over the complete measurement length of two different substrates. The two substrates shown provoke a different behavior of the traveling free surface wave referring to the amplitude evolution. The red curve represents the amplitude of the traveling wave over the substrate with $W = 10$ mm and $L = 50$ mm, see Figure 2.3 (b) and (c), and shows first an exponential growth of the amplitude and then a saturation. For the processing of the amplitude discrete steps of 20 mm in downstream-direction were used. For each discrete step the maximal amplitude in the 20 mm x-space and the whole time space (6s, 1200 frames) measured was searched. The resulting maximal amplitude is plotted in Figure 3.18. The spikes in the saturation region result from the data processing: the steady state free surface is subtracted from the time-dependent resulting free surface, hence the top of the trench shows a slightly higher amplitude than the bottom of the trench, as described in Section 2.2.4 and exemplarily shown in Figure 2.16.

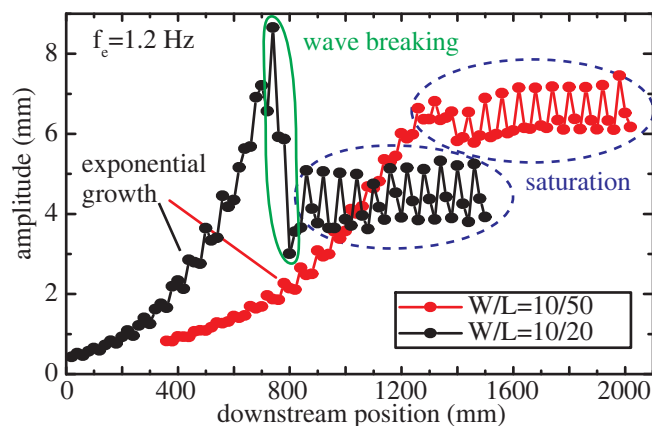


Figure 3.18.: Amplitude plot of traveling free surface waves over two different topographies with $W/L = 10/50$ (red) and $W/L = 10/20$ (black) with the excitation frequency $f_e = 1.2$ Hz. The chart characteristics are circled and named. Modified and reprinted with permission from Dauth and Aksel [143]. © AIP Publishing.

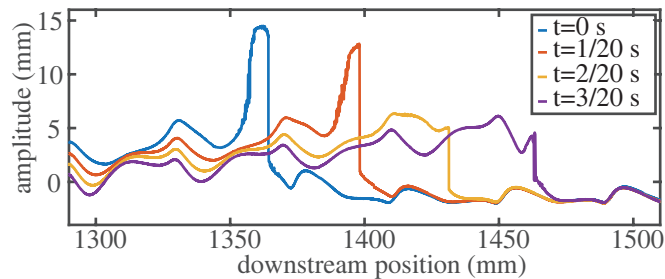


Figure 3.19.: Time evolution of one traveling wave with $f_e = 1.0$ Hz over the substrate with $W/L = 20/20$ for four different time steps for a small excerpt of the whole measurement distance. Modified and reprinted with permission from Dauth and Aksel [143]. © AIP Publishing.

For the black curve over the substrate with $W = 10$ mm and $L = 20$ mm a different evolution of the amplitude of the traveling wave is observable. First an exponential growth is visible but unlike the other graph the evolution of the amplitude does not show a saturation but abruptly decreases in amplitude. This mechanism is denoted as wave breaking. After the wave breaking a saturation similar to that on the other substrate occurs. However, it is worth noting that in the red graph the maximal amplitude is the saturation amplitude and for the black graph the maximal amplitude is almost twice as big as the saturation amplitude. This is the first report in literature that a surface wave collapses in a gravity-driven viscous thin film flow [143].

Such a wave breaking effect is also visible for the substrate with $W/L = 20/20$. The wave breaking mechanism can be shown in either the amplitude evolution of the traveling wave or in the time evolution of the wave. In Figure 3.19, the time evolution of the traveling free surface wave ($f_e = 1.0$ Hz) over the substrate with $W = 20$ mm and $L = 20$ mm is plotted for different time steps with $\Delta t = 1/20$ s. For the sake of lucidity, only a small excerpt of the measurement distance is picked, i.e., $x = [1290; 1510]$ mm. The blue line which represents $t = 0$ s shows the maximal amplitude of the traveling wave. For the next time step $t = 1/20$ s (red line), the amplitude of the traveling free surface wave has already slightly decreased. For one time step further $t = 2/20$ s (yellow line), the amplitude reaches a minimum, which is less than half of the maximal amplitude at $t = 0$ s. This rapid ($\Delta t = 2/20$ s) decrease of the traveling wave's amplitude corresponds to the above-mentioned wave breaking and constitutes a new feature for traveling waves over thin film flows. For further time steps, the amplitude of the traveling wave increases again to a saturation amplitude. This phenomenon was also visible in Figure 3.18 for the wave over a different substrate ($W/L = 10/20$). The graphs in Figure 3.19 give the reader an understanding of the time period in which the wave breaking happens.

3.2.5. Screening different substrates and excitation frequencies

In this Section, the behavior of the traveling waves over substrates is analyzed in more detail. In Figure 3.20, the amplitude evolution for four exemplary substrates at various frequencies is displayed. It can be distinguished between three different types of evolutionary behavior, namely saturation, single wave breaking, and multiple wave breaking. In Table 3.2, the substrates and the corresponding categorization of the above given wave evolution behavior are listed. Here, only the most prominent examples are selected from all experiments carried out in this study.

The well-known case of the flat substrate ($W = 0$ or ∞ ; $L = 0$ or ∞), see Figure 3.20 (a), serves as a reference for the wave evolution. In all other substrates, a bottom undulation is yielded

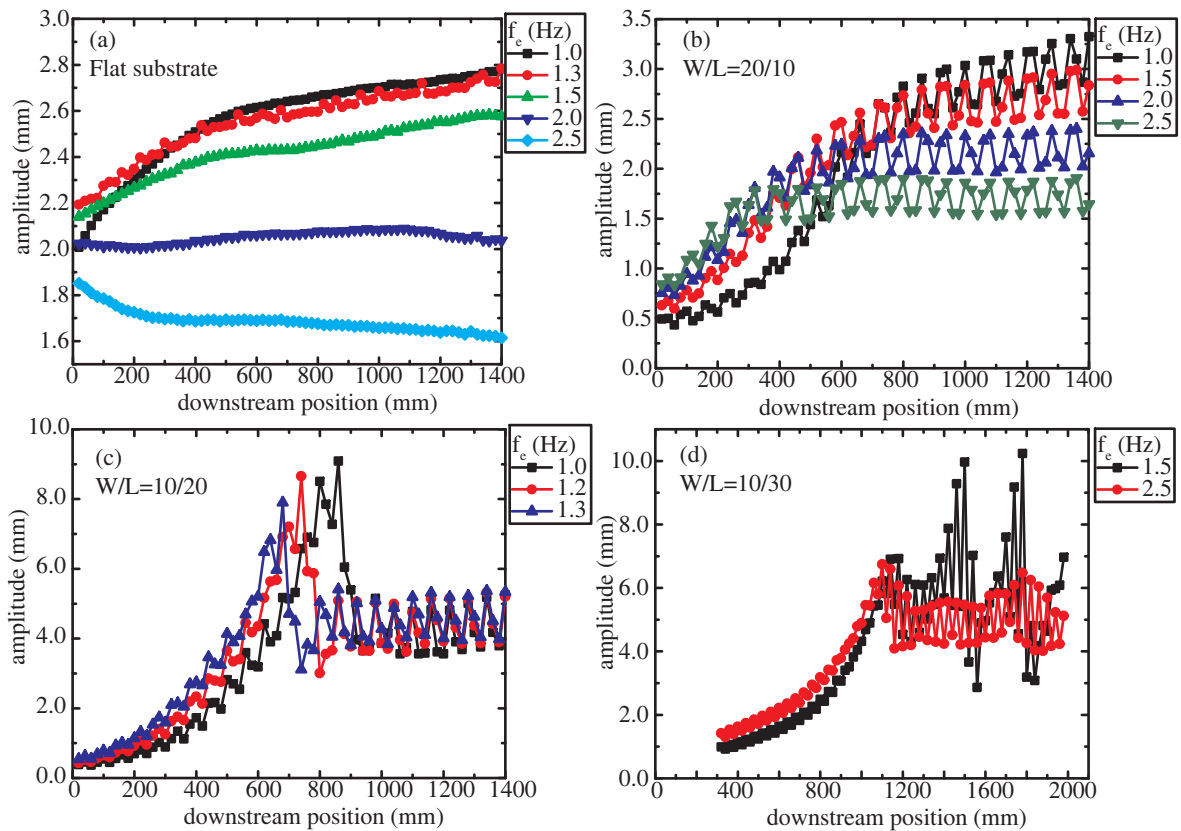


Figure 3.20.: Amplitude plots for four exemplary measured substrates (see Table 3.1) for different excitation frequencies. The three different amplitude evolutions (saturation, single wave breaking, and multiple wave breaking) visible in the plots are listed and categorized in Table 3.2. Modified and reprinted with permission from Dauth and Aksel [143]. © AIP Publishing.

due to the variation of the two building blocks in a not limiting case and hence an undulated steady state free surface, see Figure 3.17.

For the substrates with the combinations $W/L = \{10/10; 20/10; 10/50; 10/100\}$ and the flat substrate, which are represented by the graphs (a) and (b) in Figure 3.20, the amplitudes show an exponential growth and a saturation, when the disturbance is settled in the convectively unstable regime. For the waves with a frequency within the stable area, the amplitude just decreases.

Reck and Aksel [125] found recirculation areas underneath free surface waves, which made the wave become saturated. These recirculation areas were found in solitary waves over a flat substrate. It was not possible to measure these surface rollers for the geometries used due to the two-dimensional movement of the traveling wave caused by the undulated substrates. Nevertheless, it is assumed that these surface rollers primarily lead to a non-breaking saturated wave for unstable frequencies.

Furthermore, a new kind of behavior for traveling waves over thin film flows is observed. The substrates with $W/L = 10/20$ and $W/L = 20/20$, which are represented in Figure 3.20 (c) by $W/L = 10/20$, exhibit an exponential growth and a rapid decrease of the amplitude of the traveling wave, which is interpreted as a single wave breaking (please compare to Figure 3.18 and 3.19). The amplitude reached a saturation level after the wave has broken. The saturation is similar to the substrates discussed before. This means the traveling free surface wave grows

#	W (mm)	L (mm)	saturation	single wave	multiple wave
0	0 or ∞	0 or ∞	x		
1	10	10	x		
2	10	20		x	
3	10	30			x
4	10	50	x		
5	10	100	x		
6	20	10	x		
7	20	20		x	

Table 3.2.: List of all substrates and the categorization for the three phenomena (saturation, single wave breaking and multiple wave breaking).

rapidly until it is in an energetically unstable state, collapses, and finds an equilibrium state.

Another behavior for the amplitude evolution of the traveling free surface wave was found over the substrate with $W/L = 10/30$ [Figure 3.20 (d)]. There, an exponential growth followed by a wave breaking and a rapid re-growth and re-breaking of the wave was found. The difference to the case discussed before with the single wave breaking is that the amplitude does not converge into a saturation level but shows multiple wave breaking. This leads to the conclusion that the wave can not find an equilibrium state for the amplitude within the observation area when multiple wave breaking occurs.

For all substrates, a set of excitation frequencies was measured but for the sake of lucidity only a few curves for the exemplary substrates are shown in Figure 3.20. In Figure 3.21, the wave evolution is shown for one fixed frequency over three different substrates. By comparison of the graphs it can be concluded that the critical frequency, at which the last wave breaking characteristic occurs, is a function of the steady state free surface as a reaction to the substrate. For the substrate with $W/L = 20/20$, the excitation frequencies $f_e = \{1.0; 1.1; 1.2\}$ Hz show a single wave breaking. The geometry with $W/L = 10/20$ shows single wave breaking for $f_e = \{1.0; 1.1; 1.2; 1.3; 1.4; 1.5\}$ Hz. Multiple wave breaking occurs at $f_e = \{1.4; 1.5\}$ Hz on the substrate with $W/L = 10/30$. In order to find these critical values the excitation frequencies was scanned in 0.1 Hz steps.

In Figure 3.20 (b), the four excitation frequencies show different saturation amplitudes. That the saturation amplitude is a function of the excitation frequency on substrates, which show a normal saturation, can also be seen in Figure 3.20 (a). In Figure 3.20 (c), the excitation frequencies $f_e = \{1.0; 1.2; 1.3\}$ Hz show a similar saturation amplitude. For the two geometries, which show single wave breaking, the saturation amplitude after the wave breaking is similar and hence not a function of the excitation frequency in contrast to the substrates with the normal saturation.

In Section 3.1, it was shown that the flat substrate is the limiting case for all substrate shapes when the wavelength tends against zero or infinity. Therefore, the flow characteristics converge for very short and long wavelength to the limiting case. In the experiments, a similar trend for the categorization is observable. Substrates with a very long wavelength compared to the length of the top of the trench show a normal saturation, see $W/L = 10/100$. In the other direction for a very short wavelength, the same trend is visible, see $W/L = 10/10$.

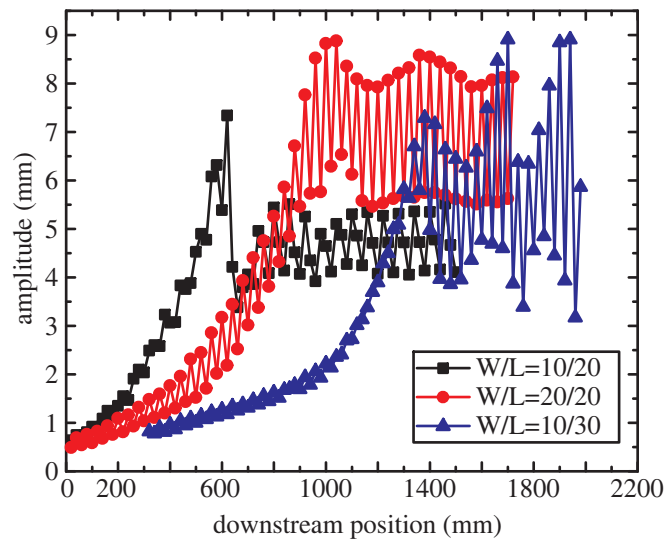


Figure 3.21.: Amplitude plots for $f_e = 1.4$ Hz over different substrates. Modified and reprinted with permission from Dauth and Aksel [143]. © AIP Publishing.

3.2.6. Screening the excitation amplitude

In Section 3.2.5, different excitation frequencies f_e were considered and a strong dependence of f_e on the categorization was observed. For all measurements shown until now, the paddle excitation amplitude A_e was set to 8 mm. Now this amplitude was varied, and two more values were studied. The steady state flow was excited with $A_e = \{0.5; 8.0; 16.0\}$ mm. The smallest amplitude is a borderline case between linear and nonlinear excitation [99]. With higher excitation amplitudes $A_e = 8.0$ and 16.0 mm, nonlinear waves were excited with a difference in their nonlinearity.

In Section 3.1 and in the work by Dauth *et al.* [139], it was shown that the excitation amplitude does not influence the evolution of the wave's shape and curvature. The results presented in the present Section 3.2 extend those results on waves that can break: The excitation amplitude does not affect the wave breaking character. Therefore, no graph is shown. This means that linear and nonlinear waves transform into strongly nonlinear waves on their way downstream, which break when their amplitude exceeds a threshold level.

3.2.7. Screening the wave breaking

Figure 3.22 (a) shows the time resolution of a traveling wave breaking over the substrate with $W/L = 20/20$. Each of the seven time steps correlates to a picture in Figure 3.22 (b). The pictures in Figure 3.22 (b) were taken with a high-speed camera from above the channel, which was illuminated with spotlights. The frame rate was set to 200 fps. The blue dotted line represents the wave front. Due to the no slip condition of the rigid boundaries, the wave fronts are curved similar to Georgantaki *et al.* [83]. In line with the case of Georgantaki *et al.* [83], the variation of the curvature in the flow direction is not visible. For the time step $t = 0$ s, the wave has not collapsed yet, hence only the blue line is marked. This wave serves as a reference frame for the following time steps and shows the maximum amplitude of all graphs plotted in Figure 3.22 (a). For the next time step $t = 13/200$ s, the amplitude already slightly decreased from its maximal value. In Figure 3.22 (b), a broad bubble, which almost extends over the whole channel width, underneath the wave's surface is visible and for the sake of lucidity circled

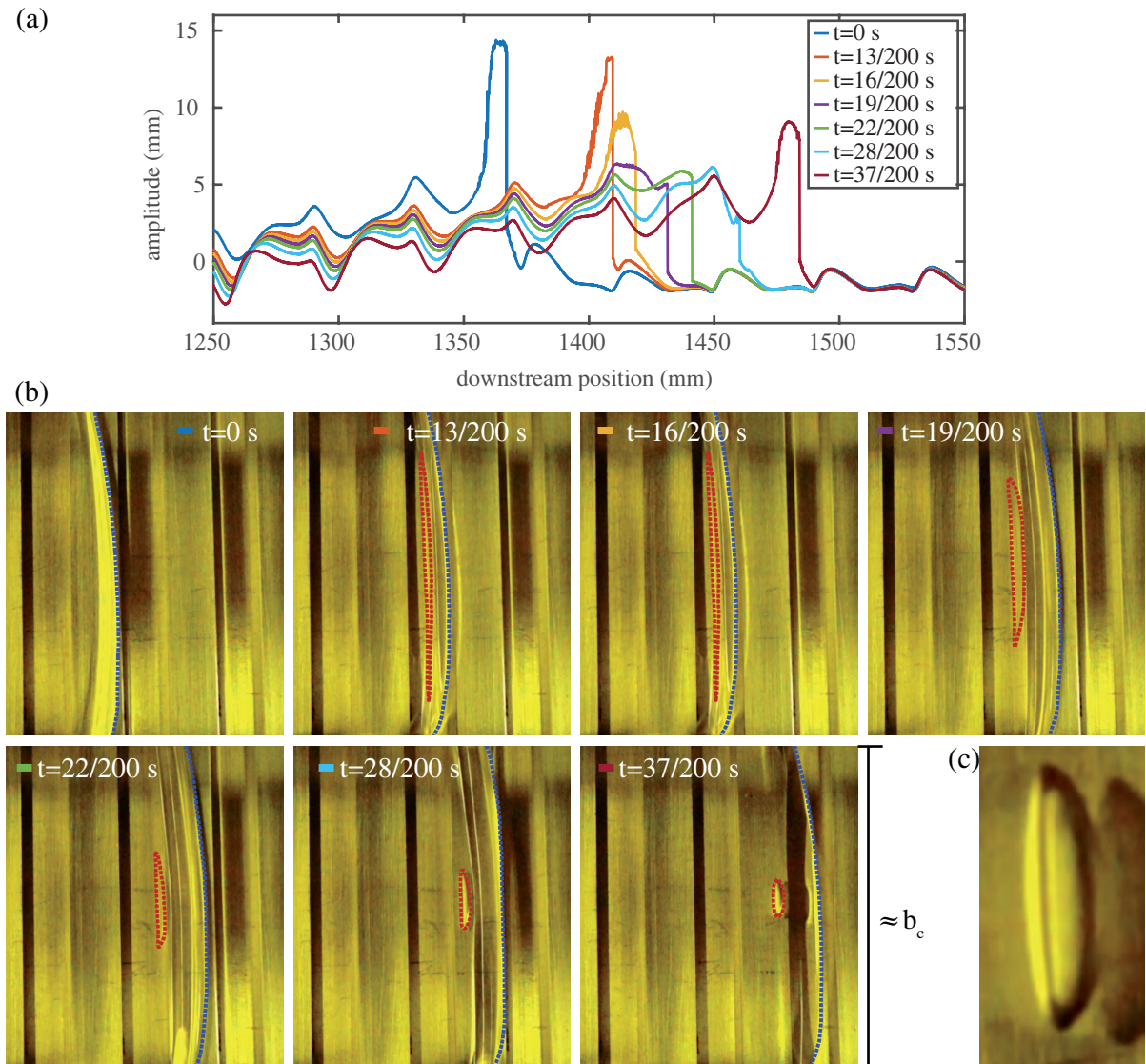


Figure 3.22.: (a) Time evolution of the traveling wave over the substrate with $W/L = 20/20$ (see wave breaking in Figure 3.20 (c) for $W/L = 10/20$) with the excitation frequency $f_e = 1.0$ Hz for various time steps. (b) The view of the traveling wave from above for the time steps used in (a). The wave front is marked with a blue dotted line and the emerging bubble is circled with a red dotted line. For the sake of comparison the width of the pictures corresponds to the channel width b_c . (c) For the sake of lucidity a bubble is enlarged. Modified and reprinted with permission from Dauth and Aksel [143]. © AIP Publishing.

by a red dotted line. This means the wave already collapsed but the amplitude just slightly decreased. The wave is breaking over the whole channel width, therefore the encapsulation of air initially extends over the whole channel width. The broad bubble, encapsulated in the wave, tries to minimize its surface while following the wave front. Hence, it contracts to an energetically favorable state, as visible in the following time steps. The contracted bubble at the channel center then rises to the surface of the traveling wave due to buoyancy. Furthermore, it has to be mentioned that the bubble is traveling slower than the wave, which can be shown by the distance of the blue and red dotted lines. That means the wave front strides away from the bubble. The bubble is enlarged displayed in Figure 3.22 (c) and in Figure A.1 in the

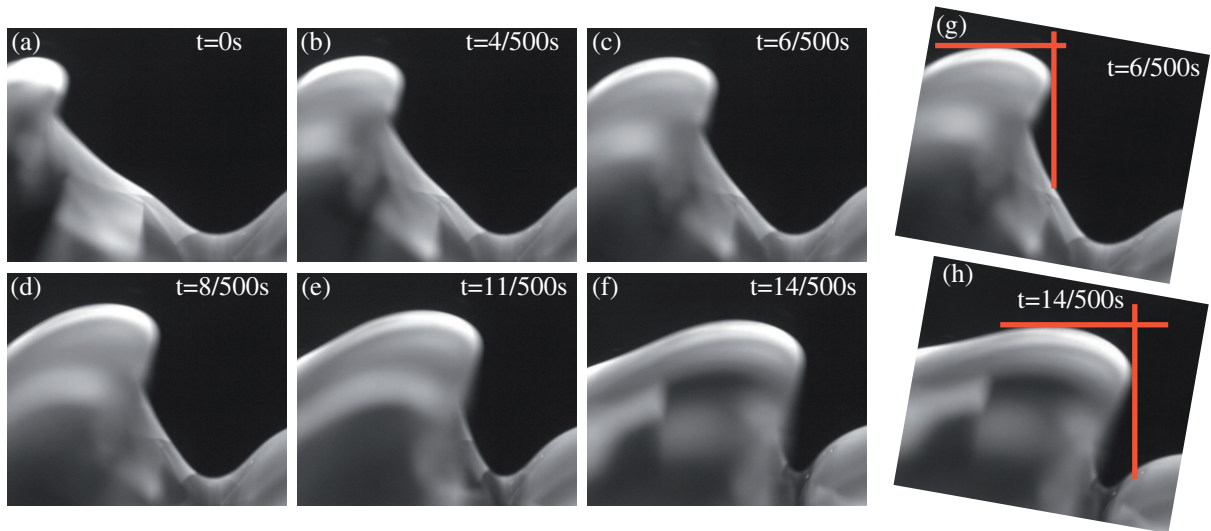


Figure 3.23.: The raw data of the traveling wave over the substrate with $W/L = 20/20$ with the excitation frequency $f_e = 1.0\text{Hz}$ recorded with a frame rate of 500 fps. Pictures (a) - (f) are already corrected by the inclination angle $\alpha = 10^\circ$. In (g) and (h) the red lines mark the maximal amplitude and the wave front, making the overlap more visible. Modified and reprinted with permission from Dauth and Aksel [143]. © AIP Publishing.

Appendix. Furthermore, a video of the bubble creation is available as supplementary material of the publication by Dauth and Aksel [143]. Varchanis *et al.* [152] also found air inclusions on films flowing down a rectangular corrugated vertical wall.

As mentioned before, the wave already broke for the time step $t = 13/200\text{s}$, but the amplitude of the traveling wave only slightly decreases from the steps $t = 0\text{s}$ to $t = 13/200\text{s}$. This phenomenon can be explained with the help of Figure 3.23. The pictures (a) - (f), which show the raw recorded images of the film flow, are already corrected by the inclination angle of the channel $\alpha = 10^\circ$. As visible, the maximum amplitude of the traveling wave is not directly at the wave front. The amplitude decreases when the bubble formation continues and the bubble shifts out of the area with the maximum amplitude. In Figure 3.23, the time steps of the pictures are given in the frames. The raw data is shown for an area around the x-coordinate where the wave collapses.

Furthermore, it has to be mentioned that the wave shows an overlap at the wave front depicted with red lines in Figure 3.23. This is already visible in Figure 3.23 (a) - (f) but the waves are already corrected by the inclination angle α , there. In Figure 3.23 (g) and (h), the α -uncorrected pictures are shown for the sake of lucidity of this overlap. In the raw data of the waves over the substrates which do not show the wave breaking the overlap is not visible.

3.2.8. Screening the Fourier wave number space

In this Section, a closer look is taken at the waves before and after the wave breaking. Therefore, the wave number Fourier space and the time evolution of the wave were analyzed. The evolution of the wave over one time period is shown in Figure 3.24. It has to be remarked that only the traveling wave for the Fourier analysis was used by subtracting the steady state free surface from all time-dependent surfaces, see Section 2.2.4 and Dauth *et al.* [139]. In Figure 3.25, the Fourier analysis of the traveling waves is shown for two distinct areas of the measurement distance. For the traveling wave over the $W/L = 20/10$ substrate [see saturation in Figure 3.20

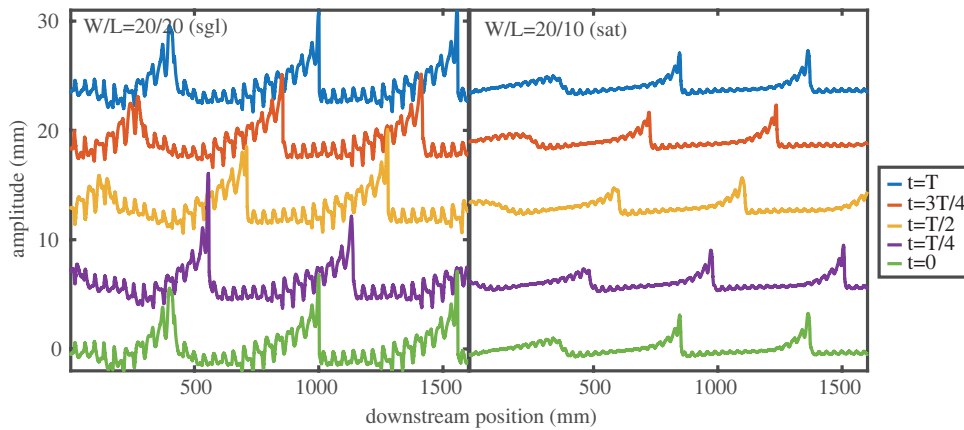


Figure 3.24.: Time evolution of the traveling wave with $f_e = 1.0$ Hz over one time period in $T/4$ steps. An offset was added to some curves for the sake of lucidity. Modified and reprinted with permission from Dauth and Aksel [143]. © AIP Publishing.

(b)], the whole measurement distance excluding 200 mm inlet length was used, the resulting distance was divided in two sections (Beginning & End) and the 1D-Fourier was computed for both regions. Both curves show a similar behavior. The main peak which represents the excitation frequency f_e and the beat wave numbers around $k \approx 33 \text{ m}^{-1}$ are almost identical for both curves. The only real difference is the strength of the higher harmonics of the main excitation. In the first region (Beginning, blue curve), the wave is still growing and the second region (End, red curve) mainly represents the saturated, fully developed wave, hence the higher harmonics are better visible. Beat wave numbers have already been discussed and explained in Sections 3.1.3 and 3.1.5 and by Dauth *et al.* [139] and Reck and Aksel [126].

For the graph in Figure 3.25 with the Fourier analysis of the wave over the substrate with $W/L = 20/20$ [see wave breaking in Figure 3.20 (c)], the separation is not that easy. The same inlet length was subtracted from the beginning of the channel. The separation point for the two Fourier analysis spaces is the x -coordinate of the wave breaking. Around this decisive point, a small space puffer is subtracted in both directions in order to avoid any wave breaking frequency phenomena into the Fourier analysis. For the blue curve (Beginning), the main peak representing the excitation frequency f_e and the beat wave numbers around $k = 25 \text{ m}^{-1}$ and $k = 50 \text{ m}^{-1}$ are visible. There are almost no higher harmonics of the excitation frequency visible in the Fourier space.

The second curve for the end of the channel (red line in Figure 3.25) mainly shows the saturated new generated wave, which is caused by the wave breaking mechanism. For this domain, the main peak representing the excitation frequency and multiple distinct higher harmonics are visible. Furthermore, some major peaks are observable in the region of the beat wave numbers, yet these are shifted and not as clear as in the region before the wave breaking. This is in contrast to the similarity of the Fourier data of the substrate without the wave breaking. It means the wave before and after the wave breaking is very different and it can be concluded that a new wave emerged from the wave breaking.

3.2.9. Screening the wave impact

In Section 3.2.7, the raw data of the traveling free surface wave was shown in order to clarify the amplitude behavior during and after the wave breaking with a special attention to the air

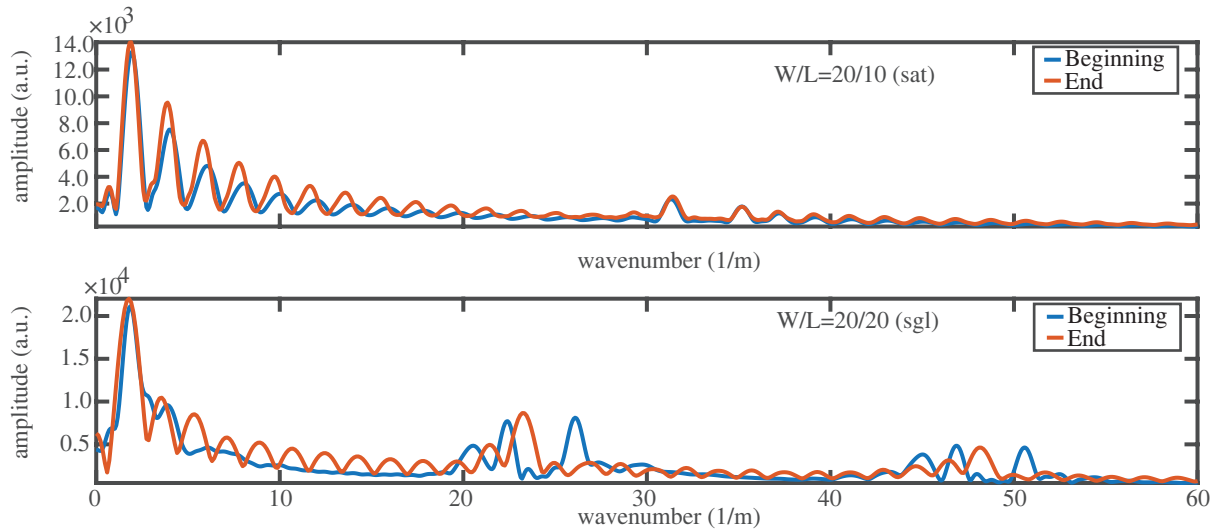


Figure 3.25.: Wave number Fourier spectra for two different substrates $W/L = 20/10$ (top), with saturation, abbreviated with sat, see Fig 3.20 (b) and $W/L = 20/20$ (bottom), with single wave breaking, abbreviated with sgl, see Fig 3.20 (c) with the excitation frequency $f_e = 1.0$ Hz: For $W/L = 20/10$ (top) the measurement length less 200 mm inlet length was divided in half as described in Section 3.2.8. The first area is shown in blue, marked as “Beginning”, and the second area is shown in red, marked as “End”. For $W/L = 20/20$ (bottom) the inlet length was also subtracted and the measurement area was divided in before and after the wave breaking. Modified and reprinted with permission from Dauth and Aksel [143]. © AIP Publishing.

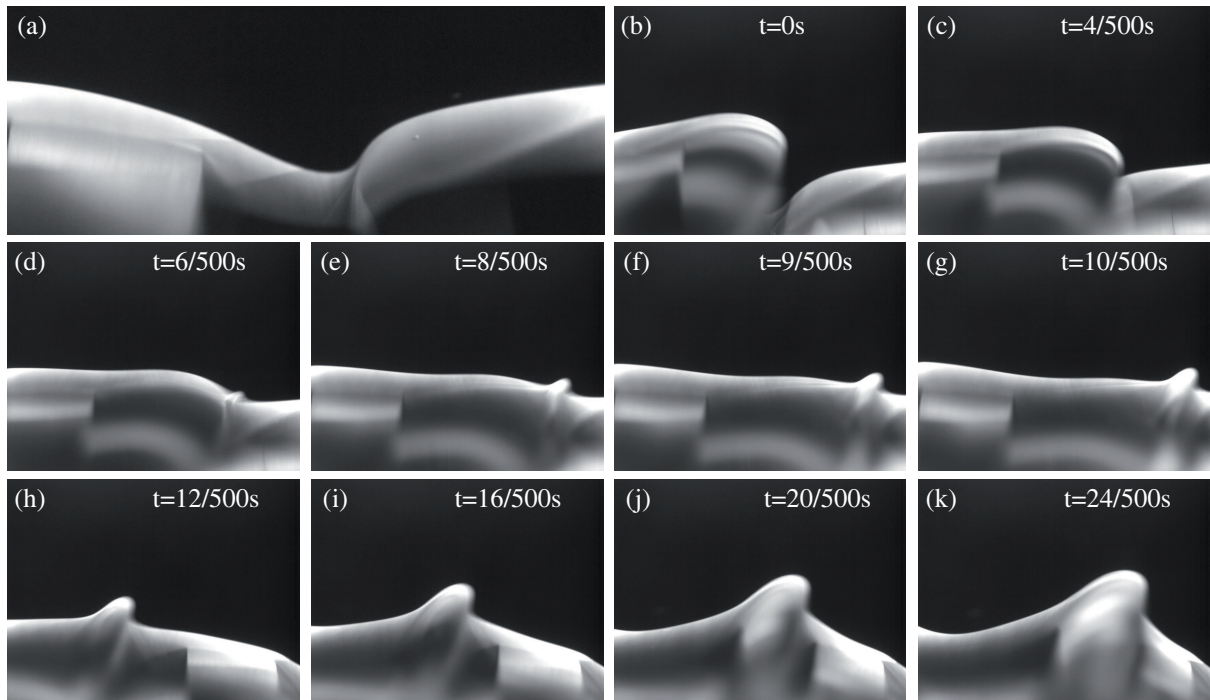


Figure 3.26.: (a) The raw image of the steady state free surface of the liquid oil film over the undulated substrate. (b) - (g) Raw images of the wave falling into the trough with a jet emerging. (h) - (k) The adjacent repeating unit as a sequel to (b) - (g). Modified and reprinted with permission from Dauth and Aksel [143]. © AIP Publishing.

inclusion in the wave. In this Section, new findings of the impact of the traveling wave on the steady state flow are shown. Since the channel including the substrate is inclined and undulated geometries are used, a strongly curved steady state free surface is yielded. The steady state free surface raw data is displayed in Figure 3.26 (a). In Figure 3.26 (b) and (c), the wave is on its way breaking into the trough. The wave similar to the one in Figure 3.23 almost vanishes by flattening out the trough, caused by the undulated substrate. After flattening the trough a baby jet emerges, see Figure 3.26 (d). Eventually the jet evolves into a fully developed wave. In order to get an understanding of the time domain for this process, time steps are given in the pictures, whereas Figure 3.26 (b) was used as a random time reference $t = 0$ s. Notable is that there is no pinch-off during the formation of the jet.

3.2.10. The steady state free surface as a major influencing parameter

Considering that always the same wave is impressed onto the steady flow for all substrates and the waves develop so differently, the substrate and hence the steady state free surface might have a major influence on the development of the traveling free surface wave. The steady state free surfaces for the different substrates are plotted in Figure 3.17. It can be assumed that the curvature of the steady state free surface mainly influences the evolution of the traveling free surface wave, i.e., the wave breaking mechanism. The substrates with a very long trough compared to the top of the trench ($W/L = \{10/50; 10/100\}$) show a smooth steady state free surface despite the area around the top of the trench. In this area, the local curvature is steep. All these substrates priorly discussed in this Section exhibit an amplitude evolution which does not show a wave breaking mechanism. This means that not only a weak curvature but also an only locally strong curvature does not lead to the new phenomena discussed in this Section. Therefore, a strong mean or global curvature of the steady state free surface is required to see the wave breaking mechanism of the traveling free surface wave.

For a closer look on the curvature of the steady state free surface, the first derivative of the surface function is calculated. The derivatives are shown in Figure 3.27 and also indicate that not only a locally strong curvature is sufficient for a wave evolution which leads to wave breaking. This can be seen at the substrate with $W/L = 10/50$, for which the changes in curvatures around the top of the trench are more pronounced. Nevertheless, a wave breaking did not occur for any excitation frequency and amplitude.

3.2.11. Conclusion

In Section 3.2, thin film gravity-driven traveling free surface waves over undulated substrates in a channel were considered. The steady state flow was perturbed with continuous waves of different excitation frequencies. As substrates seven different variations made of building blocks were used, see Figure 2.3 (c) and Table 3.1.

New phenomena concerning the evolution of the wave's amplitude were reported. The first wave breaking on this kind of flow was revealed and shown. Depending on the substrate's shape it can be distinguished between three different possible categories. First, the wave is exponentially growing and converges into a saturation amplitude, see Figure 3.20 (a) and (b). This was already seen by Dauth *et al.* [139], Reck and Aksel [126], and in Section 3.1. It was assumed that surface rollers keep the wave on its way downstream in a stable condition [125]. Second, the wave is exponentially growing until it reaches an undefined high amplitude and then abruptly collapses. After the collapse, the wave converges into an amplitude saturation, see Figure 3.20 (c). This

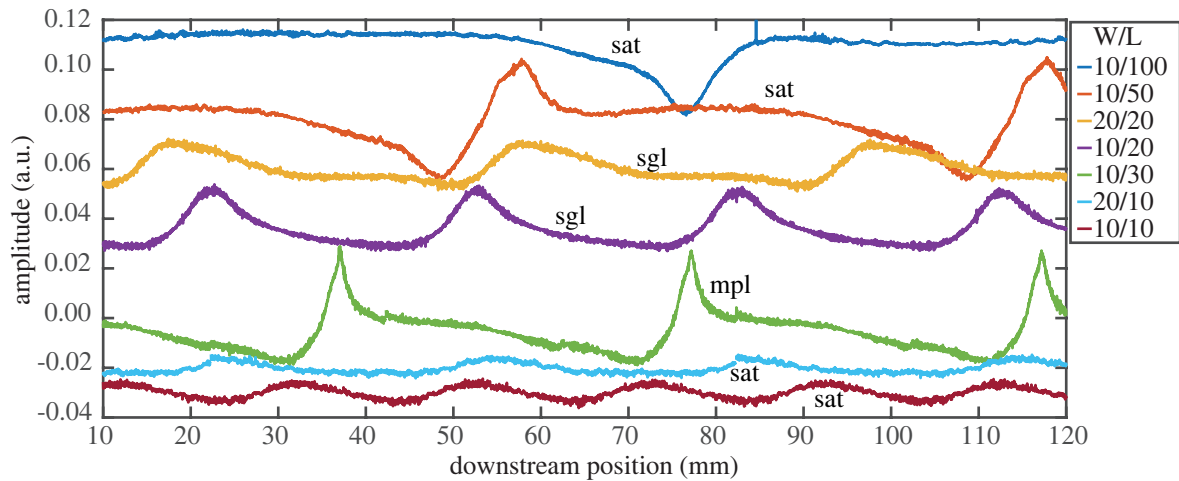


Figure 3.27.: The derivatives of the steady state free surfaces for all substrates measured in this Section 3.2. An offset was added to some curves for the sake of lucidity. For the categorization see Table 3.2. The graphs are denominated with abbreviations: sat means saturation, sgl means single wave breaking, and mpl means multiple wave breaking. Modified and reprinted with permission from Dauth and Aksel [143]. © AIP Publishing.

collapse is denominated as single wave breaking. At the wave breaking a broad air encapsulation is visible underneath the surface of the traveling wave. This encapsulation extends over the whole channel width, see Figure 3.22 (b). It contracts over time and forms a bubble at the channel center. The bubble arises from underneath the wave to the surface of the oil film. Third, the waves show an alternating exponential growth and wave breaking, see Figure 3.20 (d). This mechanism is denoted as multiple wave breaking.

For the waves over the substrates which show a single or multiple wave breaking a very narrow band of excitation frequencies is reported where these new phenomena can occur. For all substrates, the limiting excitation frequency differs despite having all other parameters fixed. This leads to the conclusion that the critical frequency is a function of the substrate.

That the substrate's shape is decisive for the evolution of the wave and the developed wave shape was previously discussed by Dauth *et al.* [139] and Section 3.1. In this Section 3.2, it was taken one step further and it was postulated that the steady state free surface and its curvature are crucial for the categorization mentioned before, see Figure 3.17. A weak curvature of the steady state free surface does not lead to a single or multiple wave breaking. Also a locally strong curved surface is not sufficient for the wave breaking. Hence, a strong mean or global curvature is needed for the wave breaking mechanism, see Figure 3.27.

In a nutshell, for breaking of waves over gravity-driven viscous films it is necessary that the bottom slope is corrugated with some protruding, prominent, sufficiently high peaks as obstacles which provoke corresponding peaks on the free surface of the steady film flow. The traveling waves surfing over this undulated free surface of the steady film stumble over these peaks and break. This chain of highly nonlinear, geometrical, and dynamic triple interaction of “the substrate – the steady state free surface – the traveling wave” is the necessary cause to effect paradigm of breaking of waves over gravity-driven viscous thin films.

3.3. Turbulent wave fronts on film flows

3.3.1. Motivation

The increase of the inertia from Section 3.1 to Section 3.2 led to various unseen phenomena as wave breaking on gravity-driven thin film channel flows. The fact that some wave breakings bring a saturation with it and others were succeeded by more wave breaking and there is no explanation for that, led to further experiments with an increase of the inertia. The inertia was increased in two ways. First, the Reynolds number was varied. Second, the inclination angle was drastically increased.

In Figure 3.28, two wave fronts recorded from the frontal view are displayed for one bottom undulation ($W/L = 10/30$), equal Reynolds number ($Re = 16$), but different inclination angles [(a) $\alpha = 10^\circ$, (b) $\alpha = 15^\circ$]. For $\alpha = 10^\circ$, a regular shape of the intersection of the wave front is visible, which can be seen by the smooth shape of the bright wave front. The two brighter areas in the picture are caused by overlapping two laser lines. In contrast to $\alpha = 10^\circ$, $\alpha = 15^\circ$ shows an irregular shape of the wave front. This can be seen in the random height distribution of the traveling wave. Both images were taken from the beginning of the wave front, meaning the wave just entered the intersection.

This novel finding of irregular wave fronts triggered a wide range of experiments on the transition of regular to irregular wave fronts. In this Section 3.3, the experimental techniques described in Sections 2.2.4 (wave dynamics) and 2.2.6 (wave screening) were used to study the transition elaborately.

The present Section 3.3 is based on the publication "*Transition of regular wave fronts to irregular wave fronts in gravity-driven thin film over topography*" by Dauth and Aksel [144].

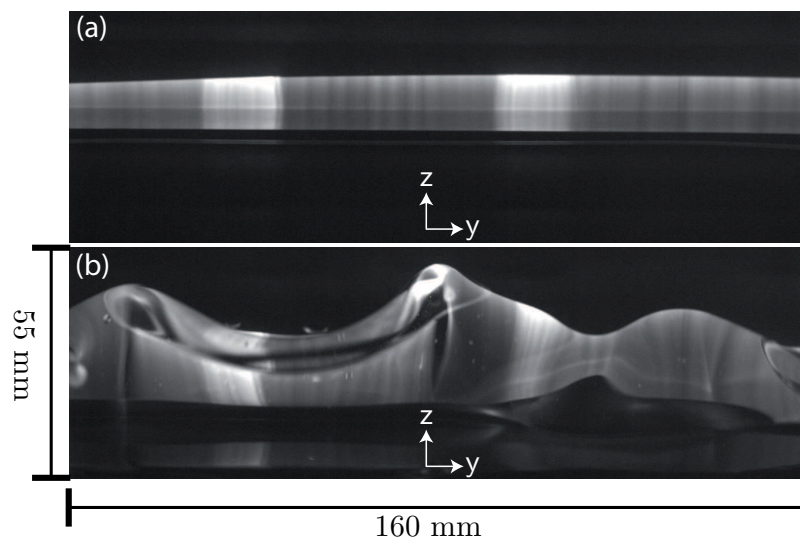


Figure 3.28.: Recorded images from the frontal view of the beginning of waves over the substrate with $W/L = 10/30$ and $Re = 16$. Inclination angles: (a) $\alpha = 10^\circ$, (b) $\alpha = 15^\circ$. Modified and reprinted with permission from Dauth and Aksel [144]. © Springer Nature.

3. Results and discussion

#	W (mm)	L (mm)	λ_b (mm)	shape
0	0 or ∞	0 or ∞	0 or ∞	<i>Flat</i>
1	10	30	40	<i>Rec</i>
2	20	20	40	<i>Rec</i>
3	10	50	60	<i>Rec</i>
4	10	100	100	<i>Rec</i>

Table 3.3.: The list of all substrate combinations used for measurements. Different length combinations of top of the trench (W) and bottom of the trench (L) are used.

3.3.2. Measured parameter space

The experiments in this Section have been carried out on the rectangular *Rec* and *Flat* substrate, shown in Figure 2.3 (b). The list of all combinations of W and L is shown in Table 3.3. All measurements were taken at the temperature

$$\theta = (23.0 \pm 0.1)^\circ\text{C}. \quad (3.13)$$

The volume flux \dot{V} was varied between four discrete steps

$$\dot{V} = ((140; 164; 187; 210) \pm 3) \frac{\text{cm}^3}{\text{s}}. \quad (3.14)$$

The inclination angle was varied between $\alpha = 10.0^\circ$ and 30.0° in various steps

$$\alpha = ((10.0; 11.0; 12.0; 13.0; 14.0; 15.0; 20.0; 25.0; 30.0) \pm 0.1)^\circ. \quad (3.15)$$

The corresponding Reynolds number Re , Nusselt film thickness h_n and the free surface velocity for the Nusselt flow $u_{s,n}$ can be calculated by Equations 2.2 and 2.3 and are shown in Table 3.4 for $\alpha = 10^\circ$ and 30° .

3.3.3. Irregular wave shape

To understand the irregular wave shape [see Figure 3.28 (b)], the whole wave from this specific configuration was analyzed in more detail. The idea of the measurement is displayed in Figure 3.29 (a). Figure 3.29 (b) & (c) shows the evolution of one wave ($f_e = 1.0$ Hz) at different time steps as the wave travels through the illuminated laser intersection. In Figure 3.29 (b), $t = 0$ s was plotted as a reference time step. In the following time steps, the wave front passes through

\dot{V} (cm ³ /s)	Re	$\alpha = 10^\circ$		$\alpha = 30^\circ$	
		h_n (mm)	$u_{s,n}$ (mm/s)	h_n (mm)	$u_{s,n}$ (mm/s)
140	12	5.3	233	3.7	331
164	14	5.6	259	3.9	368
187	16	5.8	282	4.1	401
210	18	6.1	305	4.3	434

Table 3.4.: The list of all volume fluxes and Reynolds numbers used for measurements and the resulting flow parameter for the inclination angles 10° and 30° .

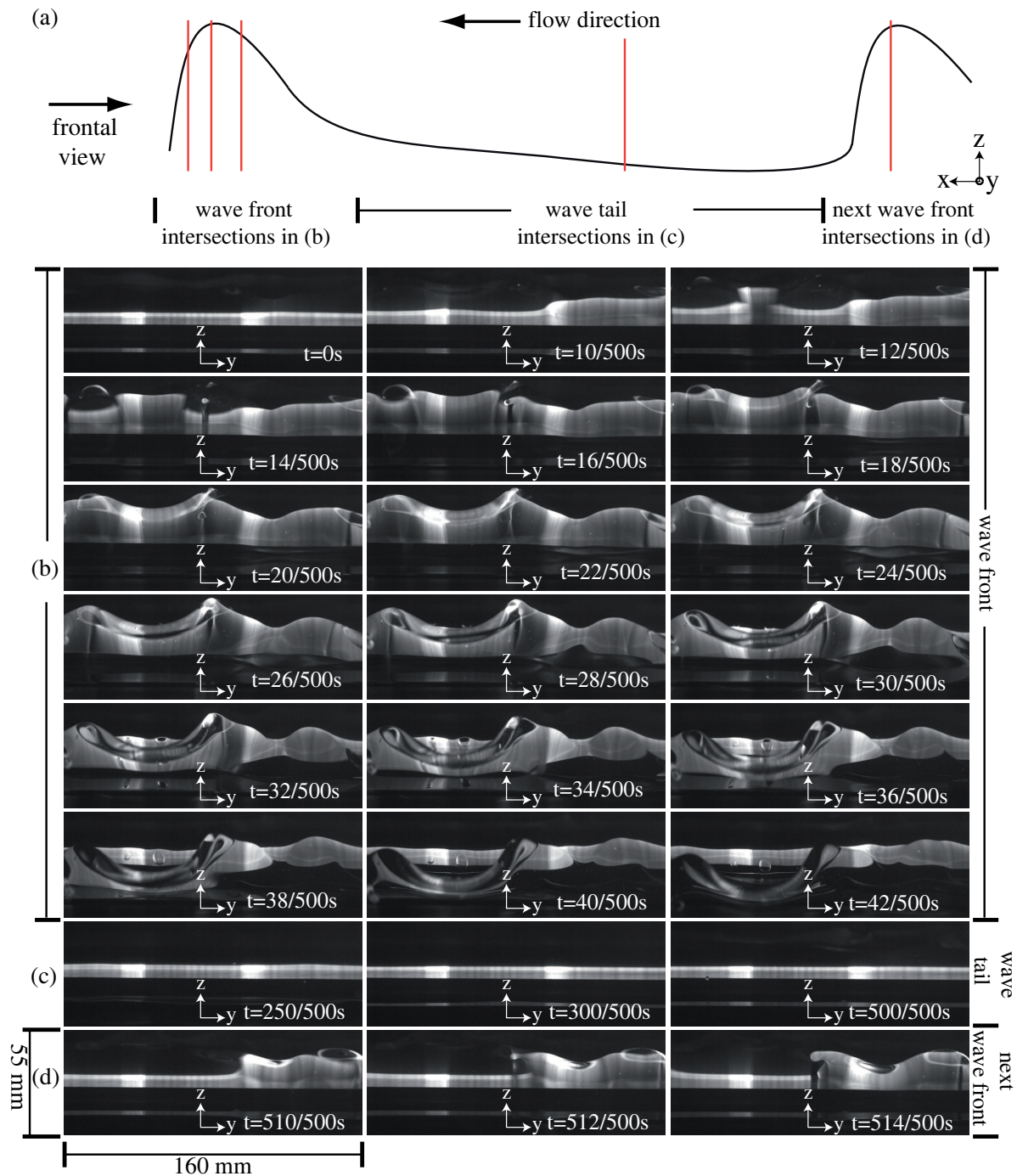


Figure 3.29.: The time evolution at one position in the channel recorded with a frontal view. The waves are traveling over the substrate with $W/L = 10/30$, $Re = 16$ and $\alpha = 15^\circ$. (a) Idealized sketch of the waves measured with exemplary laser intersections indicated by red lines. (b) Shows a good time resolution of one wave front flowing through the illuminated laser intersection perpendicular to the flow direction. (c) Represents the wave tail of the wave shown in (b). (d) Shows the next wave front. Modified and reprinted with permission from Dauth and Aksel [144]. © Springer Nature.

the intersection window. As visible in the time steps $t = 10/500$ and $12/500$ s, the wave front is flowing irregularly into the intersection perpendicular to the flow direction.

In the picture for the time step $34/500$ s, an air encapsulation is clearly visible. This indicates wave breaking phenomena before the wave passes the laser intersection. In Section 3.2 and Dauth and Aksel [143], it was shown that multiple wave breaking is possible on this substrate geometry. This phenomenon was shown for lower inertia ($Re = 16$ and $\alpha = 10^\circ$) which also showed the creation of bubbles but not the irregular wave front shape.

In Figure 3.29 (c), larger time steps are shown representing the wave's tail. The tail of the traveling free surface wave exhibits a regular structure. This demonstrates that the irregular appearance is limited to the beginning of the wave, i.e., the wave front. The irregularity of the wave front can be clearly seen in Figure 3.29 (b), but in order to check whether the irregularity is also chaotic the beginning of the consequent wave is plotted in Figure 3.29 (d). The generated wave had the frequency $f_e = 1.0$ Hz and it was recorded with 500 fps. This means the time steps $10/500$ and $510/500$ s and likewise $12/500$ and $512/500$ s and $14/500$ and $514/500$ s should represent the same position of two consequent waves. The three time step pairs differ strongly. This suggests that the irregularity of the wave front shows chaotic behavior. This chaotic behavior will be discussed in more detail in the following.

In Figure 3.30 (b), intersections of 18 different waves are plotted. This is schematically shown in Figure 3.30 (a). Since the generated waves have the frequency $f_e = 1.0$ Hz and the pictures are recorded with a time-lag of $\Delta t = 1.0$ s, the pictures represent the same position in the waves of consecutive waves. The comparison of the intersections of the wave fronts leads to the conclusion that the waves are not repeating themselves in the measurement. This indicates a chaotic system. A comparison was conducted for various time steps with the same result. This chaotic behavior is limited only to the wave front, the tail of the wave shows a regular shape.

3.3.4. Evolution of traveling waves

The error of the excitation frequency $\Delta f_e = 0.05$ Hz might slightly distort the position in the wave front. To check this, the traveling waves was recorded and it was tried to recombine them with the technique described in Section 2.2.4. As described, areas of the length $x_c = 28$ mm have been recorded with a small overlap. This small overlap is needed to recombine all measured units, as depicted in Figure 2.13. Since the time-gap of the recordings between two adjacent units is random, a cross-correlation algorithm tries to combine all units which results in a wave plot as displayed in Figure 3.31. If the waves are regular, they repeat themselves after the period $1/f_e$ because of their periodic nature, please see Equation 2.8. Hence, the cross-correlation algorithm can recombine the adjacent units by correcting/eliminating all phase mismatches. The phase mismatches can be seen in the lower part of Figure 2.13. The yielded oil-air interface $h_{c,i}(x, t)$ ($i = 2; 3; 4; 5$) shows deviations, representing the phase mismatch.

A regular wave is shown in Figure 3.31 (a) for the substrate $W/L = 20/10$, Reynolds number $Re = 16$, and inclination angle $\alpha = 10^\circ$. The curve of the wave looks sound and has a smooth appearance over the whole measurement distance. The dents in the plot are caused by the used algorithm. The steady state free surface is subtracted from the time-dependent free surface, yielding a higher amplitude at the top of the undulation compared to the bottom of the undulation, see Figure 2.3 (c) in Section 2.1.2. An extract of a traveling wave, which is already corrected by the steady state free surface, over a sketch of a substrate can be seen in Figure 2.16 in Section 2.2.4.

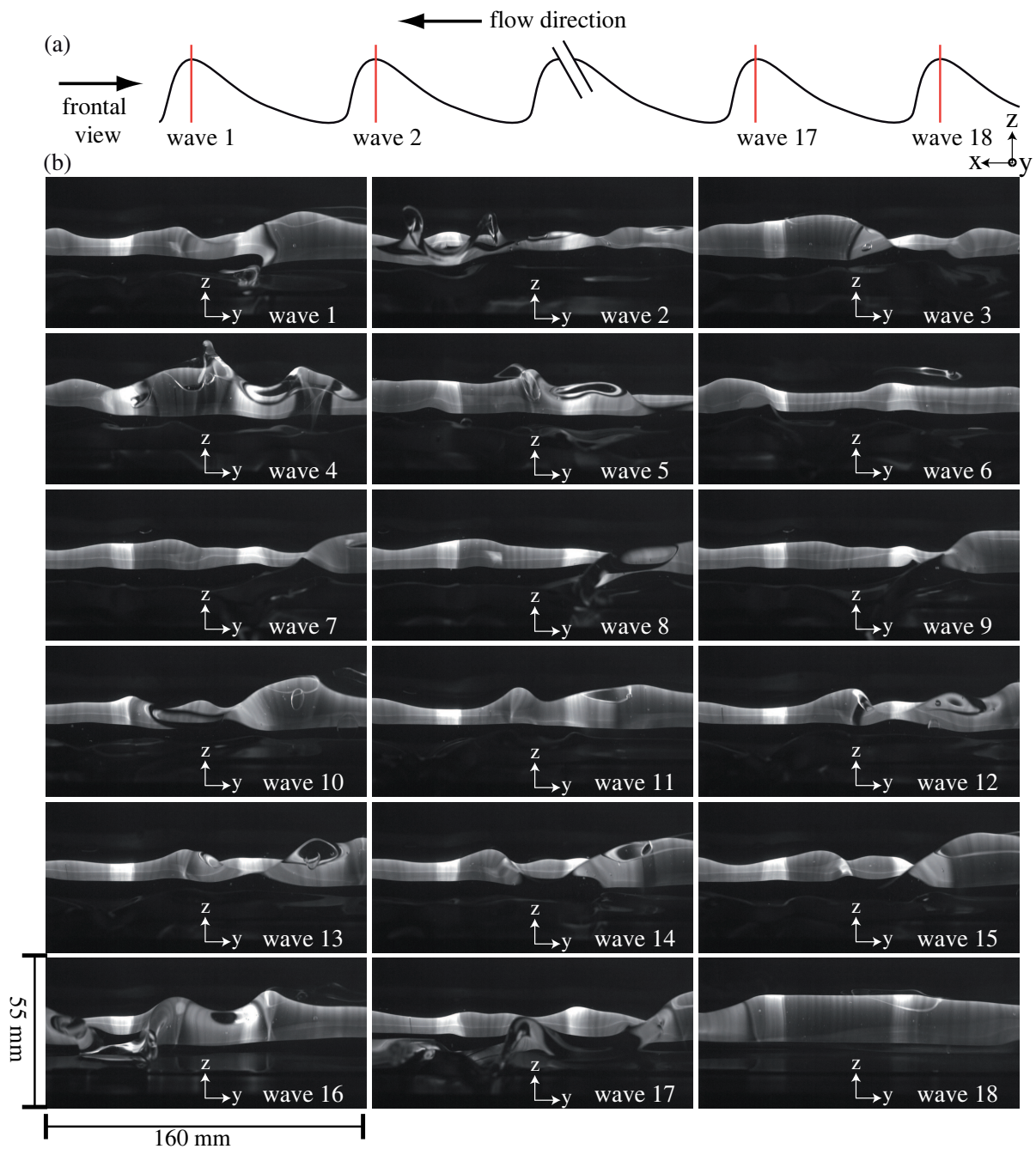


Figure 3.30.: Recordings at one position in the channel with a frontal view. (a) Idealized sketch of the waves measured with exemplary laser intersections indicated by red lines. (b) The pictures were taken from 18 different waves in a matching time delay for the excitation frequency; hence, all pictures represent the same position inside a wave for different waves. The waves were taken of a flow over a substrate with $W/L = 10/30$, $\alpha = 14^\circ$ and $Re = 16$. Modified and reprinted with permission from Dauth and Aksel [144]. © Springer Nature.

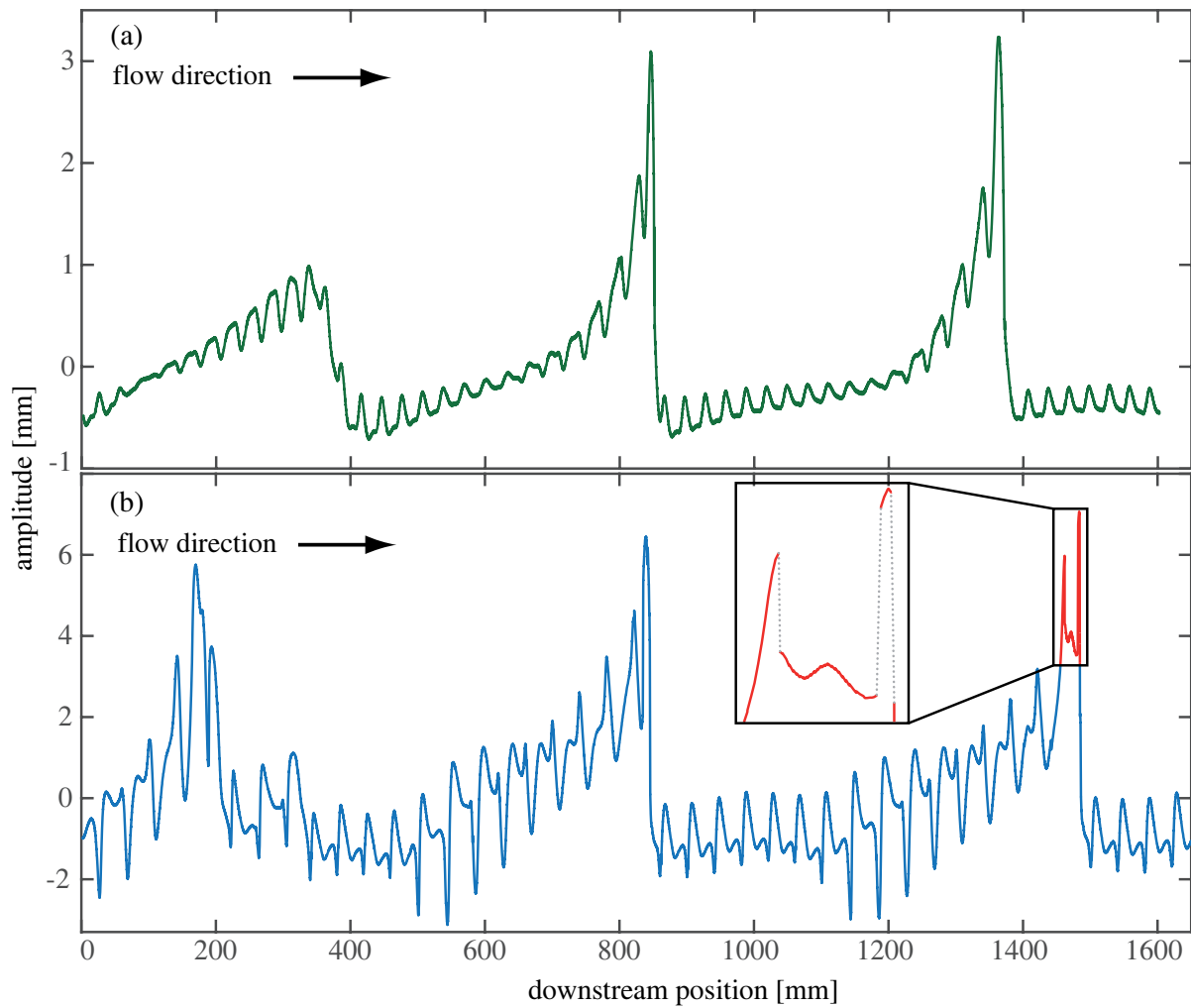


Figure 3.31.: Evolution of continuous waves with $f_e = 1.0$ Hz for: (a) $W/L = 20/10$, $\alpha = 10^\circ$ and $Re = 16$. (b) $W/L = 20/20$, $\alpha = 15^\circ$ and $Re = 16$. The inlay shows the problematic recombination area. The dotted lines highlight the failure of the combination process. Modified and reprinted with permission from Dauth and Aksel [144]. © Springer Nature.

Compared to the wave plotted in Figure 3.31 (a), the wave in Figure 3.31 (b) only shows the smooth wave shape in the beginning of the measurement distance. The wave is traveling over the substrate with $W/L = 20/20$ with an inclination $\alpha = 15^\circ$ and $Re = 16$. For this configuration, the irregular wave front is visible. The dents are larger compared to graph (a) because the undulation of the steady state free surface is more pronounced due to the higher inclination angle and the longer trough of the bottom contour. Until the downstream position $x = 1400$ mm in this plot, the cross-correlation works fine. Then, the region of the chaotic wave front of the traveling wave meaning the irregularity begins. At the wave front the cross-correlation cannot connect adjacent units properly. The area in which the cross-correlation is not working properly is marked in red in Figure 3.31 (b). The problematic area is enlarged in the inlay. The yielded surface of the wave has jumps in the front area. The jumps are highlighted by the gray dotted lines in the inlay. The red line in the inlay consists of about 2000 measurement points in contrast to the gray dotted lines (0 measurement points) which are just included to understand the problematic cross-correlation. Since the measurement was performed with

200 fps and recorded 1200 images, the cross-correlation has five waves to recombine but cannot find a proper match. In a nutshell, the wave fronts at this position are not repetitive and hence the waves show a chaotic/turbulent character. From now on, the terms chaotic and turbulent behavior are used for an irregular, non-repetitive and disordered appearance of the wave front in this Section 3.3. Chaotic and turbulent are used as synonyms in this context.

3.3.5. Screening different phenomena

The view of waves from above is shown in Figure 3.32. In the pictures, the prominent features are marked. The column (a) in Figure 3.32 shows the evolution of the fingering of the wave front. For the sake of clarity, the fingering is highlighted in red. The time difference between two adjacent photographs in column (a) is $\Delta t = 3/100$ s. The fingering is developing from a short streak into a long streak with a droplet at its tip. The streak narrows but lengthens/stretches as the wave strides forward. Since the measured length for this pictures was limited to 182 mm, it is not possible to see how the fingering ends. This kind of filament was not seen for regular waves which broke. Hence, the fingering is just a feature of the chaotic wave [143]. The air encapsulations visible in all pictures in Figure 3.32 are a result of the chaotic breaking of the waves into the troughs of the bottom undulation.

In the column (b) in Figure 3.32, two fingerings are visible at the beginning (marked with green) and these short fingers are splashing into the steady flow with a time lag. Small circles are forming around the impact area of the splashes similar to the rings forming on water when a droplet hits the surface. Yet the rings cannot spread out properly since the traveling wave overtakes and overlaps these circles. These areas are highlighted with green surroundings.

Another phenomenon is visible in the column (c) in Figure 3.32. At first, a finger from the wave front spreads out, but the filament raptures and results in a pinch-off. The form of the pinch-off is a mixture between a streak and droplet formation. In the second picture, the wave-side part of the fingering is marked in red and the pinched-off part is marked in blue and circled for the sake of lucidity. These drop formation and pinch-offs are extensively investigated for different systems by Eggers [153].

3.3.6. The magnitude of chaotic behavior

In Figure 3.33, the impact of the increase in the inertia is visible. By increasing the inclination angle from $\alpha = 12^\circ$ to $\alpha = 25^\circ$ at fixed $Re = 18$, the area of the chaotic part of the wave increases from a small portion of the image to the whole image with the length of 182 mm, see Figure 3.33 (a). A similar result was found for an increase of the Reynolds number from $Re = 12$ to $Re = 18$ at fixed $\alpha = 25^\circ$, yet the change is not as drastic as the change for the variation of the inclination angle since the magnitude of the change of the inertia is smaller, see Figure 3.33 (b).

In Figure 3.33 (c), the evolution of the wave is shown along the whole channel length. The recording was taken from a measurement with $Re = 18$, $\alpha = 25^\circ$ and $W/L = 10/30$. As visible, the chaotic region of the waves increases on its way downstream, indicated by the red lines marking the beginning and end of the chaotic region for each wave.

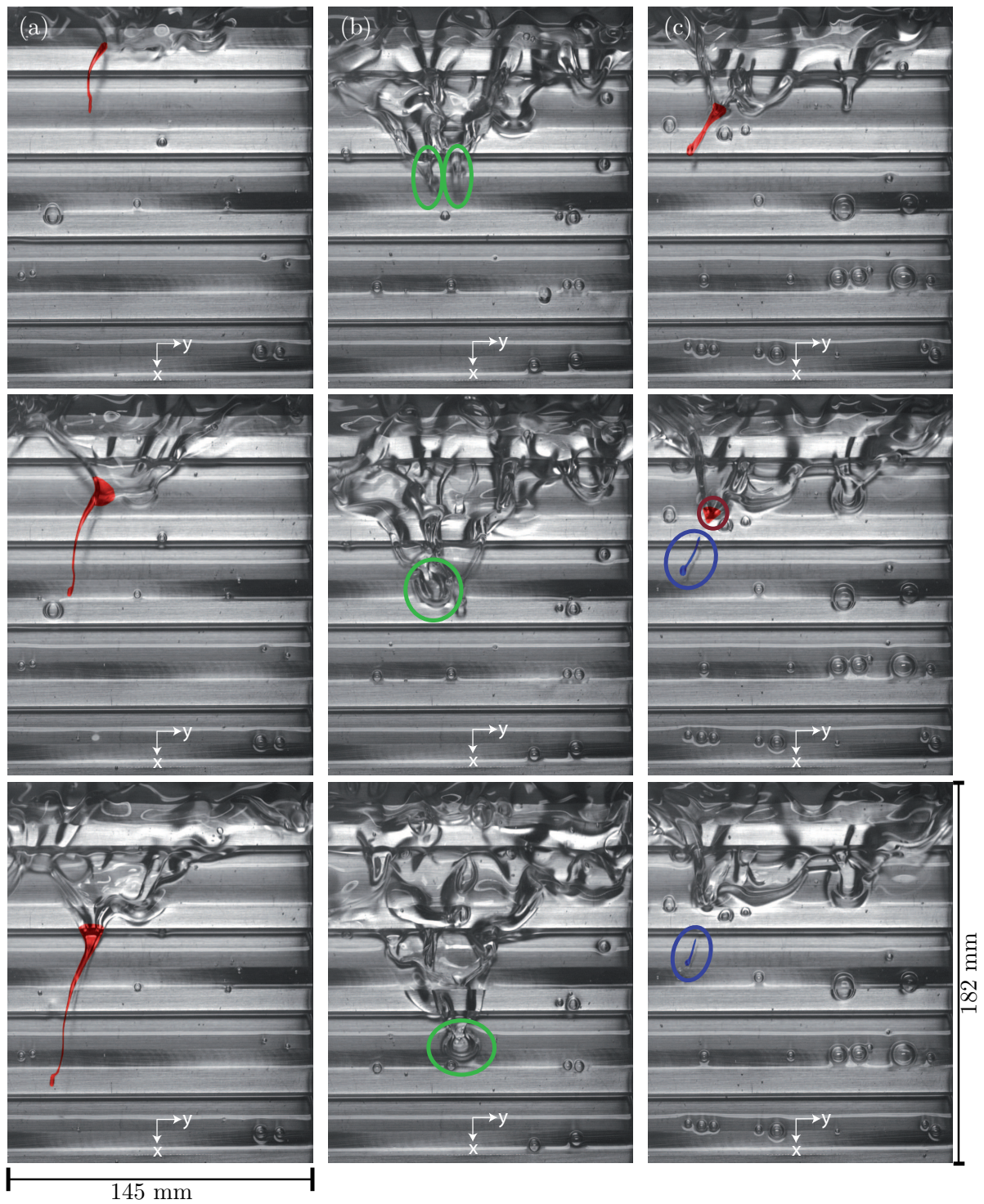


Figure 3.32.: Different phenomena highlighted in different colors. The measurements were performed on the $W/L = 10/30$ substrate with $\alpha = 25^\circ$ and $Re = 14$ [for (a) and (b)] or $Re = 16$ [for (c)]. (a) Fingering extending from the wave front. (b) Fingering splashing into the “steady flow” in front of the wave front. (c) Pinch-off with a mixture of streak and droplet formation. Modified and reprinted with permission from Dauth and Aksel [144]. © Springer Nature.

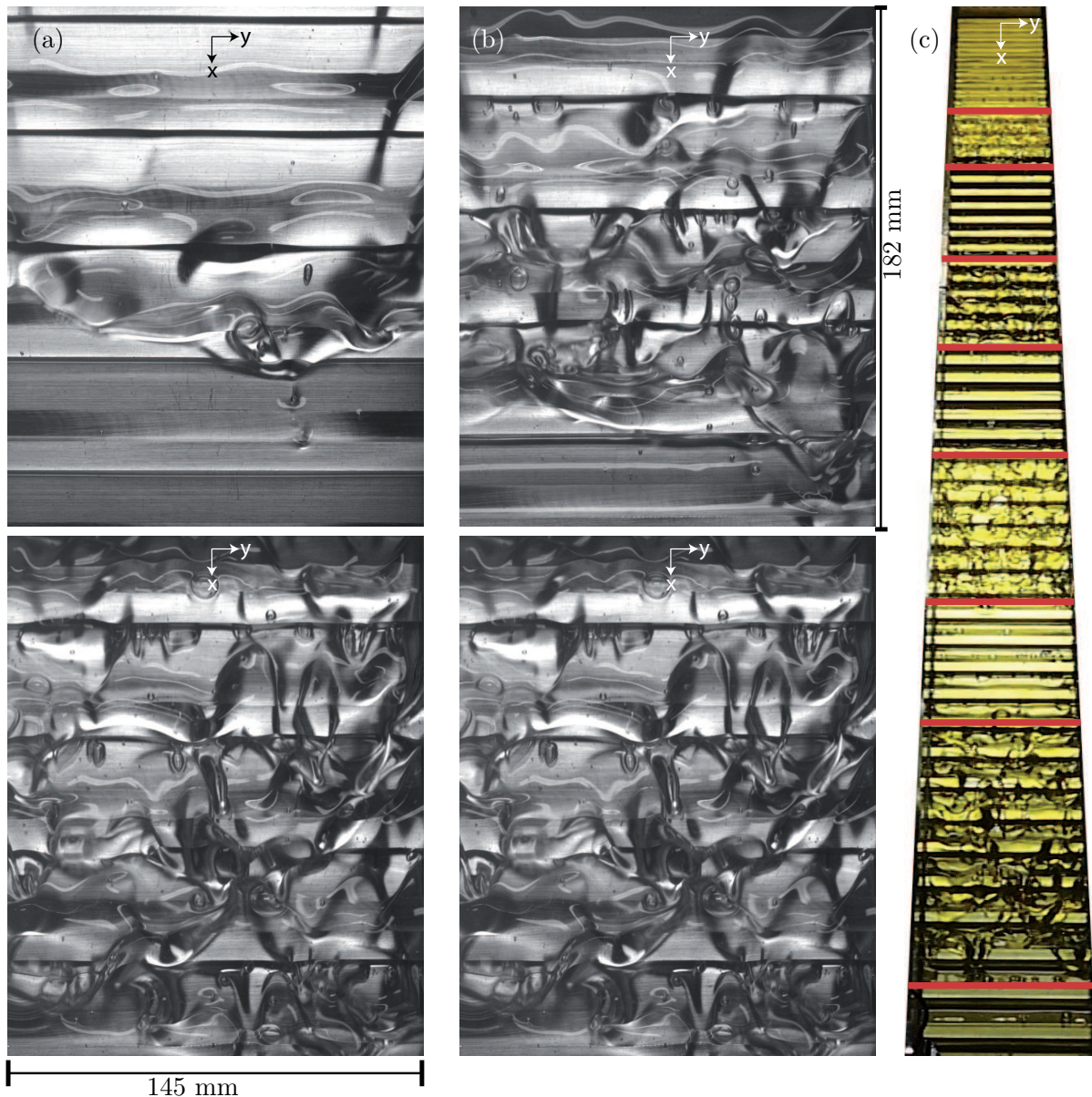


Figure 3.33.: Inspection of the chaotic area for various measurement settings on the substrate with $W/L = 10/30$. (a) Top: $Re = 18$ and $\alpha = 12^\circ$; Bottom: $Re = 18$ and $\alpha = 25^\circ$. (b) Top: $Re = 12$ and $\alpha = 25^\circ$; Bottom: $Re = 18$ and $\alpha = 25^\circ$. (c) The evolution of the chaotic area (surrounded by red marks) on the way downstream. The inertia was set to $Re = 18$ and $\alpha = 25^\circ$. Modified and reprinted with permission from Dauth and Aksel [144]. © Springer Nature.

3.3.7. The pathway to chaos and conclusion

The scenario of flow configurations in gravity-driven films over topographies differs from that over flat inclines. In gravity-driven films over flat inclines, one cannot distinguish between a creeping and inertial flow by inspection of the parabolic flow field. In contrast to that, the velocity profile (flow field) and the free surface of the gravity-driven films over topographies change with the transition from the creeping to inertial flow. In the next transition from the inertial steady flow to the traveling wave configuration, the (linear) stability charts of the

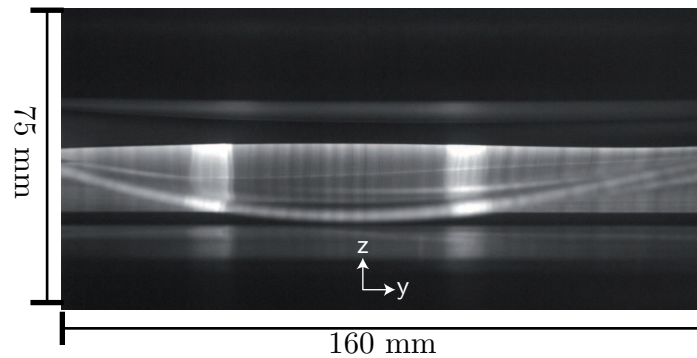


Figure 3.34.: The frontal view on a wave front of a wave flowing over a flat substrate with the inclination angle $\alpha = 30^\circ$ and $Re = 18$. Modified and reprinted with permission from Dauth and Aksel [144]. © Springer Nature.

gravity-driven films show various phenomena different from the classical transition on the flat incline [100].

Excitations above the neutral curve for any substrate provoke linear waves to develop. Higher excitations induce nonlinear waves which can show saturation, single wave breaking and multiple wave breaking [143]. Irrespective of the type, all wave configurations break at reaching sufficiently high inertia depending on the substrate. This regular wave breaking is indicated by one bubble creation over the whole channel width and subsequent contraction in the middle of the channel. It is at hand to speculate that the wave breaking acts as a precursor for the generation of chaotic wave fronts, which is shown in the following.

Dauth and Aksel [143] postulated that for breaking of waves over gravity-driven viscous films it is necessary that the bottom slope is corrugated with some protruding, prominent, sufficiently high peaks as obstacles which provoke corresponding peaks on the free surface of the steady film flow. The traveling waves surfing over this undulated free surface of the steady film stumble over these peaks and break. This chain of highly nonlinear, geometrical, and dynamic triple interaction of “the substrate – the steady state free surface – the traveling wave” is the necessary cause to effect paradigm of breaking of waves over gravity-driven viscous thin films.

This postulation was probed by using a flat substrate for the maximal inertia reached in the measurement system. With the postulation by Dauth and Aksel, no chaotic wave should be found as the necessary obstacles are not present. In Figure 3.34, the wave front for the flat substrate with $Re = 18$ and $\alpha = 30^\circ$ is shown. As visible, the wave front looks smooth and does not show any indication for chaotic behavior. In contrast, far below this inertia all undulated substrates probed for this study showed the chaotic character.

In the experiments the transition from the regular to the chaotic character of the wave fronts was analyzed in more detail. In the beginning, a wave breaking is observed, which is indicated by the bubble formation and necessary as a precursor for the chaotic behavior. After the first wave breaking further breakings occur, leading to the characteristic chaotic wave front and multiple air encapsulations. These wave breakings are not comparable to the first one since they do not break over the whole channel width. The quantity of the bubbles increases after the first wave breaking. Please, see the video in the supplementary material of publication [144] and Figures A.2 and A.3 in the appendix.

In a nutshell, from the regular wave front further wave fronts branch. This process repeats itself “indefinitely” until the system is in a turbulent state. The orderless bubble creation at the wave front supports this hypothesis of turbulent wave breaking. The experimental findings on the

transition to turbulence is in line with the Landau theory for the transition to turbulence [138]. The Landau theory states that the system reaches a turbulent state via multiple bifurcations as described in Section 1.4. In the present case, the transition to turbulence occurs with wave breaking as a necessary precursor. The wave breaking acts as a bifurcation. New stable and unstable waves emerge from the collapse of the waves. After numerous wave breakings, the state of turbulence is reached.

A schematic response diagram for the Landau theory, applied to the transition to turbulence for the present case, is displayed in Figure 3.35. The lines in the upper diagram do not represent specific states but only illustrate schematically the bifurcation mechanisms. In the beginning, for a small Reynolds number, a steady flow is at hand ($Re < Re^*$). With increasing the driving parameter (Re) above a certain threshold ($Re^* < Re < Re^{**}$), waves emerge with a regular wave front. In the next step ($Re^{**} < Re < Re^{***}$), the regular flow is still present with single or multiple wave breaking. These features were discussed by Dauth and Aksel [143] and a video of a single wave breaking is available in the supplementary material of the publication [143]. Further increase of the driving parameter leads to more bifurcations in terms of wave breakings. After many such bifurcations ($Re > Re^{***}$), irregular wave fronts with chaotic wave breakings are reached. This flow with turbulent wave fronts was discussed in the present work and a movie of the transition is available as supplementary material of publication [144]. In the lower part of Figure 3.35, characteristic exemplary diagrams are plotted. For $Re^* < Re < Re^{**}$, the amplitude evolution of a wave with normal saturation is displayed. In case of $Re^{**} < Re < Re^{***}$, the amplitude evolution of a wave with single wave breaking is shown.

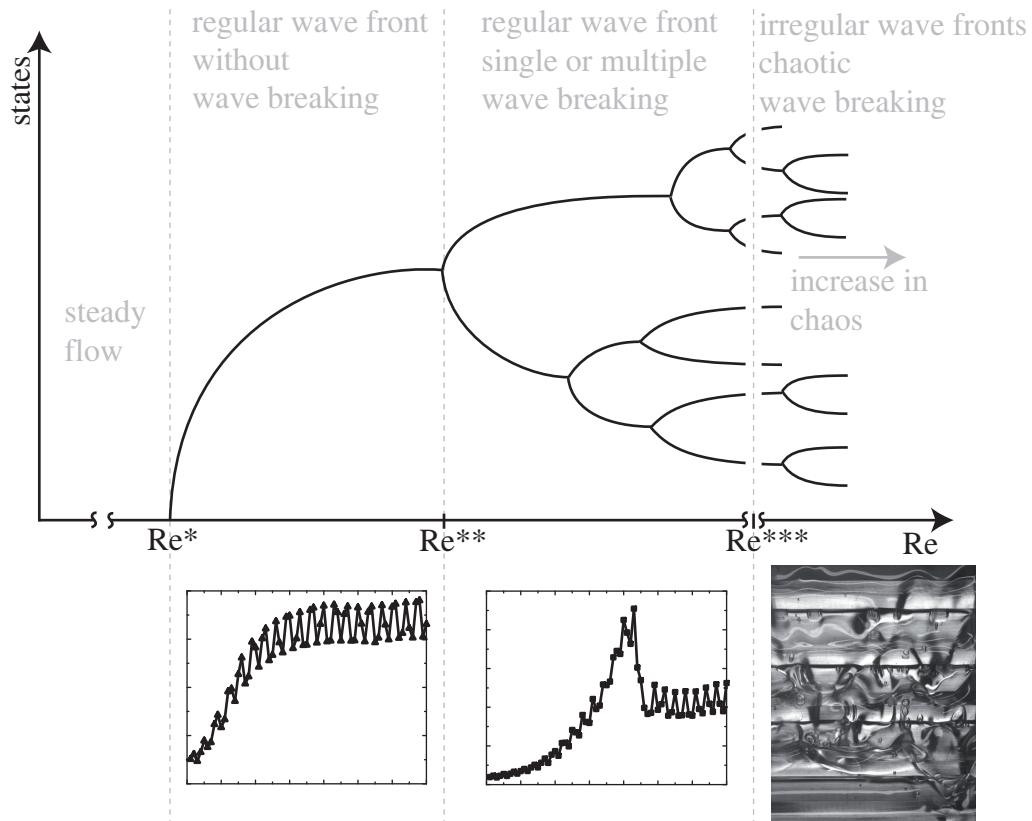


Figure 3.35.: Schematic response diagram for transition to turbulence. In the case of the regular wave fronts ($Re^* < Re < Re^{**}$) the bifurcations symbolize emerging and collapsing (breaking) waves. The quantity of these bifurcations increases with the Reynolds number (measure for the inertia). After many such bifurcations ($Re > Re^{**}$) irregular wave fronts emerge and further bifurcations in form of chaotic wave breaking result. In the lower part characteristic diagrams are plotted. For $Re^* < Re < Re^{**}$, the amplitude versus the downstream position is displayed. For $Re > Re^{**}$, a picture of a turbulent wave front is presented. Modified and reprinted with permission from Dauth and Aksel [144]. © Springer Nature.

3.4. Thoughts on surface turbulence on film flows

In the previous Section 3.3, the transition from regular to turbulent wave fronts in films over topography was discussed and shown. The turbulent area was localized only at the wave front. Hence, the wave tail exhibited a regular smooth shape. The transition to the turbulent wave front was said to be in line with the theory of the transition to turbulence by Landau. In Section 1.4 another transition to turbulence was discussed: The spontaneous transition to a comprehensive surface turbulence. This kind of behavior was also measured in the framework of this dissertation. The resulting surface turbulence of a flow over a sinusoidal substrate is shown in Figure 3.36 (a). For the sake of comparison, the localized turbulent wave fronts above a rectangular bottom profile are plotted next to it in Figure 3.36 (b). In Figure 3.36 (a), the surface is twofold and the segregation is marked with a red line. First, the excited wave travels down the smooth free surface. Second, the wave vanishes under the developed surface turbulence. Starting from the point where the surface turbulence emerges first, it covers the whole surface of the flow. A similar behavior is observable for the steady flow without any impressed disturbances. This phenomenon is only visible for a sufficiently high inertia which is determined by the inclination angle α and the Reynolds number Re . In the case of Figure 3.36 (a), the inclination angle was set to $\alpha = 30^\circ$ and $Re = 18$. The steady state becomes unstable and breaks into a three-dimensional flow. However, the transition to turbulence was never discussed and it was assumed to be spontaneous similar to the classical idea in pipe flows, as discussed in Section 1.4.

The surface turbulence features an irregular appearance without any air encapsulations, splashes, pinch-offs, etc. which are visible for the wave front turbulence. The lack of air encapsulations hints that there is no wave breaking present in the systems. Hence, the necessary trigger for the bifurcation is not present in the system. This leads to the conclusion that the transition to surface turbulence is spontaneous. In Section 3.2, it was shown that protruding, sufficiently high peaks as obstacles are required as stumbling stones for the wave breaking. In the case of the sinusoidal substrate the undulation is not functioning as a stumbling stone since the undulation is too smooth. The lack of stumbling stones explains the missing appearance of turbulent wave fronts for a lower inertia.

In Figure 3.36 (b), the area of the turbulent wave front increases on its way downstream and therefore the regular wave tail shrinks. This raises the question if subsequent turbulent wave fronts can merge if the inertia is sufficiently high. If the waves merge and a comprehensive turbulent flow is reached, will the turbulence differ from the comprehensive turbulence as displayed in Figure 3.36 (a)? Can the phenomena induced by the chaotic wave breaking like splashes, fingering, pinch-offs, and orderless bubble creation still emerge although the wave front cannot evolve freely due to the comprehensive turbulence?

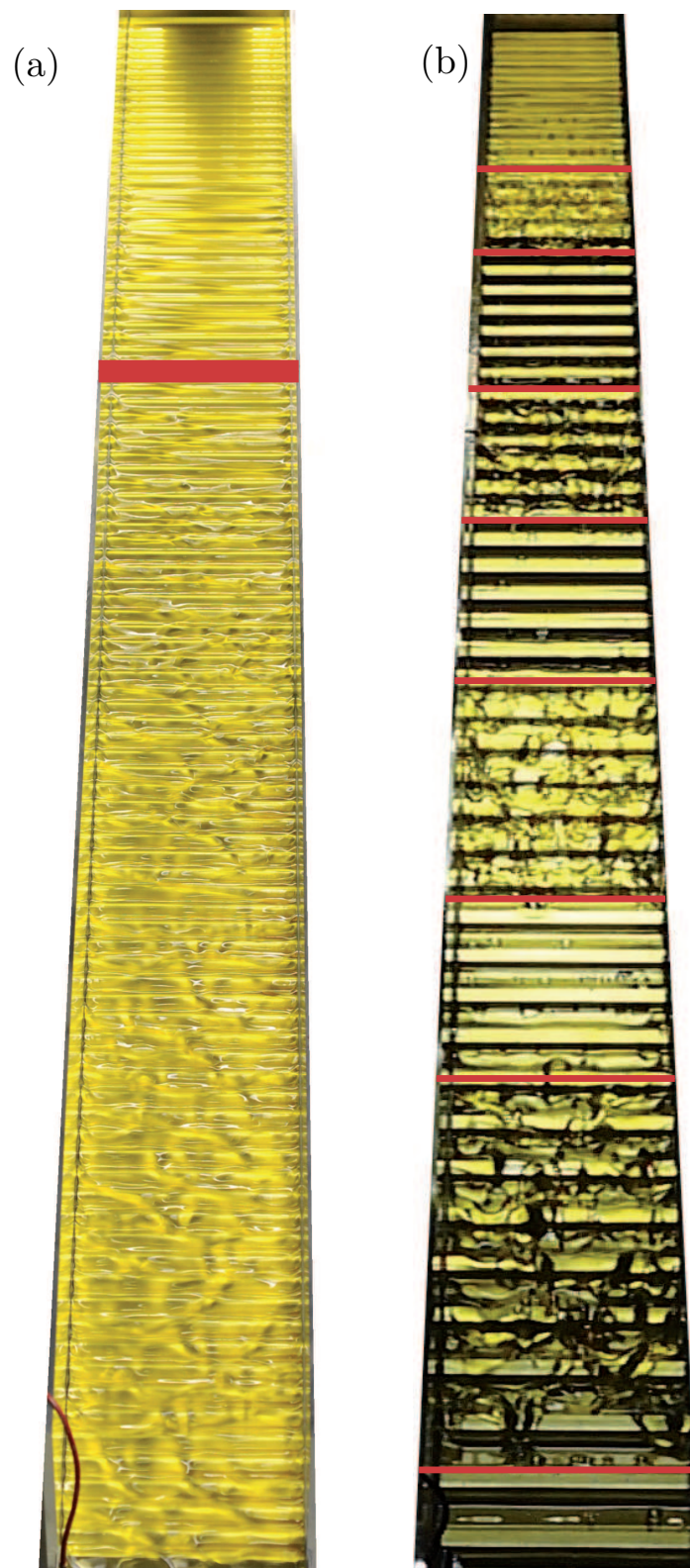


Figure 3.36.: Comparison of different turbulent flows. (a) Flow over a sinusoidal substrate with a comprehensive surface turbulence. (b) Flow over a rectangular substrate with irregular wave fronts.

4. Conclusions and outlook

The aim of this dissertation was to investigate all evolutionary steps of free surface waves traveling on a gravity-driven thin film flow. Extensive experiments with a wide range of measurement techniques were combined to unveil and characterize features of the traveling waves. Thereby, the main focus lay on the influence of periodic, one-dimensional topographies on the evolution of traveling waves. These waves surfed on a two-dimensional Newtonian film flow which was solely driven by gravity. Another crucial factor in the analysis was the inertia in form of the Reynolds number and the inclination angle.

The evolutionary steps begin with the excitation of vanishingly small waves. These waves are in the linear limit and give rise to stability measurements on traveling free surface waves. With the help of the measured stability charts it was possible to generate convectively unstable waves for further experiments. Although the stability behavior of linear and nonlinear waves differs slightly, the stability measurements are a good reference point for the evolution of nonlinear waves, which are the main topic of this work.

Sinusoidal waves in the linear regime are generated and do not change their shape on the way downstream, as long as they remain within the linear limit. In contrast to linear waves, nonlinear waves change their shape even though a sinusoidal wave is generated. Two distinct wave shapes were observed in the framework of the dissertation. First, the classical concave wave shape which is already well-known from a flow over a flat substrate. Second, a convex wave shape is observed for flows over strongly undulated substrates. Besides an energy transfer from the basic excitation frequency to higher harmonics, which is observable for both wave shapes, beat frequencies are visible in the Fourier spectrum for all undulated substrates. These beat frequencies represent the interaction of the “standing” geometrical substrate wave and the traveling wave. The interaction strength differs strongly for the two distinct wave shapes and substrate shapes, respectively. For strongly undulated substrates, the amplitudes of the beat peaks in the Fourier space are much more pronounced than in the case of weakly undulated substrates. Waves over the weakly undulated topographies show the classical concave wave shape. Consequently, the assumption of an interaction induced transition to a convex wave shape seems likely. To fortify this assumption, particle tracking measurements were conducted. The penetration depth of the traveling free surface wave into the steady state flow strongly depends on the substrate’s shape and wavelength. Concluding, the curvature of the steady state free surface, which is provoked by the substrate’s shape, is decisive for the wave’s shape. Yet, the exact substrate shape plays only a secondary role. An effective substrate shape dictates the shape of the steady state free surface and hence the curvature of the traveling wave.

A gedankenexperiment on the influence of the steady state free surface on the wave’s shape triggered new experiments. Increasing the inertia of the system through the Reynolds number and inclination angle leads to two contrary effects on the steady state free surface. First, the increase in the Reynolds number leads to a larger film thickness, which flattens the steady state free surface and decreases the mean or global curvature. Second, the increase of the inclination angle leads to a thinner film, which pronounces the steady state free surface and therefore increases the mean or global curvature. In contrast to these contrary trends, the

increase of both parameters leads to a higher growth rate of waves if the classical Nusselt case is considered.

In the course of increasing the Reynolds number, new unseen phenomena for film flows have been uncovered. These phenomena concern the evolution of the amplitude of the traveling waves for which three possible ways were observed. In the beginning, all types have an exponential growth in common but differ strongly later on. Besides the classical saturation of the traveling waves, two wave breaking mechanisms have been found. On the one hand, the wave grows exponentially until the wave is in an unstable state with a large amplitude and breaks. After the wave breaking a new wave emerges with a smaller amplitude and then saturates. Here, the saturation amplitude is much smaller than the maximal amplitude just before the wave breaking. On the other hand, the wave cannot find an equilibrium state (saturation) after the wave breaking but grows and breaks alternately. These two evolutionary behaviors were denoted as single or multiple wave breaking.

Both wave breaking mechanisms lead to a collapse of the unstable waves into the troughs of the steady state free surface. Thereby, the wave flattens the undulation of the steady state free surface and a new wave emerges, which was shown with a baby jet firing out of the upper flow boundary. Subsequently, the newly generated wave can either saturate or grow and re-break. Irrespective of the further evolution of the new wave, the wave breaking brings a bubble creation with it. An air encapsulation over the whole channel width is induced by the plunging of the wave into the underlying flow. This broad inclusion contracts to an energetically favorable state in form of a bubble, which rises to the top of the flow.

The selection of the three evolutionary types of the wave strongly depends on the topography's shape and wavelength and the subsequent steady state free surface. In the case of a strong global or mean curvature of the steady state free surface, the traveling waves show wave breaking – an only locally strong curved steady state is not sufficient for this mechanism. In a nutshell, for breaking of waves over gravity-driven viscous films it is necessary that the bottom slope is corrugated with some protruding, prominent, sufficiently high peaks as obstacles which provoke corresponding peaks on the free surface of the steady film flow. The traveling waves surfing over this undulated free surface of the steady film stumble over these peaks and break. This chain of highly nonlinear, geometrical, and dynamic triple interaction of “the substrate – the steady state free surface – the traveling wave” is the necessary cause to effect paradigm of breaking of waves over gravity-driven viscous thin films.

In the course of increasing the inclination angle with a varying Reynolds number, turbulent wave fronts were discovered for flows over strongly undulated substrates. This kind of turbulence is only limited to the wave front, so a coexistence of a regular wave tail and a turbulent wave front is present. The areas of the coexistent regimes can be tuned by the inertia in the system. In this context turbulent refers to a non-repetitive, irregular and disordered appearance. The shape of the wave front changed from the classical parabolic shape (for the center of the channel flow) to a completely disordered and unpredictable shape. Furthermore, multiple orderless bubble creations along the whole channel length hint at a chaotic wave breaking. In addition to the chaotic wave breaking, new features were seen, e.g., fingering, splashes, and pinch-offs.

The novel finding of a subdivision of the wave in a turbulent and regular part triggers the question about the actual pathway to a turbulent state. By raising this question, the necessity of a precursor in form of wave breaking was found. Having seen that, a similarity to the Landau theory of the transition to turbulence is likely. In the present case, the wave reaches the turbulent wave front via a series of wave breakings. The requirement of wave breaking to reach the turbulent wave fronts leads to the conclusion that this turbulent state can only be

reached for flows over anharmonic, strongly undulated substrates.

This conclusion was challenged by measurements on a flow over a harmonic sinusoidal substrate. Thereby, a wide range of inclination angles and Reynolds numbers were tested and the turbulent wave fronts have not been found. Nevertheless, a comprehensive turbulence of the whole flow beyond a specific point was observed, which differs strongly from the wave front turbulence. Irrespective of external forcing this turbulence was detected. Since the flow has a regular appearance before this specific point, the transition is unclear. Due to the sudden change from regular to turbulent, a spontaneous transition seems likely. However, this assumption has to be tested in further experiments.

To summarize, this work deals with the impact of corrugated topographies on the evolution of traveling free surface waves on a film flow. The shape of the steady state free surface, which is provoked by an effective substrate, is decisive for the evolution of the traveling waves in all evolutionary steps. Although a wide range of experiments was conducted, various open questions remain. Are there any other evolutionary steps of the waves for a flow over weak or strong undulated topographies? Is the transition to the comprehensive turbulence for smooth undulations really spontaneous? How will the turbulent wave fronts develop if the inertia is increased? These questions have to be answered in further experiments. However, the discrete steps and the multiplicity of experimental parameters impedes the complete scanning of the large domain of influencing parameters. Thus, a numerical study of the full Navier-Stokes equations would be eminent. But, the complexity of modeling rectangular substrates and strong nonlinear interactions make the computational effort immense. As a final remark, the author wants to emphasize that the new findings of a convex wave shape, the wave breaking mechanisms, and the turbulent wave fronts for flows over strong undulations shed light on many aspects regarding the evolution of traveling free surface waves, which paves the way for further studies on this topic. Thereby, the results provide valuable information for the design of optimized topography for specific applications.

A. Appendix

A.1. Emergence of the bubble while wave breaking



Figure A.1.: Enlarged picture of the bubble generated by wave breaking. See Figure 3.22 for comparison. Modified and reprinted with permission from Dauth and Aksel [143]. © AIP Publishing.

A.2. Transition of a regular to irregular wave front

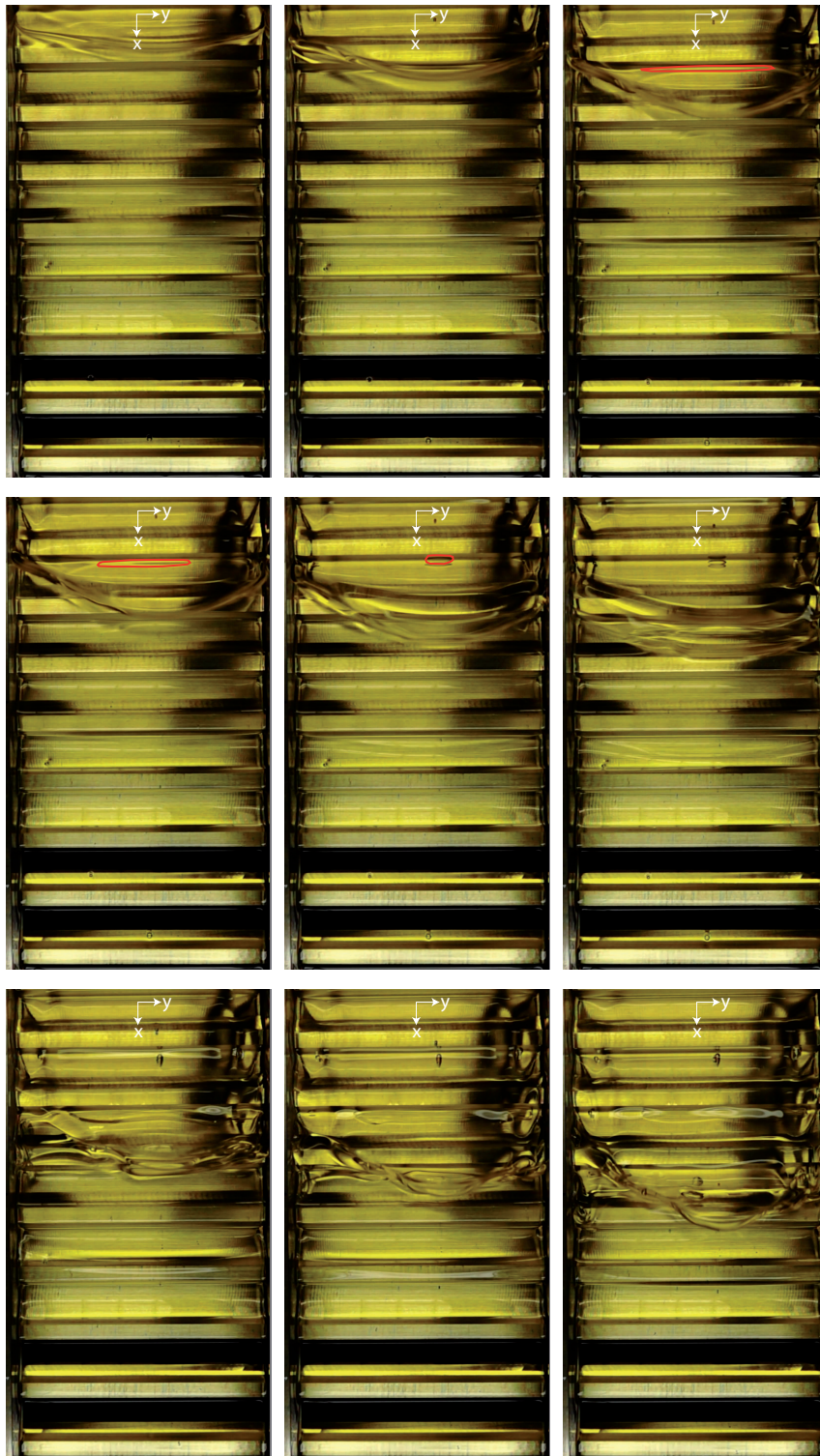


Figure A.2.: The transition of a regular to irregular wave front with the intermediate step of wave breaking. The bubble of the regular wave breaking mechanism is circled in red for the sake of lucidity.

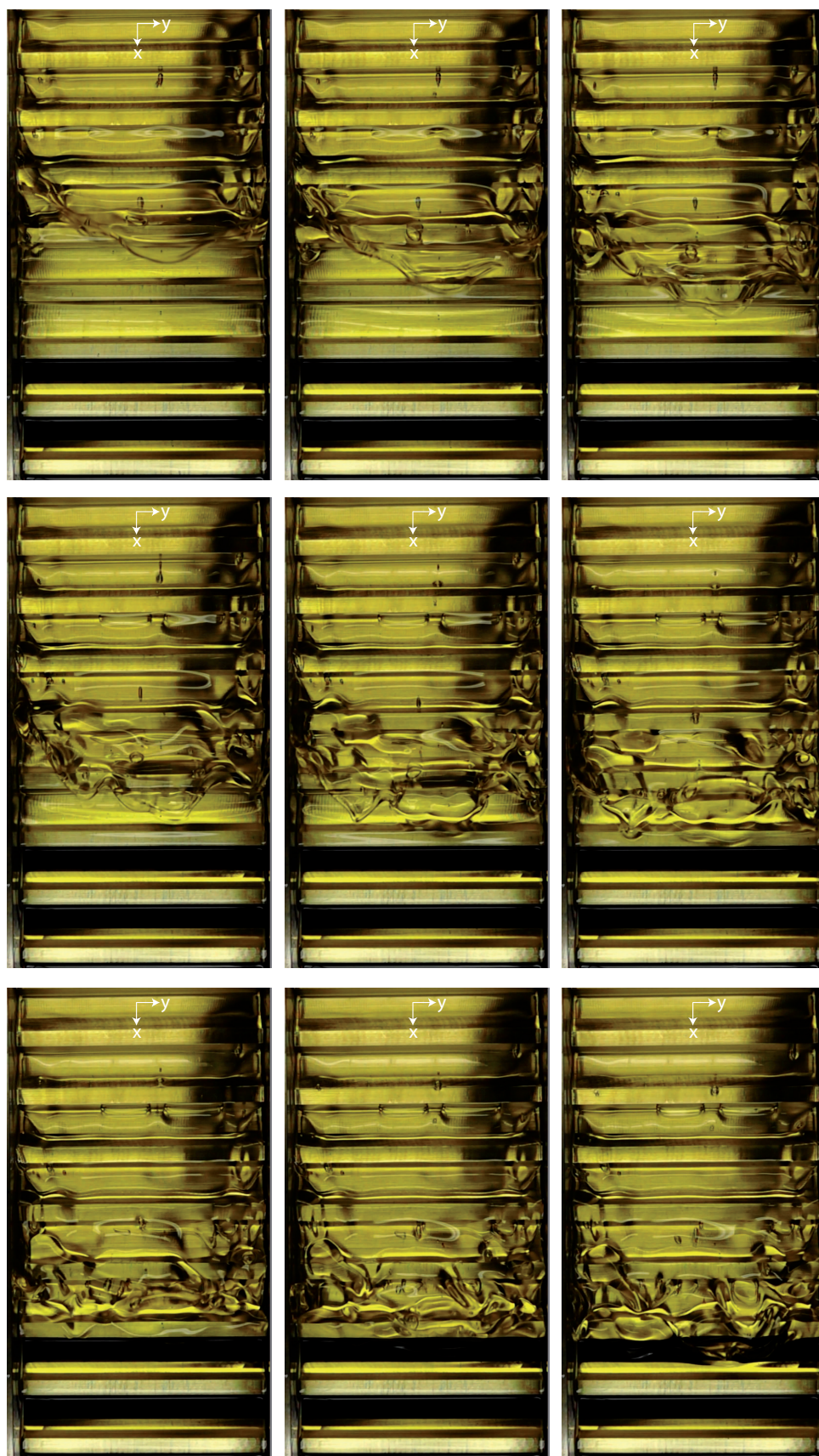


Figure A.3.: The prosecution of the transition of a regular to irregular wave front in Figure A.2.

List of Symbols

symbol (unit)	description	page list
α ($^\circ$)	Inclination angle of the channel	15, 19–21, 23, 27, 31, 34, 49, 56, 61, 62, 64, 66, 67, 73
β ($^\circ$)	Inclination angle of the lasers used for the stability measurements	26
η (Pas)	Dynamic viscosity	21, 22, 87
λ_b (m)	Wavelength of the substrate	20, 21, 34–39, 41–47, 87, 88
λ_w (m)	Wavelength of the traveling free surface wave	26, 38, 41, 42
ν (m^2s^{-1})	Kinematic viscosity	21, 23
ϕ (rad)	Phase difference	29, 30
ρ (kgm^{-3})	Liquid density	21, 22, 87
ρ_p (kgm^{-3})	Particle density	22
σ (Nm^{-1})	Surface tension	21, 87
τ (s)	Phase difference	29, 30
θ ($^\circ\text{C}$)	Temperature	19–21, 34, 49, 62, 87, 90
ξ_d	Grade of dispersity	22
A (m)	Topography amplitude	20, 27, 31, 34, 39, 41, 42
A_e (m)	Paddle amplitude; excitation amplitude	20, 26, 34, 38, 42, 43, 45–47, 54
a_w (m)	Amplitude of the traveling free surface wave	26, 27, 38, 42
B_1 (a.u.)	Amplitude of the Gaussian fit of the main peak of $\hat{p}_1(f')$	27
B_2 (a.u.)	Amplitude of the Gaussian fit of the main peak of $\hat{p}_2(f')$	27
b_c (m)	Channel width; substrate width	19, 23, 26
B_i (a.u.)	Amplitude of the Gaussian fit of the main peak of $\hat{p}_i(f')$	27
ΔB (a.u.)	Measure for the difference of the free surface amplitudes of the traveling waves at the positions x_1 and x_2	27, 28
d_p (m)	Particle diameter	22
$d_{V,16}$ (m)	Particle size, which is greater than or equal to 16% of all particles	22
$d_{V,50}$ (m)	Median particle size	22

symbol (unit)	description	page list
$d_{V,84}$ (m)	Particle size, which is greater than or equal to 84% of all particles	22
$d_{V,j}$ (m)	Particle size, which is greater than or equal to $j\%$ of all particles	22
\vec{e}_x	Unity vector in x -direction	23
\mathcal{F}	Fast Fourier Transformation	29
f' (s^{-1})	Frequency	27
f_e (s^{-1})	Paddle frequency; excitation frequency	20, 26, 27, 29, 30, 33–35, 38–43, 45–47, 51, 53, 54, 57, 64, 87, 88
<i>Flat</i>	Flat topography shape	20, 33, 34, 41, 49, 62
g (ms^{-2})	Gravitational acceleration	21–23
h (m)	Time-dependent local film thickness	28, 30
h_0 (m)	Local film thickness of the steady-state flow; upper boundary of the steady-state flowing domain	23, 25, 28–30
h_c (m)	Continuous wave's shape	28–30, 64
h_i (m)	Time-dependent local film thickness for fragment i	29
h_n (m)	Nusselt film thickness	23, 34, 49, 62
\mathcal{I}	Imaginary part of a complex number	29
k_0 (m^{-1})	Wave number of the undulation	37
k_c (m^{-1})	Continuous wave's wave number	37
k_e (m^{-1})	Continuous wave's wave number of the excitation	35
k_s (m^{-1})	Wave number of the excitation and its higher harmonics	37
Ka	Kapitza number	21
L (m)	Length of the topography's bottom of the trench	20, 21, 27, 49, 51, 62
l_c (m)	Channel length	19
N_{frag}	Number of recorded fragments	29, 30
\mathbf{p}_i (m)	Position of the laser spot i	26
$\hat{\mathbf{p}}_i$ (m)	Fourier transformed laser spot position of the laser i	27
\hat{p}_i (m)	Absolute value of the Fourier transformed laser spot position of the laser i	27
$p_{x',i}$ (m)	The x' -position of the spot of laser i on the screen	26
$\hat{p}_{x',i}$ (m)	Fourier transformed x' -position of the spot of laser i	27
$p_{z',i}$ (m)	The z' -position of the spot of laser i on the screen	26, 27
$\hat{p}_{z',i}$ (m)	Fourier transformed z' -position of the spot of laser i	27
\dot{q} (m^2s^{-1})	Two-dimensional flow rate	23

symbol (unit)	description	page list
\mathcal{R}	Real part of a complex number	29
Re	Reynolds number	23, 27, 28, 34, 38, 39, 49, 61, 62, 64, 66, 67, 71, 73
Re_c	Critical Reynolds number	15
Rec	Rectangular topography shape	20, 27, 33, 34, 41, 49, 62
Saw	Sawtooth-like topography shape	20, 34, 41
$shape$	Specific shape of the topography	20, 49, 62
Sin	Sinusoidal topography shape	20, 34, 41
t (s)	Time	26–30, 51, 56
\vec{u} (ms ⁻¹)	Velocity vector	23
$u_{s,n}$ (ms ⁻¹)	Nusselt free surface velocity	23, 34, 49, 62
\dot{V} (m ³ s ⁻¹)	Three-dimensional volume flux	20, 22, 23, 26, 34, 49, 62, 87
W (m)	Length of the topography's top of the trench	20, 21, 27, 34, 35, 49, 51, 62, 87
W/L	Ratio of the length of the top of the trench to the bottom of the trench	25, 30, 31, 33, 51–59, 61, 64, 66, 67, 87, 88
w_{sed} (ms ⁻¹)	Sedimentation speed	22
x (m)	The x-coordinate	23, 25, 28–31, 51, 57, 66
x' (m)	The x'-coordinate of the reference frame of the screen	26, 27
x_1 (m)	x -position of laser 1	26
x_2 (m)	x -position of laser 2	26
x_c (m)	Image's size in x-direction	23, 28, 29, 64
x_i (m)	x -position of laser i	26
y (m)	The y-coordinate; distance to the channel's centerplane	23, 26, 30
z (m)	The z-coordinate	23, 25, 26, 30
z' (m)	The z'-coordinate of the reference frame of the screen	26, 27

List of Figures

1.1.	Schematic response diagram for Landau theory.	17
2.1.	Sketch of the flow facilities and the flow circuit	19
2.2.	The measured temperature θ for a five hour measurement.	20
2.3.	Geometry and notations of the viscous film flow over the different topographies	20
2.4.	The dynamic viscosity η , density ρ and surface tension σ for the <i>Elbesil</i> silicon oil blend.	21
2.5.	Tracer particle size distribution and photophysical properties of the dye	22
2.6.	The measured volume flux \dot{V} for a five hour measurement.	23
2.7.	Experimental setups for the measurements of the free surface shape of the steady film flow, the free surface shape of the perturbed film flow and the flow field structure of both steady and perturbed film flow	24
2.8.	Experimental setup for the steady flow and wave evolution/dynamics	24
2.9.	Exemplary image of the steady state flow over a rectangular substrate and the calibration plate	25
2.10.	Determination of the steady state free surface of the flow	25
2.11.	Experimental setup for the measurements of the convective instability	26
2.12.	Exemplary stability measurement	27
2.13.	The sketch shows a series of measurements over a sinusoidal substrate.	28
2.14.	Amplitude-time-curves and their Fourier Transformations at the same downstream position.	29
2.15.	An example of a free surface wave over a rectangular substrate with $W/L = 20/20$.	30
2.16.	Sketch of a part of a traveling free surface wave over an undulated substrate. .	31
2.17.	Exemplary image with tracer particles, overlaid with particle trajectories . . .	31
2.18.	Experimental setup for the wave screening	32
3.1.	Different curvatures for traveling free surface waves over a flat and a rectangular topography	33
3.2.	Linear stability maps for the rectangular substrates with $\lambda_b = \{0; 10; 20; 100; \infty\}$ mm with $W = 1$ mm	35
3.3.	Evolution and Fourier plots of waves over different rectangular substrates with $\lambda_b = \{0; 10; 20; 100; \infty\}$ mm with $f_e = 1.0$ Hz	36
3.4.	Comparison of the wavelength of the traveling wave with the wavelength of the substrate for various excitation frequencies f_e	37
3.5.	Evolution of traveling waves over the flat substrate for different excitation frequencies f_e	38
3.6.	Evolution of traveling waves over the rectangular substrate with $\lambda_b = 20$ mm for various excitation frequencies f_e	39
3.7.	Linear stability maps for the sinusoidal, sawtooth and rectangular substrates with $\lambda_b = 20$ mm	39

3.8. Evolution and Fourier plots of waves over various substrate shapes with the excitation frequencies $f_e = 1.0$ Hz	40
3.9. Comparison of how the wavelength of the traveling wave changes with the shape of the substrate for different excitation frequencies f_e	41
3.10. Dimensionless parameter plotted for various substrates	42
3.11. Variation of the free surface during one period of traveling nonlinear waves over three topographies	43
3.12. Replotted figures of Figures 3.11 (b), (e), (h). For more optical clarity only time steps $t = 0, T/4, T/2, 3T/4$ are shown	44
3.13. Particle tracking images for the flow over the rectangular substrate with $\lambda_b = 10$ mm	45
3.14. Particle tracking images for the flow over the rectangular substrate with $\lambda_b = 20$ mm	46
3.15. Particle tracking images for the flow over the sinusoidal substrate with $\lambda_b = 20$ mm	47
3.16. Sketch of the basic states: (a) steady state free surface for the film flow. (b) flat surface of rest for water waves	48
3.17. The steady state free surfaces for all substrates measured in this Section 3.2	50
3.18. Amplitude plot of traveling free surface waves over two different topographies with $W/L = 10/50$ and $W/L = 10/20$ with the excitation frequency $f_e = 1.2$ Hz	50
3.19. Time evolution of one traveling wave with $f_e = 1.0$ Hz over the substrate with $W/L = 20/20$ for four different time steps for a small excerpt of the whole measurement distance	51
3.20. Amplitude plots for four exemplary measured substrates for different excitation frequencies	52
3.21. Amplitude plots for $f_e = 1.4$ Hz over different substrates	54
3.22. Observation of wave breaking and bubble creation with the amplitude time evolution and view from above	55
3.23. The raw data of the traveling wave over the substrate with $W/L = 20/20$ with the excitation frequency $f_e = 1.0$ Hz recorded with a frame rate of 500 fps	56
3.24. Time evolution of the traveling wave with $f_e = 1.0$ Hz over one time period in $T/4$ steps	57
3.25. Wave number Fourier spectra for two different substrates $W/L = 20/10$ with saturation and $W/L = 20/20$ with single wave breaking	58
3.26. Raw images of the steady state free surface and a wave falling into the trough with a jet emerging	58
3.27. The derivatives of the steady state free surfaces for all substrates measured in Section 3.2	60
3.28. Recorded images from the frontal view of the beginning of waves over the substrate with $W/L = 10/30$ and $Re = 16$ for different inclination angles	61
3.29. The time evolution at one position in the channel recorded with a frontal view	63
3.30. Recordings at one position in the channel with a frontal view	65
3.31. Evolution of continuous waves over different substrates	66
3.32. Different phenomena of irregular wave fronts are displayed	68
3.33. Inspection of the chaotic area for various values of the inertia	69
3.34. The frontal view on a wave front of a wave flowing over a flat substrate	70
3.35. Schematic response diagram for transition to turbulence	72
3.36. Comparison of different turbulent flows	74

A.1. Enlarged picture of the bubble generated by wave breaking	79
A.2. The transition of a regular to irregular wave front with the intermediate step of wave breaking	80
A.3. The prosecution of the transition of a regular to irregular wave front in Figure A.2	81

List of Tables

2.1.	Liquid properties and Kapitza number of the <i>Elbesil</i> silicon oil blend used in the experiments at the measurement temperature $\theta = (23.0 \pm 0.1)^\circ\text{C}$	21
3.1.	The list of all substrate combinations used for measurements.	49
3.2.	List of all substrates and the categorization for the three phenomena (saturation, single wave breaking and multiple wave breaking).	53
3.3.	The list of all substrate combinations used for measurements.	62
3.4.	The list of all volume fluxes and Reynolds numbers used for measurements and the resulting flow parameter for the inclination angles 10° and 30°	62

References

- [1] Luca, I., Hutter, K., Tai, Y. C., Kuo, C. Y.: A hierarchy of avalanche models on arbitrary topography. *Acta Mech.* **205**, 121–149 (2009).
- [2] Hutter, K., Svendsen, B., Rickenmann, D.: Debris flow modeling: A review. *Continuum Mechanics and Thermodynamics* **8**, 1–35 (1994).
- [3] Greve, R., Blatter, H.: *Dynamics of Ice Sheets and Glaciers.* (Springer, Berlin, 2009).
- [4] Kumar, A., Karig, D., Acharya, R., Neethirajan, S., Mukherjee, P. P., Retterer, S., Doktycz, M. J.: Microscale confinement features can affect biofilm formation. *Microfluid. Nanofluid.* **14**, 895–902 (2013).
- [5] de Gennes, P.-G., Brochard-Wyart, F., Quere, D.: *Capillarity and Wetting Phenomena* (Springer, Berlin, 2004).
- [6] Braun, R. J.: Dynamics of the tear film. *Annu. Rev. Fluid Mech.* **44**, 267–297 (2011).
- [7] Webb, R. L.: *Principles of Enhanced Heat Transfer* (Wiley, New York, 1994).
- [8] Vlasogiannis P., Karagiannis G., Argyropoulos P., Bontozoglou V.: Air-water two-phase flow and heat transfer in a plate heat exchanger. *International Journal of Multiphase Flow* **28**, 757 – 772 (2002).
- [9] Valluri, P., Matar, O. K., Hewitt, G. F., Mendes, M. A.: Thin film flow over structured packings at moderate Reynolds numbers. *Chem. Eng. Sci.* **60**, 1965 – 1975 (2005).
- [10] J. M. de Santos, T. R. Melli, and L. E. Scriven: Mechanics of Gas-Liquid Flow in Packed-Bed Contactors. *Annual Review of Fluid Mechanics* **23**, 233 – 260 (1991).
- [11] Kistler, S. F., Schweizer, P. M.: *Liquid Film Coating* (Springer, Netherlands, 1997).
- [12] Weinstein, S. J., Ruschak, K. J.: Coating flows. *Annu. Rev. Fluid Mech.* **36**, 29–53 (2004).
- [13] Gugler, G., Beer, R., Mauron, M.: Operative limits of curtain coating due to edges. *Chem. Eng. Process. Process. Intensif.* **50**, 462 – 465 (2011).
- [14] Nusselt, W.: Die Oberflächenkondensation des Wasserdampfes. *VDI Z. (1857-1968)* **60**, 541–546 (1916).
- [15] Scholle, M., Aksel, N.: An exact solution of visco-capillary flow in an inclined channel. *Zeitschrift für Angewandte Mathematik und Physik ZAMP* **52**, 749–769 (2001).
- [16] Haas, A., Pollak, T., Aksel, N.: Side wall effects in thin gravity-driven film flow: steady and draining flow. *Phys. Fluids* **23**, 062107 (2011).

- [17] Scholle, M. Aksel, N.: Thin film limit and film rupture of the visco-capillary gravity-driven channel flow. *Zeitschrift für Angewandte Mathematik und Physik ZAMP* **54**, 517–531 (2003).
- [18] Pozrikidis, C., Thoroddsen, S. T.: The deformation of a liquid film flowing down an inclined plane wall over a small particle arrested on the wall. *Phys. Fluids A* **3**, 2546–2558 (1991).
- [19] Decré, M. M. J., Baret, J.-C.: Gravity-driven flows of viscous liquids over two-dimensional topographies. *J. Fluid Mech.* **487**, 147–166 (2003).
- [20] Mazouchi, A., Homsy, G. M.: Free surface Stokes flow over topography. *Phys. Fluids* **13**, 2751–2761 (2001).
- [21] Hayes, M., O'Brien, S. B. G., Lammers, J. H.: Green's function for steady flow over a small two-dimensional topography. *Phys. Fluids* **12**, 2845–2858 (2000).
- [22] Kalliadasis, S., C. Bielarz, Homsy, G. M.: Steady free-surface thin film flows over topography. *Phys. Fluids* **12**, 1889 – 1898 (2000).
- [23] Kalliadasis, S., C. Bielarz, Homsy, G. M.: Erratum: "Steady free-surface thin film flows over topography" [*Phys. Fluids* 12, 1889 (2000)]. *Phys. Fluids* **12**, 3305 (2000).
- [24] Aksel, N.: Influence of the capillarity on a creeping film flow down an inclined plane with an edge. *Arch. Appl. Mech.* **70**, 81–90 (2000).
- [25] Scholle, M. Aksel, N.: A general free surface rule for Stokes flow of fluid films over obstacles. *Acta Mech.* **191**, 155–159 (2007).
- [26] Negny S., Meyer M., Prevost M.: Study of a laminar falling film flowing over a wavy wall column: Part I. Numerical investigation of the flow pattern and the coupled heat and mass transfer. *International Journal of Heat and Mass Transfer* **44**, 2137–2146 (2001).
- [27] Pozrikidis, C.: The flow of a liquid film along a periodic wall. *J. Fluid Mech.* **188**, 275–300 (1988).
- [28] Bontozoglou, V., Papapolymerou, G.: Laminar film flow down a wavy incline. *Int. J. Multiph. Flow* **23**, 69 – 79 (1997).
- [29] Trifonov, Y. Y.: Viscous liquid film flows over a periodic surface. *Int. J. Multiph. Flow* **24**, 1139–1161 (1999).
- [30] Wierschem, A., Bontozoglou, V., Heining, C., Uecker, H., Aksel, N.: Linear resonance in viscous films on inclined wavy planes. *Int. J. Multiph. Flow* **34**, 580–589 (2008).
- [31] Pak, M. I., Hu, G. H.: Numerical investigations on vortical structures of viscous film flows along periodic rectangular corrugations. *Int. J. Multiph. Flow* **37**, 369 – 379 (2011).
- [32] Vlachogiannis, M., Bontozoglou, V.: Experiments on laminar film flow along a periodic wall. *J. Fluid Mech.* **457**, 133–156 (2002).
- [33] Argyriadi, K., Vlachogiannis, M., Bontozoglou, V.: Experimental study of inclined film flow along periodic corrugations: the effect of wall steepness. *Phys. Fluids* **18**, 012102 (2006).

-
- [34] Wierschem, A., Scholle, M., Aksel, N.: Comparison of different theoretical approaches to experiments on film flow down an inclined wavy channel. *Exp. Fluids* **33**, 429 – 442 (2002).
- [35] Wierschem, A., Lepski, C., Aksel, N.: Effect of long undulated bottoms on thin gravity-driven films. *Acta Mech.* **179**, 41–66 (2005).
- [36] Wierschem, A., Aksel, N.: Hydraulic jumps and standing waves in gravity-driven flows of viscous liquids in wavy open channels. *Phys. Fluids* **16**, 3868–3877 (2004).
- [37] Luo, H., Pozrikidis, C.: Gravity-driven film flow down an inclined wall with three-dimensional corrugations. *Acta Mech.* **188**, 209–225 (2007).
- [38] Trifonov, Y. Y.: Viscous film flows down corrugated surfaces. *Journal of Applied Mechanics and Technical Physics* **45**, 389–400 (2004).
- [39] Sadiq, I. M. R., Gambaryan-Roisman, T., Stephan, P.: Falling liquid films on longitudinal grooved geometries: Integral boundary layer approach. *Phys. Fluids* **24**, 014104 (2012).
- [40] Heining, C., Pollak, T., Aksel, N.: Pattern formation and mixing in three-dimensional film flow. *Phys. Fluids* **24**, 042102 (2012).
- [41] Heining, C., Bontozoglou, V., Aksel, N., Wierschem, A.: Nonlinear resonance in viscous films on inclined wavy planes. *Int. J. Multiph. Flow* **35**, 78 – 90 (2009).
- [42] Gaskell, P. H., Jimack, P. K., Sellier, M., Thompson, H. M., Wilson, M. C. T.: Gravity-driven flow of continuous thin liquid films on non-porous substrates with topography. *J. Fluid Mech.* **509**, 253 – 280 (2004).
- [43] Wang, C. Y.: Liquid film flowing slowly down a wavy incline. *AIChE J.* **27**, 207 – 212 (1981).
- [44] Blyth, M. G., Pozrikidis, C.: Film flow down an inclined plane over a three-dimensional obstacle. *Phys. Fluids* **18**, 052104 (2006).
- [45] Baxter, S. J., Power, H., Cliffe, K. A., Hibberd, S.: Three-dimensional thin film flow over and around an obstacle on an inclined plane. *Phys. Fluids* **21**, 032102 (2009).
- [46] Lee, Y. C., Thompson, H. M., Gaskell, P. H.: An efficient adaptive multigrid algorithm for predicting thin film flow on surfaces containing localised topographic features. *Comput. Fluids* **36**, 838 – 855 (2007).
- [47] Lee, Y. C., Thompson, H. M., Gaskell, P. H.: Three-dimensional thin film and droplet flows over and past surface features with complex physics. *Comput. Fluids* **46**, 306 – 311 (2011).
- [48] Lee, Y. C., Thompson, H. M., Gaskell, P. H.: Dynamics of thin film flow on flexible substrate. *Chem. Eng. Process. Process. Intensif.* **50**, 525 – 530 (2011).
- [49] Bontozoglou, V., Serifi, K.: Falling film flow along steep two-dimensional topography: The effect of inertia. *Int. J. Multiph. Flow* **34**, 734–747 (2008).
- [50] Malamataris, N. A., Bontozoglou, V.: Computer aided analysis of viscous film flow along an inclined wavy wall. *J. Comput. Phys.* **154**, 372 – 392 (1999).

- [51] Luo, H., Pozrikidis, C.: Effect of inertia on film flow over oblique and three-dimensional corrugations. *Phys. Fluids* **18**, 078107 (2006).
- [52] Luo, H., Pozrikidis, C.: Publisher’s note: Effect of inertia on film flow over oblique and three-dimensional corrugations [Phys. Fluids 18, 078107 (2006)]. *Phys. Fluids* **18**, 129901 (2006).
- [53] Bontozoglou, V., Kalliadasis, S., Karabelas, A. J.: Inviscid free-surface flow over a periodic wall. *J. Fluid Mech.* **226**, 189 – 203 (1991).
- [54] Bontozoglou, V.: Laminar film flow along a periodic wall. *CMES-Comp. Model Eng.* **1**, 133 – 142 (2000).
- [55] Sellier, M.: Inverse problems in free surface flows: a review. *Acta Mech.* **227**, 913–935 (2016).
- [56] Heining, C.: Velocity field reconstruction in gravity-driven flow over unknown topography. *Phys. Fluids* **23**, 032101 (2011).
- [57] Heining, C., Pollak, T., Sellier, M.: Flow domain identification from free surface velocity in thin inertial films. *J. Fluid Mech.* **720**, 338–356 (2013).
- [58] Anjalaiah, Y., Chakraborty, S., Usha, R.: Steady solution of an inverse problem in gravity-driven shear-thinning film flow: reconstruction of an uneven bottom substrate. *J. Non-Newton Fluid Mech.* **219**, 65–77 (2015).
- [59] Usha, R., Anjalaiah: Steady solution and spatial stability of gravity-driven thin-film flow: reconstruction of an uneven slippery bottom substrate. *Acta Mech.* **227**, 1685–1709 (2016).
- [60] Heining, C., Sellier, M.: Flow domain identification in three-dimensional creeping flows. *Phys. Fluids.* **29**, 012107 (2017).
- [61] Heining, C., Sellier, M., Aksel, N.: The inverse problem in creeping film flows. *Acta Mech.* **223**, 841–847 (2012).
- [62] Sellier, M.: Substrate design or reconstruction from free surface data for thin film flows. *Phys. Fluids* **20**, 062106 (2008).
- [63] Schörner, M., Reck, D., Aksel, N.: Does the topography’s specific shape matter in general for the stability of film flows? *Phys. Fluids* **27**, 042103 (2015).
- [64] Scholle, M., Rund, A., Aksel, N.: Drag reduction and improvement of material transport in creeping films. *Acta Mech.* **75**, 93–112 (2006).
- [65] Scholle, M., Wierschem, A., Aksel, N.: Creeping films with vortices over strongly undulated bottoms. *Acta Mech.* **168**, 167–193 (2004).
- [66] Wierschem, A., Scholle, M., Aksel, N.: Vortices in film flow over strongly undulated bottom profiles at low Reynolds numbers. *Phys. Fluids* **15**, 426–435 (2003).
- [67] Wierschem, A., Aksel, N.: Influence of inertia on eddies created in films creeping over strongly undulated substrates. *Phys. Fluids* **16**, 4566–4574 (2004).

-
- [68] Scholle, M., Haas, A., Aksel, N., Wilson, M. C. T., Thompson, H. M., Gaskell, P. H.: Eddy genesis and manipulation in plane laminar shear flow. *Phys. Fluids* **21**, 073602 (2009).
- [69] Scholle, M., Haas, A., Aksel, N., Wilson, M. C. T., Thompson, H. M., Gaskell, P. H.: Competing geometric and inertial effects on local flow structure in thick gravity-driven fluid films. *Phys. Fluids* **20**, 123101 (2008).
- [70] Wierschem, A., Pollak, T., Heining, C., Aksel, N.: Suppression of eddies in films over topography. *Phys. Fluids* **22**, 113603 (2010).
- [71] Nguyen, P. K., Bontozoglou, V.: Steady solutions of inertial film flow along strongly undulated substrates. *Phys. Fluids* **23**, 052103 (2011).
- [72] Scholle, M., Haas, A., Aksel, N., Thompson, H. M., Hewson, R. W., Gaskell, P. H.: The effect of locally induced flow structure on global heat transfer for plane laminar shear flow. *Int. J. Heat Fluid Flow* **30**, 175 – 185 (2009).
- [73] Kapitza, P. L.: Wavy flow of thin layers of a viscous fluid. *Zh. Eksp. Teor. Fiz.* **18**, 3–28 (1948).
- [74] Kapitza, P. L., Kapitza, S. P.: Wavy flow of thin layers of a viscous fluid. *Zh. Eksp. Teor. Fiz.* **19**, 105–120 (1948).
- [75] Benjamin, T. B.: Wave formation in laminar flow down an inclined plane. *J. Fluid Mech.* **2**, 554–574 (1957).
- [76] Yih, C. S.: Stability of liquid flow down an inclined plane. *Phys. Fluids* **6**, 321–334 (1963).
- [77] Orr, W. M’F.: The stability or instability of the steady motions of a perfect liquid and of a viscous liquid. Part I: A perfect liquid. *Proc. R. Ir. Acad. A Math. Phys. Sci.* **27**, 9–68 (1907).
- [78] Orr, W. M’F.: The stability or instability of the steady motions of a perfect liquid and of a viscous liquid. Part II: A viscous liquid. *Proc. R. Ir. Acad. A Math. Phys. Sci.* **27**, 69–138 (1907).
- [79] Sommerfeld, A.: Ein Beitrag zur hydrodynamischen Erklärung der turbulenten Flüssigkeitsbewegungen. In: *Proceedings of the 4th International Congress of Mathematicians* **3**, 116–124 (1908).
- [80] Liu, J., Paul, J. D., Gollub, J. P.: Measurements of the primary instabilities of film flows. *J. Fluid Mech.* **250**, 69 – 101 (1993).
- [81] Liu, J., Gollub, J. P.: Solitary wave dynamics of film flows. *Phys. Fluids* **6**, 1702–1712 (1994).
- [82] Vlachogiannis, M., Samandas, A., Leontidis, V., Bontozoglou, V.: Effect of channel width on the primary instability of inclined film flow. *Phys. Fluids* **22**, 012106 (2010).
- [83] Georgantaki, A., Vatteville, J., Vlachogiannis, M., Bontozoglou, V.: Measurements of liquid film flow as a function of fluid properties and channel width: evidence for surface-tension-induced long-range transverse coherence. *Phys. Rev. E* **84**, 026325 (2011).

- [84] Pollak, T., Haas, A., Aksel, N.: Sidewall effects on the instability of thin gravity-driven films: from long-wave to short-wave instability. *Phys. Fluids* **23**, 094110 (2011).
- [85] Wierschem, A., Aksel, N.: Instability of a liquid film flowing down an inclined wavy plane. *Physica D* **186**, 221–237 (2003).
- [86] Trifonov, Y. Y.: Stability and nonlinear wavy regimes in downward film flows on a corrugated surface. *J. App. Mech. Tech. Phys.* **48**, 91–100 (2007).
- [87] Trifonov, Y. Y.: Stability of a viscous liquid film flowing down a periodic surface. *Int. J. Multiph. Flow* **33**, 1186–1204 (2007).
- [88] Trifonov, Y. Y.: Stability and bifurcations of the wavy film flow down a vertical plate: the results of integral approaches and full-scale computations. *Fluid Dynamics Research* **44**, 031418 (2012).
- [89] Heining, C., Aksel, N.: Effects of inertia and surface tension on a power-law fluid flowing down a wavy incline. *Int. J. Multiphase Flow* **36**, 847–857 (2010).
- [90] D’Alessio, S. J. D., Pascal, J. P., Jasmine, H. A.: Instability in gravity-driven flow over uneven surfaces. *Phys. Fluids* **21**, 062105 (2009).
- [91] Tseluiko, D., Blyth, M. G., Papageorgiou, D. T.: Stability of film flow over inclined topography based on a long-wave nonlinear model. *Journal of Fluid Mechanics* **729**, 638–671 (2013).
- [92] Pollak, T., Aksel, N.: Crucial flow stabilization and multiple instability branches of gravity-driven films over topography. *Phys. Fluids* **25**, 024103 (2013).
- [93] Trifonov, Y. Y.: Stability of a film flowing down an inclined corrugated plate: the direct Navier-Stokes computations and Floquet theory. *Phys. Fluids* **26**, 114101 (2014).
- [94] Cao, Z., Vlachogiannis, M., Bontozoglou, V.: Experimental evidence for a short-wave global mode in film flow along periodic corrugations. *J. Fluid Mech.* **718**, 304–320 (2013).
- [95] Schörner, M., Reck, D., Aksel, N.: Stability phenomena far beyond the Nusselt flow – Revealed by experimental asymptotics. *Phys. Fluids* **28**, 022102 (2016).
- [96] Trifonov, Y. Y.: Viscous liquid film flow down an inclined corrugated surface. Calculation of the flow stability to arbitrary perturbations using an integral method. *J. Appl. Mech. Tech. Phys.* **57**, 195 – 201 (2016).
- [97] Trifonov, Y. Y.: Nonlinear waves on a liquid film falling down an inclined corrugated surface. *Phys. Fluids* **29**, 054104 (2017).
- [98] Schörner, M., Aksel, N.: The stability cycle: a universal pathway for the stability of films over topography. *Phys. Fluids* **30**, 012105 (2018).
- [99] M. Schörner, D. Reck, N. Aksel and Y. Y. Trifonov: Switching between different types of stability isles in films over topographies. *Acta. Mech.* **229**, 423-436 (2018).
- [100] Aksel, N., Schörner, M.: Films over topography: from creeping flow to linear stability, theory, and experiments, a review. *Acta Mech.* **229**, 1453–1482 (2018).

-
- [101] Lin, S. P.: Finite-amplitude stability of a parallel flow with a free surface. *J. Fluid Mech.* **36**, 113–126 (1969).
- [102] Chang, H.-C., Demekhin, E. A., Kopelevich, D. I.: Nonlinear evolution of waves on a vertically falling film. *Journal of Fluid Mechanics* **250**, 433–480 (1993).
- [103] Krantz, W. B., Goren, S. L.: Finite-amplitude, long waves on liquid films flowing down a plane. *Industrial & Engineering Chemistry Fundamentals* **9**, 107–113 (1970).
- [104] Trifonov, Y. Y., Tselodub, O. Y.: Nonlinear waves on the surface of a falling liquid film. Part 1. Waves of the first family and their stability. *Journal of Fluid Mechanics* **229**, 531–554 (1990).
- [105] Yu, L. Q., Wasden, F. K., Dukler, A. E., Balakotaiah, V.: Nonlinear evolution of waves on falling films at high Reynolds numbers. *Physics of Fluids* **7**, 1886–1902 (1995).
- [106] Rosenau, P., Oron, A.: Evolution and breaking of liquid film flowing on a vertical cylinder. *Physics of Fluids A* **1**, 1763–1766 (1989).
- [107] Oron, A., Gottlieb, O.: Nonlinear dynamics of temporally excited falling liquid films. *Physics of Fluids* **14**, 2622–2636 (2002).
- [108] Gjevik, B.: Occurrence of finite-amplitude surface waves on falling liquid films. *Phys. Fluids* **13**, 1918–1925 (1970).
- [109] Benney, D. J.: Long waves on liquid films. *J. Math. Phys. (Cambridge, Mass.)* **45**, 150 (1966).
- [110] Ruyer-Quil, C., Manneville, P.: Improved modeling of flows down inclined planes. *Eur. Phys. J. B* **15**, 357 (2000).
- [111] Chang, H. C., Demekhin, E. A.: *Complex Wave Dynamics on Thin Films* (Elsevier, Amsterdam, 2002).
- [112] Malamataris, N. A., Vlachogiannis, M., Bontozoglou, V.: Solitary waves on inclined films: Flow structure and binary interactions. *Physics of Fluids* **14**, 1082–1094 (2002).
- [113] Argyriadi, K., Serifi, K., Bontozoglou, V.: Nonlinear dynamics of inclined films under low-frequency forcing. *Physics of Fluids* **16**, 2457–2468 (2004).
- [114] Nosoko, T., Miyara, A.: The evolution and subsequent dynamics of waves on a vertically falling liquid film. *Physics of Fluids* **16**, 1118–1126 (2004).
- [115] Vlachogiannis, M., Bontozoglou, V.: Observations of solitary wave dynamics of film flows. *J. Fluid Mech.* **435**, 191–215 (2001).
- [116] Alekseenko, S. V., Nakoryakov, V. Y., Pokusaev, B. G.: Wave formation on a vertical falling liquid film. *AIChE* **31**, 1446–1460 (1985).
- [117] Chang, H.-C., Demekhin, E., Kalaidin, E.: Interaction dynamics of solitary waves on a falling film. *Journal of Fluid Mechanics* **294**, 123–154 (1995).
- [118] Malamataris, N. A., Balakotaiah, V.: Flow structure underneath the large amplitude waves of a vertically falling film. *AIChE Journal* **54**, 1725–1740 (2008).

- [119] Chakraborty, S., Nguyen, P.-K., Ruyer-Quil, C., Bontozoglou, V.: Extreme solitary waves on falling liquid films. *Journal of Fluid Mechanics* **745**, 564-591 (2014).
- [120] Meza, C. E., Balakotaiah, V.: Modeling and experimental studies of large amplitude waves on vertically falling films. *Chemical Engineering Science* **63**, 4704 – 4734 (2008).
- [121] Miyara, A.: Numerical simulation of wavy liquid film flowing down on a vertical wall and an inclined wall. *International Journal of Thermal Sciences* **39**, 1015-1027 (2000).
- [122] Brown, H. S., Kevrekidis, I. G., Oron, A., Rosenau, P.: Bifurcations and pattern formation in the regularized Kuramoto-Sivashinsky equation. *Physics Letters A* **163**, 299-308 (1992).
- [123] Craster, R. V., Matar, O. K.: Dynamics and stability of thin liquid films. *Rev. Mod. Phys.* **81**, 1131–1198 (2009).
- [124] Chang, H. C.: Wave evolution on a falling film. *Annu. Rev. Fluid Mech.* **26**, 103–136 (1994).
- [125] Reck, D., Aksel, N.: Recirculation areas underneath solitary waves on gravity-driven film flows. *Phys. Fluids* **27**, 112107 (2015).
- [126] Reck, D., Aksel, N.: Experimental study on the evolution of traveling waves over an undulated incline. *Phys. Fluids* **25**, 102101 (2013).
- [127] Dávalos-Orozco, L. A.: Nonlinear instability of a thin film flowing down a smoothly deformed surface. *Phys. Fluids* **19**, 074103 (2007).
- [128] Drazin P. G. and Reid W. H.: *Hydrodynamic Stability* (Cambridge University Press, 1981).
- [129] Faisst, H., Eckhardt, B.: Traveling Waves in Pipe Flow. *Phys. Rev. Lett.* **91**, 224502 (2003).
- [130] Liu, J., Schneider, J. B., Gollub, J. P.: Three-dimensional instabilities of film flows. *Phys. Fluids* **7**, 55 – 67 (1995).
- [131] Park, C. D., Nosoko, T.: Three-dimensional wave dynamics on a falling film and associated mass transfer. *AIChE Journal* **49**, 2715 – 2727 (2003).
- [132] Adomeit, P., Renz, U.: Hydrodynamics of three-dimensional waves in laminar falling films. *International Journal of Multiphase Flow* **26**, 1183 – 1208 (2000).
- [133] Scheid, B., Ruyer-Quil, C., Manneville, P.: Wave patterns in film flows: modelling and three-dimensional waves. *Journal of Fluid Mechanics* **562**, 183 – 222 (2006).
- [134] Demekhin, E. A., Kalaidin, E. N., Kalliadasis, S., Vlaskin, S. Yu.: Three-dimensional localized coherent structures of surface turbulence. I. Scenarios of two-dimensional–three-dimensional transition. *Physics of Fluids* **19**, 114103 (2007).
- [135] Demekhin, E. A., Kalaidin, E. N., Selin, A. S.: Three-dimensional localized coherent structures of surface turbulence. III. Experiment and model validation. *Physics of Fluids* **22**, 092103 (2010).

-
- [136] Kharlamov, S. M., Guzanov, V. V., Bobylev, A. V., Alekseenko, S. V., Markovich, D. M.: The transition from two-dimensional to three-dimensional waves in falling liquid films: Wave patterns and transverse redistribution of local flow rates. *Physics of Fluids* **27**, 114106 (2015).
- [137] Chandrasekhar S.: *Hydrodynamic and Hydromagnetic Stability* (Dover, 1981).
- [138] Ockendon H. and Ockendon J. R.: *Viscous Flow* (Cambridge Texts in Applied Mathematics, 1995).
- [139] Dauth, M., Schörner, M., Aksel, N.: What makes the free surface waves over topographies convex or concave? A study with Fourier analysis and particle tracking. *Phys. Fluids* **29**, 092108 (2017).
- [140] Reck, D.: *Experiments on the dynamics of waves on gravity-driven viscous film flows* [Doctoral dissertation] (University of Bayreuth, Bayreuth, 2016).
- [141] Schoerner, M.: *The stability of gravity-driven viscous films over topography* [Doctoral dissertation] (University of Bayreuth, Bayreuth, 2018).
- [142] Pollak, T.: *Influence of side walls and undulated topography on viscous gravity-driven film flow* [Doctoral dissertation] (University of Bayreuth, Bayreuth, 2012).
- [143] Dauth, M., Aksel, N.: Breaking of waves on thin films over topographies. *Phys. Fluids* **30**, 082113 (2018).
- [144] Dauth, M., Aksel, N.: Transition of regular wave fronts to irregular wave fronts in gravity-driven thin films over topography. *Acta Mech.* **230** (7), 2475–2490 (2019).
- [145] Tropea, C., Yarin, A., Foss, J. F. (Eds.): *Springer Handbook of Experimental Fluid Mechanics*, p. 681 (Springer, Berlin, 2007).
- [146] Happel, J., Brenner, H.: *Low Reynolds number hydrodynamics* (Springer, Netherlands, 1983).
- [147] Spurk, J.-H., Aksel, N.: *Fluid Mechanics*, 2.ed. (Springer, Berlin, 2008).
- [148] Crocker, J. C., Grier, D. G.: Methods of digital video microscopy for colloidal studies. *J. Colloid Interface Sci.* **179**, 298 – 310 (1996).
- [149] Allan, D., Caswell, T., Keim, N., van der Wel, C.: "Trackpy version 0.3.2." Zendo, 2016.
- [150] Le Méhauté, B.: *An Introduction to Hydrodynamics & Water Waves* (Springer Verlag, New York, 1976).
- [151] Stoker, J. J.: *Water Waves: The Mathematical Theory with Applications* (John Wiley & Sons, Inc., New York, 1992).
- [152] Varchanis, S., Dimakopoulos, Y., Tsamopoulos, J.: Steady film flow over a substrate with rectangular trenches forming air inclusions. *Phys. Rev. Fluids* **2**, 124001 (2017).
- [153] Eggers J., Drop formation - an overview. *ZAMM-Zeitschrift für angewandte Mathematik und Mechanik* **179**, 400-410 (2005).

Danksagungen

Im Zuge meiner Arbeit als wissenschaftlicher Mitarbeiter am Lehrstuhl für Technische Mechanik und Strömungsmechanik der Universität Bayreuth unter Leitung von Professor Dr. Nuri Aksel entstand diese Dissertation. Professor Aksel gebührt mein ausdrücklicher Dank für die herausragende Betreuung. Die vielen Diskussionen, für die er sich stets Zeit nahm, setzten den Grundstein für die zahlreichen Erkenntnisse der Arbeit. Für das mir entgegengebrachte Vertrauen und die Freiheit in der Forschung möchte ich mich besonders bedanken.

Bei allen Mitarbeitern des Lehrstuhls für Technische Mechanik und Strömungsmechanik möchte ich mich ganz herzlich bedanken. Sie haben mich während meiner Zeit hier am Lehrstuhl begleitet und tatkräftig unterstützt. Insbesondere möchte ich mich bei meinen wissenschaftlichen Kollegen Dr. Daniel Reck, Dr. Mario Schörner und Armin Kögel für die zahlreichen Fachdiskussionen bedanken. Die Diskussionen haben einen tiefergehenden Einblick in die Thematik, Problemlösungen und neue Ideen hervorgebracht. Außerdem möchte ich Marion Märkl, Gabriele Jena, Markus Horn und insbesondere Stephan Eißner hervorheben für die tatkräftige Unterstützung bei den Laborarbeiten und Experimenten. Weiterhin gilt mein Dank Dr. Lutz Heymann für dauerhafte Hilfsbereitschaft bei thematischen und organisatorischen Angelegenheiten.

Besonderer Dank gilt meiner Familie. Insbesondere möchte ich mich bei meinen Eltern für ihre liebevolle und uneingeschränkte Unterstützung auf meinem gesamten Lebensweg bedanken.

Selbstständigkeitserklärung

Hiermit versichere ich, dass ich die vorliegende Dissertation selbstständig verfasst und keine anderen als die von mir angegebenen Quellen und Hilfsmittel verwendet habe.

Ich erkläre, dass ich diese Dissertation nicht bereits zur Erlangung eines akademischen Grades eingereicht habe und dass ich nicht bereits diese oder eine gleichartige Doktorprüfung endgültig nicht bestanden habe.

Des Weiteren erkläre ich, dass ein gewerblicher Promotionsberater bzw. Promotionsvermittler weder bisher in Anspruch genommen wurde noch künftig in Anspruch genommen wird.

(Ort, Datum)

(Dipl.-Phys. Markus Dauth)